KEK Proceedings 98 -7
November 1998
A/R/D

Proceedings of the Seventh EGS4 Users' Meeting in Japan

July 30 - August 1, 1998.

KEK, Tsukuba, Japan

Edited by

H. Hirayama, Y.Namito and S.Ban

High Energy Accelerator Research Organization

High Energy Accelerator Research Organization (KEK), 1998

KEK Reports are available from:

Information Resources Division
High Energy Accelerator Research Organization (KEK)
1-1 Oho, Tsukuba-shi
Ibaraki-ken, 305-0801
JAPAN

Phone: 0298-64-5137
Fax: 0298-64-4604
Cable: KEK OHO
E-mail: Library@kekvax.kek.jp
Internet: http://www.kek.jp

FOREWARD

The Seventh EGS4 Users' Meeting in Japan was held at High Energy Accelerator Research Organization (KEK) from July 30 to August 1. The meeting has been hosted by the Radiation Science Center. Nearly 90 participants attended the meeting.

The meeting was divided into two parts. Lectures concerning the EGS4 System, Mortran, User code, HOWFAR, how to use PEGS4, how to write source routine and the EGS4 shower display system on PC were given at the first half. Practices to install the EGS4 system on the UNIX workstation or PC and to run PEGS4 or user code were also performed. In the later half, 15 talks related EGS4 were presented. The talks covered the wide fields, like the medical application and the calculation of various detector response *etc.* These talks were very useful to exchange the information between the researchers in the different fields.

Finally, we would like to express our great appreciation to all authors who have prepared manuscript quickly for the publication of this proceedings.

Hideo Hirayama
Yoshihito Namito
Syuichi Ban
Radiation Science Center
KEK, High Energy Accelerator Research Organization

CONTENTS

IMPLEMENTATION OF ELECTRON-IMPACT IONIZATION INTO THE EGS4 CODE

Y. NAMITO and H. HIRAYAMA

High Energy Accelerator Research Organization (KEK)
Oho, Tsukuba-shi, Ibaraki-ken, 305-0801, Japan

Abstract

A modification to the general-purpose Monte-Carlo electron-photon transport code EGS4 [1] was made in order to include K-shell electron-impact ionization (EII). Five cross sections of K-shell EII have been implemented. The ratio of the K-shell EII cross section to the Møller scattering cross section is prepared by the PEGS4 program, and is then used in the EGS4 code. Simulations of the K-X ray emissions from Al, Ti, Cu, Sn, Ag and Au targets for an electron beam with an incident energy of 0.01 to 3 MeV were performed by using the improved EGS4 code; the calculated K-X ray yields agreed well with the measurements.

1 Introduction

When an electron beam having keV-MeV energy hits a target, the major photon production channels are:

1. bremsstrahlung,
2. fluorescent photon emitted after a photoelectric effect due to bremsstrahlung photons,
3. fluorescent photon emitted after the scattering of an incident electron with an inner-shell electron (electron impact ionization:EII).

It is necessary to treat all of these three channels in order to precisely simulate photon emission from a target. In the original EGS4 code, photon production channels (1) and (2) are already treated, but EII has not been treated so far. We reported the implementation of EII into the EGS4 code in this series of workshop in 1996 [2] and in 1997 [3]. Gryziński's K-shell EII cross section and Kolbenstvedt-revised one were used in 1996 and in 1997 respectively. And a simulation of photon emission from Sn target for an incident 0.1 MeV electron beam was performed using the improved EGS4 code in both the time.

In this study, following five different cross sections of EII is compared with measured cross sections: (1) Gryziński's (2) Kolbenstvedt-original (3) Kolbenstvedt-revised (4) Casnati's (5) Jakoby's. All of these five cross sections are included into EGS4 code. These EII cross sections are described in section 2. To verify the validity of the improved EGS4 code, a simulation of the K-X ray emission from Al, Ti, Cu, Sn, Ag, and Au targets for an incident 0.01-to-3 MeV electron beam was performed using the improved EGS4 code; the calculated K-X ray yield was compared with the measurements. The way of implementation of EII is basically the same as the one reported in 1996 [2].

2 Electron-Impact Ionization Cross Section

In an implementation of EII to a general-purpose electromagnetic shower code, it is important to choose an EII cross section which agrees with measurements over wide energy and atomic-number regions. In this section, the following five formulas for the EII cross section are compared with the measurements.

The K-shell EII cross sections for Al, Ar, Cu, Ag and Au are shown in Fig. 1, and the measured values are taken from Refs. [6, 7, 8, 9, 10, 11, 12, 13] [14, 15, 16, 17, 18, 19, 20] [21, 22, 23, 24, 25, 26, 27, 28, 29] [30, 31, 32]. In the case that the K-shell fluorescent yield (ω_K) used is mentioned, and that the fluorescent yield is different from those given by Bambynek et al. [33], the measured value [6, 7, 11, 14, 24] is modified so as to be consistent with Bambynek et al.

The K-shell EII cross section calculated by the following formulas are shown in Fig. 1:

- Gryziński developed the relativistic EII cross section based on semi-classical theory [4] (Hereafter, referred to as Gryziński's cross section). Gryziński's cross section agrees reasonably well with measurements in the case that $E_K \leq$ a few tens of MeV, as shown by the dashed lines in Fig. 1. Here, E_K represents the incident electron kinetic energy. Gryziński also developed a nonrelativistic EII cross section. The nonrelativistic EII cross section, however, differs from the relativistic cross section in only one correction factor for relativity. Gryziński's nonrelativistic cross section agrees well with measurements in the case that $E_K \leq$ a few hundreds of keV. Gryziński's cross section can be applied for any shell.

- Kolbenstvedt developed an EII cross-section formula for a K-shell electron based on a simple theory (Hereafter, referred to as Kolbenstvedt-original cross section) [5]. The Kolbenstvedt original cross section is calculated as the sum of the contribution due to ionization by a virtual photoelectric effect and that due to close collisions. The Kolbenstvedt original cross sections, which are shown as chain lines in Fig. 1, are bigger than measurements in the case that $E_K \leq 4 \times E_B$. Here, E_B represents the binding energy of the orbit electron.

- Kolbenstvedt revised the cross section in 1970 [13]. This revised cross section agreed with measurements better than did the Kolbenstvedt original cross section, but is bigger than the measured values [24, 31] in the vicinity of the K-shell binding energy. The Kolbenstvedt revised cross sections are shown as double-dot-chain lines in Fig. 1. This cross section shows the best agreement with measurements in the case that $E_K \geq 20$ MeV and Z=79.

- Casnati et al. developed an empirical formula to describe the K-shell EII cross section [34], which are shown as the solid lines in Fig. 1. The Casnati's cross section reproduces the measurement best among five cross-section formulas discussed in this section.

- Jakoby made an empirical formula of the K-shell EII cross section by a fitting using 600 measurements [35]. The Jakoby's cross section is shown as the dotted line in Fig. 1.

Since all of these cross sections are expressed in relatively simple formulas, they do not need any numerical tabulation, and agreed reasonably well with measurements over the wide energy and atomic-number ranges. Since the empirical formula depends on the measurement, it is limited to only the K-shell. In Figs. 1 (b), (d), (e); Scofield's Born-approximation calculation is also shown as a long chain line [36, 37].

All five cross sections are employed for the implementation of EII into the EGS4 code. Casnati's cross section is used as a default because it reproduces the measurements best among the five cross sections shown here. Gryziński's cross section is used as the second choice because this cross section is based on a theory, and is therefore most reliable for an area of incident energy and atomic number where there is no reliable measured cross section. The Kolbenstvedt-revised cross section is used as

the third choice, since this cross section agrees with the measurement best in the case that $E_K >$ 100 MeV. However, only Casnati's and Gryziński's cross sections were used in the comparison with measurement in section 4, since there are no comparisons in the energy range above 100 MeV. The choice of the cross section is described in Discussion. Two other cross sections also remained in the program to meet the possible necessity of users.

3 Method of Calculation

EII is treated as being a part of Møller scattering in the EGS4 code. The ratio of EII to the Møller scattering cross section is calculated by the PEGS4 program (a pre-processor program for EGS4). Electron transport other than Møller scattering is not affected by the implementation of EII.

When EII is sampled in a Monte-Carlo calculation, the emission of a K-X ray or an Auger electron is sampled using the K-shell fluorescence yield [38]. In the case of K-X-ray emission, one of the K_{α_1}, K_{α_2}, K_{β_1} and K_{β_2} emissions is sampled according to the intensity ratio. The calculation method used to treat 4 kinds of K-X rays was taken from Hirayama's improvement of EGS4 [39]. The Auger electron is not followed. In the case that a K-X ray is emitted, the difference in the E_B and K-X ray energy is deposited locally. In the case that no K-X ray is generated (i.e. Auger electron emission), E_B is deposited locally.

The energy and direction of electrons after EII are treated in an approximate way. E_B is subtracted from the energy of either one of the two electrons related to the Møller scattering. In the case that neither of the two electron has kinetic energy greater than E_B, E_B is subtracted from the sum of the kinetic energies of both electrons. The directions of the electrons after EII are treated as being the same as the electrons after Møller scattering.

In this study, only K-shell ionization by electron impact was treated; also, neither L, M and outer-shell ionization by electron impact nor any shell ionization by positron impact was treated.

4 Comparison of the Calculation and Measurement

To verify the implementation of EII to the EGS4 code, we simulated i) the photon spectra, which consists of bremsstrahlung and the K-X ray [43, 44] and ii) the K-X ray yield [45]. We did not apply any normalization between the measurement and the calculation, and compared them in absolute values.

The calculation conditions were as follows. The EGS4 calculations were performed both with and without EII, referred to as EGS4+EII and EGS4, respectively hereafter. The improvements of EGS4(PRESTA [40], the use of the ICRU-37/NBS radiative stopping powers [41] and the improved angular distribution of bremsstrahlung photons [42]) were employed in all of the EGS4 calculations. The calculation geometry is shown in Fig. 2. Particle splitting was applied to EII-induced K-X rays and photoelectric effect-induced K-X rays to the increase efficiency of the K-X ray calculation.

4.1 Photon spectra from a Sn target

An additional condition for the calculation is as follows. A 100 keV electron beam is incident normally on a Sn target, which is an infinite slab of 21.6 mg/cm^2 thickness. Photons are scored when they reach the target surface (Plane 1 and 2 in Fig. 2). The scoring angular regions are θ=65-75°, 105-115°, respectively. The calculated photon spectra are smeared by a Gaussian function (FWHM=8 keV) in order to account for the resolution of the scintillation detectors. This FWHM value is arbitrary determined to fit the calculation to the measurement.

The calculated photon spectra was compared with Placious's measurement. Placious published a measurement of the bremsstrahlung photon spectra from various targets for the incidence of 50

or 100 keV electrons [43]. The error in the measurement is ±10% for Z=13, 50 and ±15% for Z=79. The contribution of K-X rays was removed from the photon spectra in order to show only the bremsstrahlung photon. Two spectra in this measurement have been published by Berger, while contribution of the K-X ray was not removed [44]. These spectra are referred to as Placious's measurement in this paper. In Placious's measurement, a 100 keV electron beam incident was normally on Sn targets (target thickness, 21.6 mg/cm^2). The photons emitted from the targets toward 70° and 110° from the direction of the incident electron were measured by a scintillation spectrometer. These photons consist of bremsstrahlung radiation and K-X rays.

The calculated photon spectra are shown in Fig. 3 together with Placious's measured value. Only the calculation result using Casnati's EII cross section is shown to obtain clearance in the figure. The K-X ray yield by EGS4 with Casnati's EII cross section agrees with the measurement within 10% in the spectra at both 70° and 110°. The calculation result using Gryziński's cross section gives a 12% lower yield of K-X rays. After smearing, K-X rays are seen to be underestimated by a factor of 2 if EII is neglected. Before smearing, the underestimation of K-X rays due to neglecting EII is a factor of 3 and 5 for θ = 70° and 110°, respectively. The calculated yield of bremsstrahlung photons is not affected by a consideration of EII. Bremsstrahlung photons were underestimated by ≈ 30%. Also, an EGS4 calculation with EII agrees well with an ETRAN calculation, which also considers EII [44].

4.2 K-X ray yield

Dick et al. measured the K-X ray yield from various targets for an incident electron beam of 0.01 to 3 MeV [45]. Among them, the K-X ray yield from Al, Ti, Cu, Ag and Au target measured at θ = 180° and 120° is simulated by the improved EGS4 code. In this measurement, electron beams of 10, 20, 50, 100, 500 keV and 1.5 and 3.0 MeV were normally incident on the target. Dick et al. stated that the uncertainty in the number of K-X ray photons and that in the incident electrons are less that 2% and about 1%, respectively. Dick et al also stated that targets having a the thickness equal to or greater than the electron range were used in the measurement.

The additional conditions for the calculation are as follows. The target thickness is set as being 1.2-times the electron range (Table IV of [45]). When the K-X ray is produced after EII or the photoelectric effect in the EGS4 calculation, a K-X ray flag is set to this K-X ray. Photons with the K-X ray flag are scored when they reach the target surface (Plane 1 in Fig. 2). The scoring angular regions are 170-180° and 115-125°, respectively. The energy spectra of the scored photons consist of monochromatic K-X ray peaks and a small tail at lower energy due to the Compton scattering of K-X rays before escaping from the target. All of these photons are regarded as being K-X rays in the calculation, because both of the peaks and most of these tails are supposed to also be scored in measurement.

The calculated and measured K-X ray yields are shown in Fig. 4. The statistical error in the calculation is within 3% for EGS4+EII, 10% and 5% for EGS4 of Al and other targets, respectively. The geometric average of the ratio of the calculated K-X ray yield to the measured one is shown for each target in Table 1. The EGS4 calculation apparently becomes underestimated with decreasing Z of the target. C/M is only 0.0025 for Al, but C/M is 0.84 for Au. The degree of underestimation depends weakly on the electron incident energy and the scoring angle. The EGS4 results show the yield of K-X rays due to the photoelectric effect. EGS4+EII with Casnati's cross section (EGS4+EII(Ca)) agreed within 25% with the measurement for 41 points in all 62 comparisons. EGS4+EII with Gryziński's cross section (EGS4+EII(Gr)) agreed within 25% with measurements for 53 points in all 62 comparisons. Also, the C/M of EGS4+EII in Table 1 is close to unity, except for Ti in the case that Casnati's cross section is used.

From these comparisons, an improvement in the K-X ray yield in the EGS4 code is clearly shown. The reason for the difference between the measurement and the calculations is mentioned

Table 1: Geometric average of C/M of K-X ray yields. Ca and Gr means the calculation result using Casnati's and Gryziński's cross section, respectively.

Target	Al	Ti	Cu	Ag	Au
EGS4	0.0025	0.022	0.049	0.30	0.84
EGS4+EII(Ca)	1.06	1.35	1.10	1.06	1.12
EGS4+EII(Gr)	0.88	1.10	0.82	0.90	1.04

in Discussion.

5 Discussion

There are several possible reasons for the discrepancy in the measured K-X ray yield and the calculated one:

- EII cross section,
- Particle transport calculation,
- Measurement.

A calculation using Gryziński's cross section agrees with the measured K-X ray yield better than that using Casnati's cross section at an energy range above 1.5 MeV for Al and above 200 keV for Ti. A calculation using Casnati's cross section gave a larger value than did the measurement in these two cases. Casnati's formula is based on fitting the measured cross section. Since there has been no measurement of the EII cross section in these energy ranges, the validity of Casnati's cross section in these energy ranges is not known at all. We guess that Casnati's cross section is too large and that Gryziński's cross section is better than Casnati's cross section in these energy regions.

There is a big difference between the measurement and calculation in the lowest energy region for Ti, Cu, Ag and Au targets. In these energy regions, although there have been many cross-section measurements, the measured values differ from each other. Casnati's cross section and Gryziński's cross section are close to the maximum data and minimum data of the measurement, respectively. Casnati's cross section is generally slightly closer to the measurement than Gryziński's cross section. Some enhancement of the uncertainty in the measurement may occur, since these energies are the lowest energy for each target. For example, the measured K-X ray yields from a Cu target of 12 keV electron beam incident at $\theta = 180°$ and $\theta = 120°$ differs by a factor of 2. In this condition, K-X rays are generated in an isotropic fashion in the vicinity of the target surface. Thus, these two measured values should be almost the same. Accordingly, we guess that this difference by a factor of 2 implies the degree of enhancement of uncertainty in the measurement in this energy region. While the lower energy boundary of the EGS4 code is a few tens of keV [1], EGS4 runs down to 1 keV for light atoms without error. In these energy regions, the treatment of electron multiple scattering becomes difficult. Thus, some enhancement in the uncertainty of the particle transport calculation may also occur. Accordingly, it is hard to consider a single reason to explain the large difference in the lowest energy comparison for each target.

Judging from the K-X ray yield comparisons and cross section ones, the most recommendable EII cross section may be as follows:

- Above a few hundreds keV or 1 MeV for a low-Z target: Gryziński. For example, this energy region is above 1.5 MeV for Al, and above 200 keV for Ti.

- Above 100 MeV: Kolbenstvedt-revised.
- Near edge: Either Casnati or Griziński.
- Other area: Casnati.

Making a reliable data set of the EII cross section is necessary for more precise calculations.

Appendix ESIG evaluation in USTEP loop

This appendix is a revised version of Appendix B of Ref. [2] [1].

In a class-II simulation) of charged-particle transport, Møller scattering, Bhabha scattering and bremsstrahlung production are treated as separate interactions only when the produced particle energy is beyond some threshold, on the other hand soft collisions are treated as continuous energy loss. In the EGS4 code, the interaction cross section (Σ) is defined as either (Møller scattering cross section + bremsstrahlung cross section) or (Bhabha cross section + bremsstrahlung cross section) for an electron and a positron, respectively. One problem concerning this treatment is that the interaction cross section is energy dependent, and the electron and positron energy changes continuously. EGS4 has a correction capability for this problem. This correction is effective when the interaction cross section is an increasing function of the energy, but is not effective when the interaction cross section is a decreasing function of the energy. For example, the interaction cross section of Sn has its minimum value at around 5 MeV. Thus, the interaction cross section of Sn is not adequately evaluated below 5 MeV. This causes an underestimation of both the Møller scattering and bremsstrahlung. Also, this causes an underestimation of the electron-impact ionization, since the electron-impact ionization is sampled using the ratio of the electron-impact ionization to the Møller scattering in this study.

Two groups of the authors developed the methods to solve the underestimation of the Møller scattering and the bremsstrahlung. Ma and Nahum intensively studied the effect of this problem using their own algorithm [46]. Aarnio et al used maximum interaction cross section to determine interaction point in FLUKA [47].

In this study, Ma and Nahum's method is applied for this correction after including two modifications. The starting points for this correction is: "If there are *N(E)*-particles of energy E, the number of discrete event is $\Sigma(E)N(E)$". Here, $\Sigma(E)$ represents discrete event cross section. This is described in a differential equation:

$$\frac{dN}{dE} = -\Sigma(E)N(E). \tag{1}$$

For an analytical calculation, Eq.(1) is solved as:

$$N(E) = N_0 \exp\left(-\int_E^{E_0} \Sigma(E')dE'\right) = N_0 \exp\left(-\int_x^{x_0} \frac{\Sigma(E(x'))}{dE/dX(E(x'))}dx'\right). \tag{2}$$

Here, N_0 is the number of electrons when their energy is E_0.

In order to carry out an actual Monte-Carlo calculation, Eq(1) is rewritten as:

$$\frac{dN}{dE} = -\left(\frac{\Sigma(E)}{f\Sigma_0}\right) f\Sigma_0 N(E). \tag{3}$$

Here f is a Ma and Nahum's factor to make $(\Sigma(E)/f\Sigma_0) < 1$. And Σ_0 is an arbitary constant at this stage. The place of discrete event is sampled by:

[1] We revised Appendix B of Ref. [2] in Jan 1997, two month after the publication of [2].

1. Particle travels ($f\Sigma_0$DEMFP). DEMFP is calculated by $(-\log\xi)$. ξ is a random number between 0 and 1. Σ_0 is a descrete event cross section at the beginning of each USTEP.

2. When a descrete event occurs, another random number $\xi_2(0 < \xi_2 < 1)$ is used to reject that event if $(\Sigma(E)/f\Sigma_0) < \xi_2$.

The modified points are:

- The evaluation of Σ_0 is moved into the USTEP-loop.
- $\Sigma(E)$ is used as discrete event cross section when partice energy is E. This is the same way as the original EGS4 code does.

The following macro is used in the calculation to implement the modification described in this appendix.

```
REPLACE{;SIG=SIGO*RHOF;} WITH
{;IF(EKE.LE.3.*TE(MEDIUM))[FMFPCM=1.;]
ELSE[FMFPCM=1.+(EKE-3.*TE(MEDIUM))/(10.*TE(MEDIUM)+EKE*EKE);]
IF(LELEC.LT.0) [$EVALUATE SIGO USING ESIG(ELKE);]
ELSE ["E+"$EVALUATE SIGO USING PSIG(ELKE);]
SIG=SIGO*RHOF*FMFPCM;}

REPLACE {;]UNTIL (RFICT.LE.SIGF/SIGO);} WITH
{;]UNTIL (RFICT.LE.SIGF/(FMFPCM*SIGO));}
```

In Fig. 3, all the EGS4 results include this correction.

References

[1] W. R. Nelson, H. Hirayama and D. W. O. Rogers, *SLAC-265* (Stanford University, Stanford, 1985).

[2] Y. Namito and H. Hirayama, "Implementation of the electron impact ionization into the EGS4 code", Proc. of the 6th EGS4 User's Meeting in Japan, *KEK Proc. 96-10* (1996).

[3] Y. Namito, H. Hirayama and S. Ban, "Improvements of Low Energy Photon Transport in EGS4", Proc. of the 1st International Workshop on EGS4, *KEK Proc. 97-16* (1997).

[4] M. Gryziński, *Phys. Rev.* **138** (1965) A305., *Phys. Rev.* **138** (1965) A322., *Phys. Rev.* **138** (1965) A336.

[5] H. Kolbenstvedt, *J. of Appl. Phys.* **38** (1967) 4785.

[6] D. L. Webster, W. W. Hansen and F. B. Duveneck, *Phys. Rev.* **43** (1933) 839.

[7] J. C. Clark, *Phys. Rev.* **48** (1935) 30.

[8] W. Hink and A. Ziegler, *Z. Phys.* **226** (1969) 222.

[9] J. W. Motz and R. C. Placious, *Phys. Rev.* **136** (1964) A662.

[10] H. Hansen and A. Flammersfeld, *Nucl. Phys.* **79** (1966) 135.

[11] D. H. Rester and W. E. Dance, *Phys. Rev.* **152** (1966) 1.

[12] K. H. Berkner, S. N. Kaplan and R. V. Pyle, *Bull. Am. Phys. Soc.* **15** (1970) 786.

[13] L. M. Middleman, R. L. Ford and R. Hofstadter, *Phys. Rev.* **2** (1970) 1429.

[14] D. V. Davis, V. D. Mistry and C. A. Quarles, *Phys. Let.* **38A** (1972) 169. C. A. Quales, Private communication: ω_K(Cu)=0.454 is used in Davis et al. (1972) *ibid.*

[15] H. Hübner, K. Ilgen and K. -W.Hoffmann, *Z. Phys.* **255** (1972) 269.

[16] W. Scholz, A. Li-Scholz, R. Cólle and I. L. Preiss, *Phys. Rev. Let.* **29** (1972) 761. A. Li-Scholz, R. Cólle, I. L. Preiss, W. Scholz, *Phys. Rev. A* **7** (1973) 1957.

[17] H. Tawara, K. G. Harrison and F. J. De Heer, *Physica* **63** (1973) 351.

[18] S. A. H. Seif el Nasr, D. Berényi and G. Bibok, *Z. Physik* **267** (1974) 169.

[19] G. R. Dangerfield and B.M. Spicer, *J. Phys. B* **8** (1975) 1744.

[20] K. Ishii, M. Kamiyama, K. Sera, S. Morita, H. Tawara, M. Oyamada and T. C. Chu, *Phys. Rev. A* **15** (1977) 906.

[21] D. Berényi, G. Hock, S. Ricz, B. Schlenk and A. Valek, *J. Phys. B* **11** (1978) 709.

[22] D. H. H. Hoffmann, C. Brendel, H. Genz, W. Löw, S. Müller and A. Richter, *Z. Phys. A* **293** (1979) 187.

[23] M. Kamioya, A. Kuwako, K. Ishii, S. Morita and M. Oyamada, *Phys. Rev. A* **22** (1980) 413.

[24] K. Shima, *Phys. Let.* **77A** (1980) 237.

[25] K. Kiss, G. Kalman, J. Palinkas and B. Schlenk, *Acta. Phys. Hung.* **50** (1981) 97.

[26] H. Genz, C. Brendel, P. Eschwey, U. Kuhn, W. Löw, A. Richter and P. Seserko, *Z. Phys. A* **305** (1982) 9.

[27] R. Hippler, K. Saeed, I. McGregor and H. Kleinpoppen, *Z. Phys. A* **307** (1982) 83.

[28] C. Quarles and M. Semaan, *Phys. Rev. A* **26** (1982) 3147.

[29] H. Platten, G. Schiwietz and G. Nolte, *Phys. Lett.* **107A** (1985) 83.

[30] S. C. McDonald and B. M. Spicer, *Phys. Rev. A* **37** (1988) 985.

[31] J. Deiwiks, S. Helms, U. Brinkmann, R. Hippler, H. Schneider, I. Tobehn, F. Ebel, D. Segers and J. Paridaens, Proceedings of the 10th international conference on positron annihilation, Materials Science Forum 175-178 (1995) 951.

[32] Z. An, T. H. Li, L. M. Wang, X. Y. Xia and Z. M. Luo, *Phys. Rev. A* **54** (1996) 3067.

[33] W. Bambynek, B. Crasemann, R. W. Fink, H. -U. Freund, H. Mark, C. D. Swift, R. E. Price and P. Venugopala Rao, *Rev. Mod. Phys.* **44** (1972) 716.

[34] E. Casnati, A. Tartari and C.Baraldi, *J. Phys. B* **15** (1982) 155. E. Casnati, A. Tartari and C.Baraldi, *J. Phys. B* **16** (1983) 505.

[35] C. Jakoby, H. Genz and A. Richter, *Jounal de Physique Colloque C* **9** (1987) 487.

[36] S. Seltzer, in: Monte Carlo transport of Electron and Photons, eds. T. M. Jenkins, W. R. Nelson and A. Rindi (Plenum, New York, 1988), 103.

[37] J.H. Scofield, *Phys. Rev. A* **18** (1978) 963.

[38] Ed: C. M. Lederer and V. S. Shirley, "Table of Isotopes 7th ed.", (Wiley-Interscience, New York, 1978) Table.10.

[39] H. Hirayama and D. K. Trubey, *Nucl. Sci. Eng.* **99** (1988) 145.

[40] A.F. Bielajew and D.W.O. Rogers, *PIRS No.042* (NRCC 1986). A.F. Bielajew and D.W.O. Rogers, *Nucl. Instrum. and Meth. B* **18** (1987) 165.

[41] D.W.O. Rogers, S. Duane, A.F. Bielajew and W.R. Nelson, *PIRS-0177* (NRCC, Ottawa, 1989).

[42] A.F. Bielajew, R. Mohan and C. Chui, *PIRS-0203* (NRCC, Ottawa, 1989).

[43] R. Placious, *J. Appl. Phys.* **38** (1967) 2030.

[44] M. J. Berger, in: Monte Carlo transport of Electron and Photons, eds. T. M. Jenkins, W. R. Nelson and A. Rindi (Plenum, New York, 1988) 216, Figure 8.27b. Berger cited Placious (1967) for the measurement. But in Placious (1967), only bremsstrahlung spectra are shown and no K-X ray are shown. Thus, it seems that Berger obtained spectra from Placious as a private communication and the experiment conditions is the same as shown in Placious (1967).

[45] C. E.Dick, A. C. Lucas, J. M. Motz, R. C. Placious, and J. H. Sparrow, *J. Appl. Phys.* **44** (1973) 815.

[46] Chang-ming Ma and A. E. Nahum, *Nucl. Instrum. and Meth. B* **72** (1992) 319.

[47] P. A. Aarnio, et al, in: International conference on Monte Carlo simulation in high Energy and Nuclear Physics (MC93), eds. P. Dragovitsch, S. L. Linn and M. Burbank (World Scientific, 1993) 100.

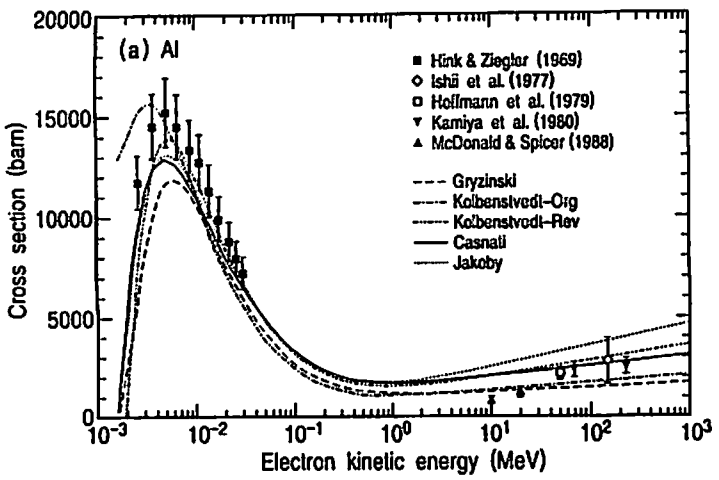

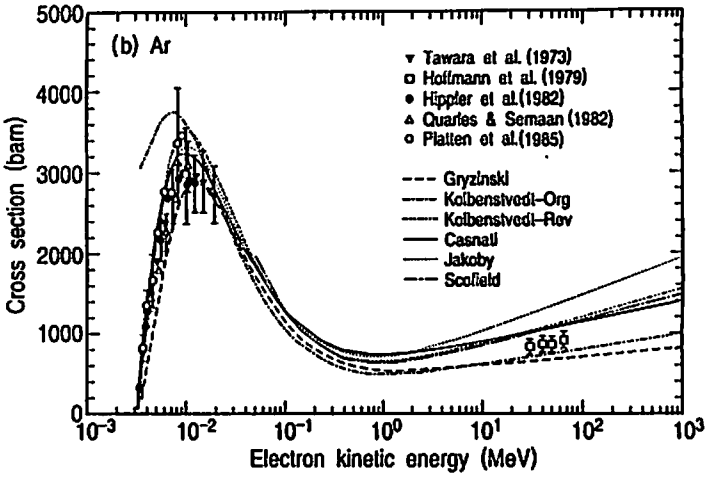

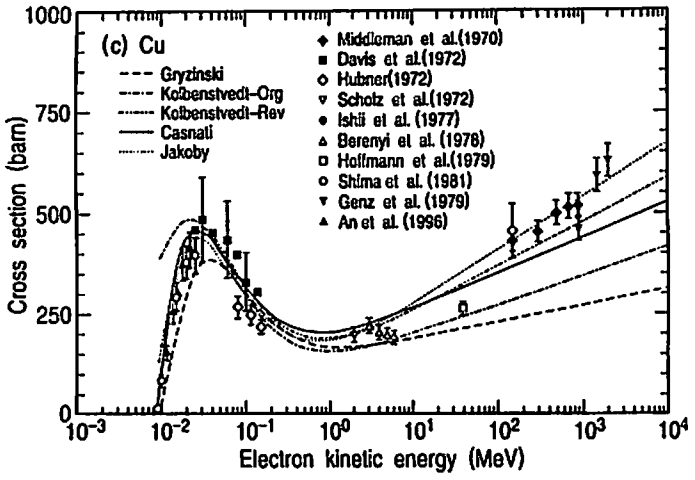

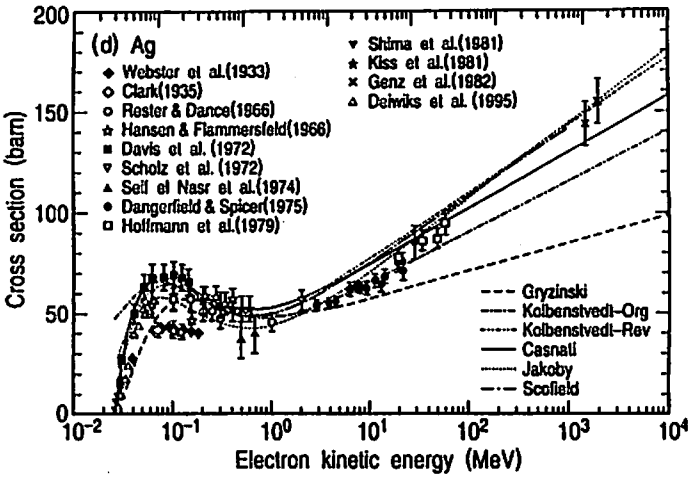

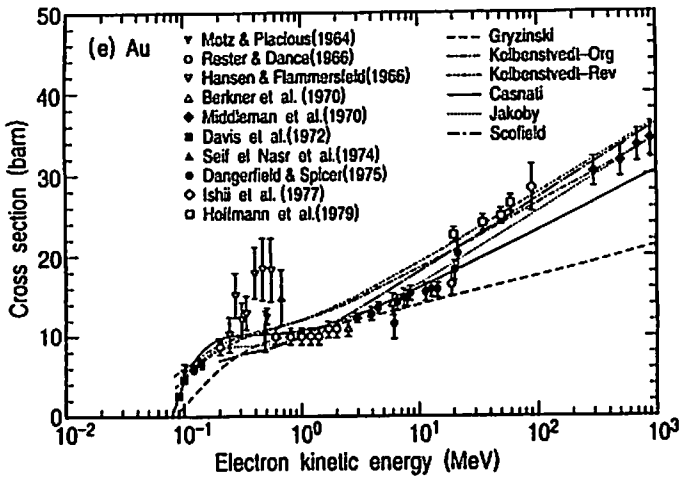

Fig. 1. K-shell electron-impact ionization cross sections of (a) Al, (b) Ar, (c) Ti, (d) Cu (e) Ag and (f) Au targets. The measured and calculated values are indicated by the symbols and lines, respectively. Solid line, Casnati; Dashed line, Gryziński; Dotted line, Jakoby; Chain line, Kolbenstvedt-original; Double dot-chain line, Kolbenstvedt-revised; Long chain line, Scofield (Ar, Ag and Au only).

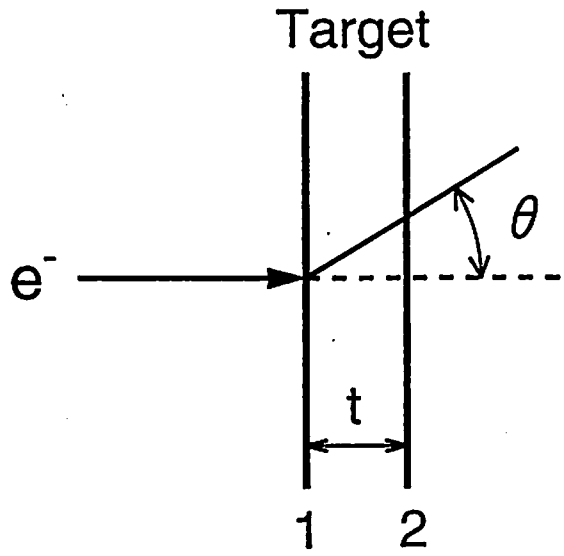

Fig.2. Geometry for the calculation. An electron beam incident on a target normally. The target is an infinite plate of thickness t, which is defined by planes 1 and 2. The angle θ is measured from the electron-beam direction.

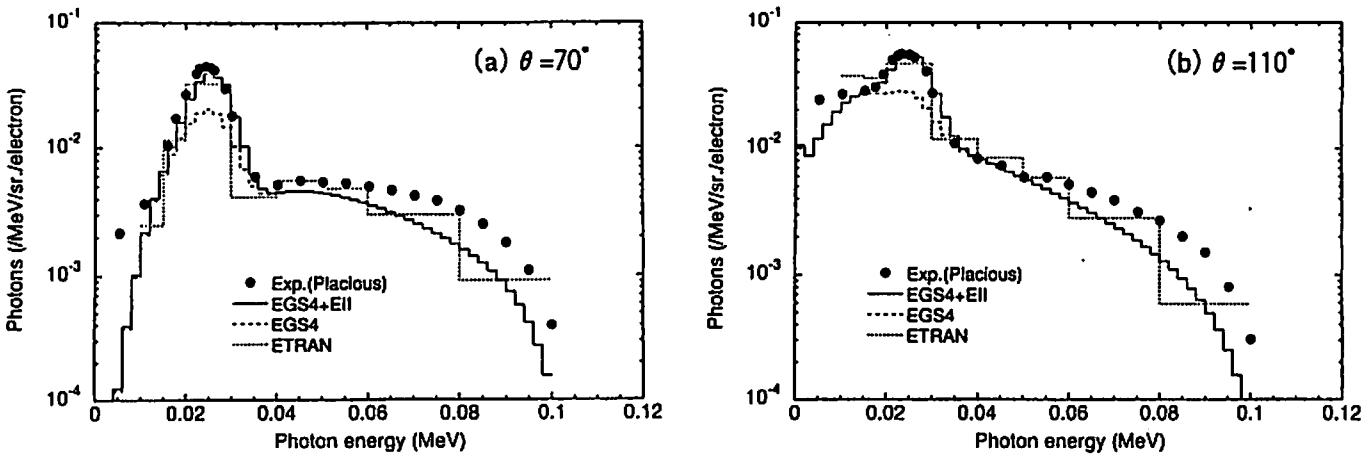

Fig. 3. Spectra of the bremsstrahlung and K-X rays from a Sn target (21.6 mg/cm^2) toward (a) $\theta = 70°$ and (b) $\theta = 110°$, respectively. A 100 keV electron beam is normally incident on the target. The closed circle indicates a measurement by Placious. The solid and dashed lines indicates the EGS4 calculation with EII using Casnati's cross section and without EII. The solid and dashed lines overlap above 40 keV. The dotted line shows the ETRAN calculation.

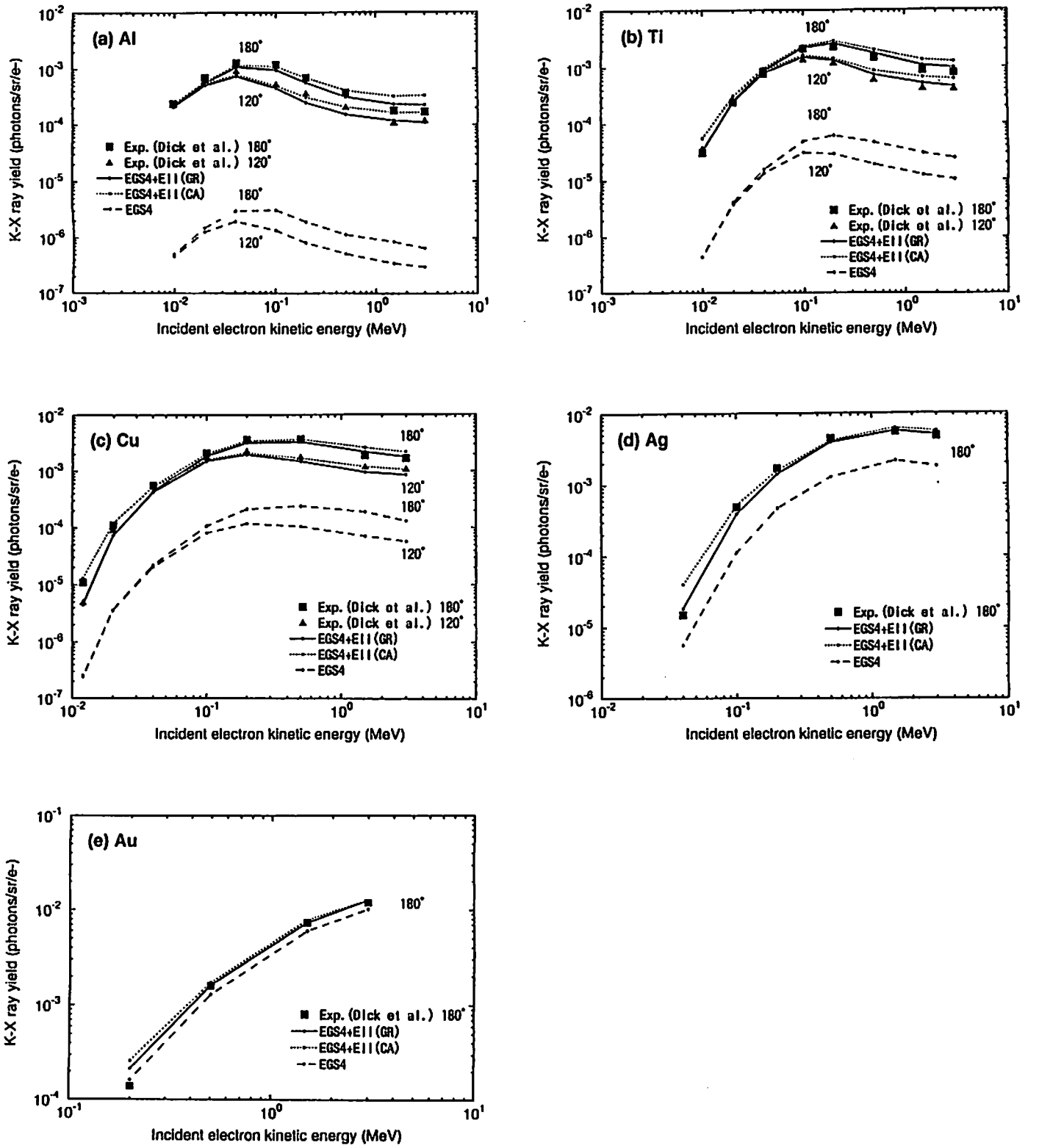

Fig. 4. Comparison of the K-X ray yield. The measured values by Dick et al. are indicated by filled boxes (θ = 180°) and filled triangles (θ = 120°). EGS4: EGS4 calculation without EII; EGS4+EII(GR): EGS4 calculation with EII using Gryziński's cross section; EGS4+EII(CA): that using Casnati's cross section. (a) Al (b) Ti (c) Cu (d) Ag (e) Au.

PROPERTY OF MOLIÈRE ANGULAR DISTRIBUTION WITH IONIZATION

T. NAKATSUKA

Okayama Shoka University
Tsushima-Kyomachi, Okayama 700-8601 Japan

Abstract

The solution for Molière angular distribution is improved to take into account ionization loss. The Kamata-Nishimura formulation of Molière theory is used and the translation formula between the above formulation and the Molière-Bethe one is devised. The result also is described by the usual Molière distribution with some smaller expansion parameter B and some larger unit of Molière angle compared with those without ionization. The structure of solution and the property of distribution are also investigated.

1 Introduction

The theory of multiple Coulomb scattering is important to trace passages of charged particle in computer simulations by Monte Carlo method [1, 2, 3, 4, 5]. There have been long history of studying multiple Coulomb scattering process [6]. Among those works, Molière theory [7, 8, 9, 10] is recognized one of the most advanced and representative taking into account single and plural scatterings other than multiple scatterings in the theory.

Although Molière theory keeps high accuracy and sophisticated mathematical contents, it was a defect that almost no improvement had been achieved after the submissions of angular and lateral distributions by himself [7, 8, 9]. We should remind there have been another formulation of Molière theory [11]. Kamata and Nishimura proposed a method to realize the Molière theory in the differential stage [12, 13]. By their method we can easily innovate the multiple scattering theory under the gaussian approximation [14] to that under the Molière theory. There exists a translation formula between the both method [15] and they are mathematically equivalent. By using their formulation, Kamata and Nishimura accomplished their cascade shower theory taking account of single and plural scatterings [12, 13] and the author investigated the effect of single and plural scatterings on the path-length problem under the multiple scattering process [15].

Molière gave the angular distribution of charged particle of a fixed energy. In practical cases, charged particles of moderately relativistic energy lose their energy almost at a constant rate during their passage by ionization process [16], so that they receive more effects from multiple scattering process than Molière's predictions. Due to this insufficiency of the theory in main we couldn't take long step sizes at tracing charged particles in Monte Carlo simulations, and this fact have decreased the accuracy of the results and disturbed the effective carrying out of computer simulations [1, 17].

So we attempted taking into account ionization effect in the diffusion equation of multiple scattering process under the Kamata-Nishimura formulation of Molière theory and got the solution. Through a translation formula devised this time our solution is reduced to the Molière-Bethe

solution, and the angular distributions with ionization loss are also represented by the familiar Molière distribution with the expansion parameter for some smaller step size and with the Molière angle of some larger unit in the practical step-size region.

2 Multiple Scattering Theory with Ionization Loss

The diffusion equation for the angular distribution of charged particles after receiving multiple Coulomb scattering with ionization becomes

$$\frac{\partial f}{\partial t} = \iint \{f(\vec{\theta} - \vec{\theta'}) - f(\vec{\theta})\}\sigma(\vec{\theta'})d\vec{\theta'} + \varepsilon\frac{\partial f}{\partial E}, \tag{1}$$

where t means thickness of traverse measured in radiation unit [14] and ε means critical energy or loss of energy in each unit radiation length [14]. If we assume axial symmetry of single scatterings, there satisfies

$$\sigma(\vec{\theta}) = \sigma(\theta), \tag{2}$$

so that the double Fourier transforms of Eq. (1) becomes

$$\frac{\partial \tilde{f}}{\partial t} = -2\pi\tilde{f}\int_0^\infty \theta d\theta[1 - J_0(\zeta\theta)]\sigma(\theta) + \varepsilon\frac{\partial \tilde{f}}{\partial E}. \tag{3}$$

Under the Kamata-Nishimura formulation of Molière theory, the diffusion equation becomes

$$\frac{\partial \tilde{f}}{\partial t} = -\frac{K^2\zeta^2}{4p^2v^2}\tilde{f}\{1 - \frac{1}{\Omega}\ln\frac{K^2\zeta^2}{4p^2v^2}\} + \varepsilon\frac{\partial \tilde{f}}{\partial E}, \tag{4}$$

where K and Ω are the scattering constants specific to the material defined by Kamata and Nishimura [12, 13].

At first we approximate the coefficient pv appearing in the single scattering formula by E:

$$pv = E\{1 - (\frac{mc^2}{E})^2\} \simeq E, \tag{5}$$

which is allowed when the rest mass is enough smaller than E (referred to as *massless approximation*). If we regard the dependence of t on E,

$$t = \frac{1}{\varepsilon}(E_0 - E), \tag{6}$$

then the last differential term of the equation vanishes and we get

$$\varepsilon\frac{\partial \ln \tilde{f}}{\partial E} = \frac{K^2\zeta^2}{4E^2}\{1 - \frac{1}{\Omega}\ln\frac{K^2\zeta^2}{4E^2}\}. \tag{7}$$

The solution of the differential equation satisfying the initial condition of

$$\tilde{f} = \frac{1}{2\pi} \qquad \text{at} \qquad E = E_0 \tag{8}$$

becomes

$$\begin{aligned}\tilde{f} &= \frac{1}{2\pi}\exp\{\frac{K^2\zeta^2}{4E_0\varepsilon}(1 + \frac{2}{\Omega} - \frac{1}{\Omega}\ln\frac{K^2\zeta^2}{4E_0^2}) - \frac{K^2\zeta^2}{4E\varepsilon}(1 + \frac{2}{\Omega} - \frac{1}{\Omega}\ln\frac{K^2\zeta^2}{4E^2})\} \\ &= \frac{1}{2\pi}\exp\{-\frac{K^2\zeta^2 t}{4E_0E}[1 + \frac{1}{\Omega}(2 - \frac{E_0 + E}{E_0 - E}\ln\frac{E_0}{E}) - \frac{1}{\Omega}\ln\frac{K^2\zeta^2}{4E_0E}]\}.\end{aligned} \tag{9}$$

3 A Translation Formula Between the Kamata-Nishimura Formulation and the Molière-Bethe One

Let the solution of the equation under the Kamata-Nishimura formulation have a form [18] of

$$\tilde{f} = \frac{1}{2\pi}\exp\{-a\zeta^2 + b\zeta^2\ln(c\zeta^2)\}. \tag{10}$$

If we can determine B by the equation

$$B - \ln B = \frac{a}{b} - \ln\frac{c}{b}, \tag{11}$$

then Eq. (10) can be translated to the Molière solution:

$$\tilde{f} = \frac{1}{2\pi}\exp\{-\frac{u^2}{4}(1 - \frac{1}{B}\ln\frac{u^2}{4})\}, \tag{12}$$

where

$$u = 2\zeta\sqrt{bB}. \tag{13}$$

Thus, applying Hankel transforms we get the Molière expansion for the angular distribution:

$$f(\vartheta) = f^{(0)}(\vartheta) + B^{-1}f^{(1)}(\vartheta) + B^{-2}f^{(2)}(\vartheta) + \ldots, \tag{14}$$

where the Molière angle is defined by

$$\vartheta = \theta/(2\sqrt{bB}). \tag{15}$$

4 The Distribution under the Massless Approximation

Coefficients of the solution under the massless approximation are

$$a = \frac{K^2 t}{4E_0 E}, \tag{16}$$

$$b = \frac{1}{\Omega}\frac{K^2 t}{4E_0 E}, \tag{17}$$

$$c = e^{-2}(\frac{E_0}{E})^{\frac{E_0+E}{E_0-E}}\frac{K^2}{4E_0 E}. \tag{18}$$

If we define the scale factor ν for the traversed thickness as

$$\nu = e^2(\frac{E}{E_0})^{\frac{E_0+E}{E_0-E}}, \tag{19}$$

then the solution can be reduced to the Molière expansion with parameter B of

$$B - \ln B = \Omega - \ln\{\Omega/(\nu t)\}. \tag{20}$$

The Molière angle is new defined by

$$\vartheta = \theta/\theta_{\mathrm{M}}, \tag{21}$$

where the unit of Molière angle is

$$\theta_{\mathrm{M}} = \frac{K\sqrt{t}}{\sqrt{E_0 E}}\sqrt{\frac{B}{\Omega}}. \tag{22}$$

The scale factor ν under the massless approximation is a function of fraction of residual energy $(E_0 - E)/E_0$ or fractional thickness $t/(E_0/\varepsilon)$ [19], as plotted in Fig. 1.

5 Molière Angular Distribution with Ionization

We will obtain the accurate solution of Eq. (4), which indicates Molière angular distribution taking account of ionization loss of a constant rate with traversed thickness. The equation can be written as

$$\frac{\partial \tilde{f}}{\partial t} = -\frac{\zeta^2}{w^2}\tilde{f}\{1 - \frac{1}{\Omega}\ln\frac{\zeta^2}{w^2}\} + \varepsilon\frac{\partial \tilde{f}}{\partial E}, \tag{23}$$

where we used Fermi coefficient w [14] with the scattering energy E_s replaced by K:

$$w = 2pv/K. \tag{24}$$

w is a function of E and if we regard the dependence of E on t by

$$E = E_0 - \varepsilon t, \tag{25}$$

the last term of the right-hand side of Eq. (23) vanishes. If we assume imaginary material whose K is finite and Ω diverges, then Eq. (23) gives the solution under the gaussian approximation [14] with the mean square angle of

$$\theta_G^2 = \int_0^t \frac{4}{w^2}dt. \tag{26}$$

We assume the structure of solution as same as that under the massless approximation, by introducing a new unknown scale factor ν:

$$\tilde{f} = \frac{1}{2\pi}\exp\{-\frac{\theta_G^2\zeta^2}{4}(1 - \frac{1}{\Omega}\ln\frac{\theta_G^2\zeta^2}{4\nu t})\}. \tag{27}$$

Then we get the ordinary diffusion equation for ν with a known inhomogeneous term:

$$\frac{\partial}{\partial t}\ln(\nu t) + \frac{4}{w^2\theta_G^2}\ln(\nu t) = \frac{4}{w^2\theta_G^2}(1 - \ln\frac{4}{w^2\theta_G^2}). \tag{28}$$

The solution of the equation becomes

$$\begin{aligned}\ln(\nu t) &= \exp\{-\int\frac{4dt}{w^2\theta_G^2}\}\int_0^t[\frac{4}{w^2\theta_G^2}(1 - \ln\frac{4}{w^2\theta_G^2})\exp\{\int\frac{4dt}{w^2\theta_G^2}\}]dt \\ &= 1 - \frac{1}{\theta_G^2}\int_0^t\frac{4}{\theta_G^2}\ln\frac{4}{w^2\theta_G^2}dt.\end{aligned} \tag{29}$$

So we get the explicit expression for the scale factor:

$$\nu = \frac{\theta_G^2}{4t}\exp\{\frac{4}{\theta_G^2}\int_0^t\frac{\ln w^2}{w^2}dt\}. \tag{30}$$

Thus we get the Molière angular distribution with ionization loss by the traditional Molière expansion with the parameter B from Eq. (20) and Eq. (30), where the unit of Molière angle is defined by

$$\theta_M = \theta_G\sqrt{B/\Omega} \tag{31}$$

and the gaussian mean square angle is explicitly expressed [20] by

$$\theta_G^2 = \frac{K^2}{2\varepsilon}\{\frac{1}{pv} - \frac{1}{p_0v_0} + \frac{1}{2mc^2}\ln\frac{(E_0 - mc^2)/(E - mc^2)}{(E_0 + mc^2)/(E + mc^2)}\}. \tag{32}$$

The scale factor ν this time is a function of $E_0/(mc^2)$ and $E/(mc^2)$. ν gradually decreases from the initial value of 1 with increase of traversed thickness and finally it rapidly falls to zero with dissipation of its kinetic energy, as indicated in Fig. 1 for $E_0/(mc^2)$ of 10, 20, and 50.

6 Recipe for Getting Molière Angular Distribution with Ionization

We summarize here the sequence of getting the Molière angular distribution with ionization $f(E_0, t, \theta)\theta d\theta$ of charged particles starting with incident energy of E_0 and having traversed thickness of x in g/cm^2 or $t = x/X_0$ in radiation unit [14].

At first we should get the scale factor ν,

$$\nu = \frac{\theta_G^2}{4t} \exp\{\frac{4}{\theta_G^2} \int_0^t \frac{\ln w^2}{w^2} dt\},$$

where the gaussian mean square angle θ_G^2 is

$$\theta_G^2 = \frac{K^2}{2\varepsilon}\{\frac{1}{pv} - \frac{1}{p_0 v_0} + \frac{1}{2mc^2} \ln \frac{(E_0 - mc^2)/(E - mc^2)}{(E_0 + mc^2)/(E + mc^2)}\},$$

and

$$w = 2pv/K \quad \text{and} \quad E = E_0 - \varepsilon t.$$

Then we can get our distribution by the usual Molière function:

$$f(E_0, t, \theta)\theta d\theta = [f^{(0)}(\vartheta) + B^{-1} f^{(1)}(\vartheta) + B^{-2} f^{(2)}(\vartheta) + \cdots]\vartheta d\vartheta,$$

where the Molière expansion parameter B is got by

$$B - \ln B = \Omega - \ln\{\Omega/(\nu t)\},$$

and the Molière angle is defined by

$$\vartheta = \theta/\theta_M \quad \text{and} \quad \theta_M = \theta_G \sqrt{B/\Omega}.$$

The parameters K and Ω are the scattering constants defined by Kamata and Nishimura [12, 13].

7 Characteristic Feature of Molière Angular Distribution with Ionization

We discuss the case of angular distributions of charged particle of energy E_0 to penetrate material with ionization. The new expansion parameter B is determined by the product of the thickness of material and the new introduced scale factor ν. The scale factor decreases gradually from 1 with traversed thickness and later rapidly falls to zero with the dissipation of kinetic energy as indicated in Fig. 1. So the product νt, hence the expansion parameter B which is an increasing function of νt, grows at first with traversed thickness, later reaches to its peak, and falls at the last stage before dissipation of the kinetic energy, though the violation to the small angle approximation may occur at the last stage [19]. On the other hand the unit of Molière angle is determined by the product of gaussian root mean square angle θ_G, which grows monotonously with traverse, and the square root of the ratio of expansion parameter B determined above to Ω. So we can recognize the shape of Molière angular distribution becomes old much slowly, on the other hand the unit of Molière angle becomes large much rapidly due to ionization, in the practical step-size region of penetration before violations to the small angle approximation.

We can get a rather simple understanding of transition of the angular distribution under the massless approximation. We compare the angular distributions of charged particle penetrating with

a fixed incident energy through various materials of a fixed thickness of traverse measured in unit of g/cm^2. Charged particles lose almost the same energy irrespective of materials and they have almost the same fractional energy and fractional thickness. So that they have almost the same scale factor ν. Radiation length X_0 decreases with the atomic number so that the traversed thickness in radiation unit increases with the atomic number. So the expansion parameter B becomes large and the shape of the angular distribution becomes old with the atomic number. On the other hand the gaussian mean square angle θ_G^2 increases with thickness in radiation unit as easily confirmed in Table V of Ref. [19], hence with the atomic number. So if charged particles traverse various materials of the same thickness in g/cm^2, the shape of angular distribution grows old and the unit of Molière angle increases with the atomic number of material.

8 Conclusions

We have got the Molière angular distribution taking account of ionization loss of a constant rate with traversed thickness. The distribution is reduced to the traditional Molière expansion, with some smaller expansion parameter B and some larger unit of Molière angle θ_M in the practical step-size region. Using the new distribution we can make more accurate analyses of experiments concerning charged particles and more accurate tracing of charged particles in computer simulations by slight alterations of existing tools.

References

[1] M. Messel and D.F. Crawford, *Electron-Photon Shower Distribution Function Tables for Lead Copper and Air Absorbers* (Pergamon, Oxford, 1970).

[2] W.R. Nelson, H. Hirayama, and D.W.O. Rogers, "The EGS4 Code System," SLAC-265, Stanford Linear Accelerator Center (Dec. 1985).

[3] J.A. Halbleib and T.A. Mehlhorn, ITS: The integrated Tiger Series of coupled electron/photon Monte Carlo transport codes, Sandia National Laboratories report SAND84-0573(1984).

[4] J.S. Hendricks and J.F. Breismeister, IEEE Trans. Nucl. Sci. **39**, 1035(1992).

[5] S.M. Seltzer, Appl. Radiat. Isot. (Int. J. Radiat. Appl. Instrum. Part A) **42**, 917(1991).

[6] W.T. Scott, Rev. Mod. Phys. **35**, 231(1963).

[7] G. Molière, Z. Naturforsch. **2a**, 133(1947).

[8] G. Molière, Z. Naturforsch. **3a**, 78(1948).

[9] G. Molière, Z. Naturforsch. A **10A**, 177(1955).

[10] H.A. Bethe, Phys. Rev. **89**, 1256(1953).

[11] T. Nakatsuka, *Proc. of RIKEN Intern. Workshop on Electromagnetic and Nuclear Cascade Phenomena in High and Extremely High Energies, RIKEN 1993*, p. 258.

[12] K. Kamata and J. Nishimura, Prog. Theor. Phys. Suppl. **6**, 93(1958).

[13] J. Nishimura, in *Handbuch der Physik, Band 46*, edited by S. Flügge (Springer, Berlin, 1967), Teil **2**, p. 1.

[14] B. Rossi and K. Greisen, Rev. Mod. Phys. **27**, 240(1941).

[15] T. Nakatsuka, Phys. Rev. **D35**, 210(1987).

[16] Particle Data Group, Eur. Phys. J., **C3**, 1(1998).

[17] A.F. Bielajew and D.W.O. Rogers, Nucl. Instrum. Methods Phys. Res. **B18**, 165(1987).

[18] The determination of parameters a and c is not unique. We can put $a = 0$ or $c = 1$ without loss of generality, then the other is determined uniquely.

[19] T. Nakatsuka, Phys. Rev. **D58**, 5102(1998).

[20] T. Nakatsuka, K. Kobayakawa and T. Kitamura, *Proc. of Fouth Asia Pacific Physics Conference, Seoul 1990*, p. 1425.

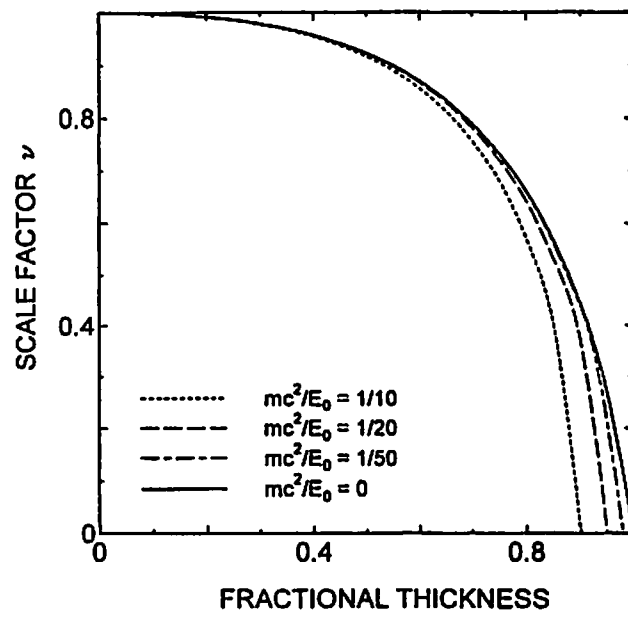

Figure 1: The scale factor ν vs the fractional thickness. Abscissa means $t/(E_0/\varepsilon)$.

EXPLICATION OF NEUTRON STREAMING PATH IN A DUCT STREAMING SYSTEM

Kohtaro UEKI and Masayoshi KAWAI[1]

Nuclear Technology Division, Ship Research Institute
6-38-1 Shinkawa, Mitaka, Tokyo 181-0004, Japan

[1]*High Energy Accelerator Research Organization, Neutron Science Laboratory*
1-1 Oho, Tsukuba, Ibaraki 305-0801, Japan

Abstract

In this study, the neutron streaming experiment with three straight ducts in the thick iron slab is analyzed with the Cell Flagging card. The ratios of the neutrons passed through the flagging cell set at the duct inlet to the total neutrons (flagged and non-flagged neutrons) are obtained as a function of the detector locations in the duct. In addition, the streaming system with a two-bend duct in the thick concrete slab is calculated. The neutron contributions from several flagging cells to the detector cell in the outlet of the duct was analyzed in the streaming system that has the two-bend duct in a thick concrete slab with a 14 MeV neutron source.

1 Introduction

In the Monte Carlo calculation, the history of a particle is tracked in a shielding system in accordance with the probability low, so that it enable us to recognize each course that the particles passed through. In the MCNP 4B code[1], the passage of a particle is recognized with the Cell Flagging card. Only the particles passed through the Flagging Cell or Surface are flagged and the other particles are not flagged. Accordingly, the flagged particles and the non-flagged particles are distinguished in the detector. In this study, the neutron streaming experiment with three straight ducts in the thick iron slab was analyzed with the Cell Flagging card. The ratios of the neutrons passed through the flagging cell set at the duct inlet to the total neutrons (flagged and non-flagged neutrons) were obtained as a function of the detector locations in the duct. In addition, the streaming system with a two-bend duct in the thick concrete slab was calculated. The contribution of neutrons passed through the flagging cells set in several locations around the duct to the detector located at the outlet of the duct was analyzed. Thus, the optimum location for setting a compensation shield[2] can be comprehended in the duct shielding system.

The streaming pass was clarified and the contribution from a certain part of a system was quantitatively analyzed with Monte Carlo method. The compensation shielding calculation to a duct streaming is established by the quantitative estimate so that the locational optimization of compensation shielding will be possibly expected.

2 Identification of the Streaming Path

At first, an identification technique of a neutron streaming path is discussed in multi-duct neutron streaming system. As a neutron streaming system, it is assumed that the neutron streaming system with three-straight ducts in Fig. 1. Neutrons radiated from the source at the inlet of the center duct stream in the ducts or penetrate through the streaming system, and some of them are detected by the detector located in the duct. The dose-equivalent rate or the energy spectrum is obtained with the detector located in the streaming system. However, the detector can not identify which ducts or parts of the duct the neutrons have passed through.

As mentioned above, the history of each particle is tracked with the probability low. Accordingly, it is possible to identify the paths of the particles and to distinguish the particles passed through the specified cell or surface located in the duct. In the MCNP 4B code, CF card (cell-flagging card) was used to specify the entrance cell that neutrons passed through and the detector cell was applied to calculate the contribution of neutrons from the flagged cell to the detector.
An example of using the CF card with MCNP 4B code is shown in fig. 1. A flagging cell is set at the duct inlet of the center duct and a detector cell is set at the duct outlet. The particles streaming from the neutron source passed through a flagging cell are distinguished from the others by flags as dotted lines shown in the fig. 1. The flags will be remained until the particles pass through the system or reduce the energy less than the cut off. Flagged particle and non-flagged particle are scored distinguishably at a detector cell and the total of the flagged and non-flagged particles, and the flagged particle are output respectively. The contribution of the particles streaming from other parts will be obtained by subtracting the flagging particles from the total ones at the detector cell. It is possible to set flagging cell and detector cell plurally. When flagging cell is plural, the flags are given to the particle as many as the flagging cells that the particles passed through. Accordingly, it is necessary to choose the flag number of the particle scored at the detector cell.

3 Application to the Three Straight Ducts Streaming Benchmark Experiment

The benchmark experiment of 14 MeV neutrons performed with OCTAVIAN of Osaka University[3] was analyzed with the CF card and the streaming pass was clarified. The three straight ducts are in a thick iron block as shown in Fig. 2, and the neutron source of 14 MeV is in the outside of the center duct inlet. The NE213 detector response to the neutrons higher than 1.47 MeV was analyzed with MCNP 4B code. The comparison between the experiment and the result of the analysis by Monte Carlo calculation in the outside duct, and the contribution to the outside duct of the neutron that passed the side duct inlet are described in Fig.3. ▲ shows the response of the NE213 and ○ shows the response of Monte Carlo calculation. ○ is not shown in the inlet of the outside duct (Distance = 0 cm) means the value of ○ is the same as ●.

As shown in Fig. 3, the Monte Carlo calculations slightly overestimate the experiment between the inlet and the outlet of the duct. The FSD's (fractional standard deviation) are not given to ○ in Fig. 3 and the others because they are smaller than the size of ○ (FSD $\leq$ 0.05). ● shows the contributions of the neutron passed through the side duct inlet to the NE213 detectors located in the places of ○ in the outside duct. For example, the contribution was 100% at 1.5-cm distance, where the NE213 detector is close to the inlet. It reduces to 26% at the distance 17-cm, to 10% at 62-cm, and to 9.5% at the 108-cm distance, which is close to the duct outlet.

4 Application to the Two-Bend Duct Streaming System

Fig. 4 shows the streaming system that has a 30-deg. two-bend duct in a 2-m thick concrete slab. A 14 MeV neutron source is located at 50 cm from the duct inlet. The distribution of the neutron dose-equivalent rates was calculated and it was compared with non-duct concrete. In addition, six flagging cells were located outside of the duct and contribution of each cell to the detector in the duct outlet was investigated.

The result of the calculation is described in the fig. 5 and fig. 6. Fig. 5 shows the distribution of neutron dose-equivalent rates in the 10 cm-diameter duct and in the concrete without duct. The dose-equivalent rate increased about by two times at 2 m from the inlet. This is caused mainly by the small size of the duct in the streaming system and by the 50-cm distance from the inlet to the point isotropic source. Fig. 6 shows the contribution of neutron dose-equivalent rate from the flagging cell to the detector cell located in the duct outlet as shown in Fig. 4.

Following considerations are clarified from Fig. 6.

1. The contribution of the neutron dose-equivalent rate from the flagging cell set in the duct inlet was about 10

2. The contribution of the neutron dose-equivalent rate from the flagging cell in the outside of the duct inlet was 30is same with the contribution from flagging cell 5 and flagging cell 6, and the contribution from the flagging cell in the duct inlet is relatively large although the 2-m distance from the outlet.

3. In this case, the polyethylene shielding will be optimum as compensation shielding at the outside of the inlet or outlet of a duct to reduce the streaming to duct outside effectively. The contribution of second gamma ray is not calculated, however, it is possible by the same method by using the CF card.

5 Conclusions

The streaming pass was clarified and the contribution from a certain part of a streaming system was quantitatively analyzed by using Monte Carlo method with the CF card applying to the benchmark experiment of 14 MeV neutrons. The contribution was 100% at 1.5-cm distance, where the NE213 detector is close to the inlet. It reduces to 26% at the distance 17-cm, to 10% at 62-cm, and to 9.5% at the 108-cm distance, which is close to the duct outlet.

The neutron contributions from several flagging cells to the detector cell in the outlet of the duct was analyzed in the streaming system that has a 30-deg. two-bend duct in a 2-m thick concrete slab with a 14 MeV neutron source at 50 cm from the duct inlet. The contribution of the neutron dose-equivalent rate from the flagging cell in the outside of the duct inlet was 30It was the same as the contribution from the flagging cells in the third leg.

Using this strategy, the locational optimization of compensation shielding will be possibly expected.

References

[1] F. Briesmeister, Editor, "MCNPTM - A General Monte Carlo N-Particle Transport Code Version 4B", *LA-12625-M*, (March 1997).

[2] Y. Oka, et al., "Benchmark Experiment of Fusion Neutron Streaming through Iron Shields", *OKTAVIAN Report A-88-01*, (July 1988).

[3] A. Yamaji, "Study on a Compensational Shield for Gamma Radiation to Maintain the Shielding Performance of a Shield Wall with Duct and Slit," Thesis, Papers of Ship Research Institute, Vol. 26, No. 6, (Nov. 1989).

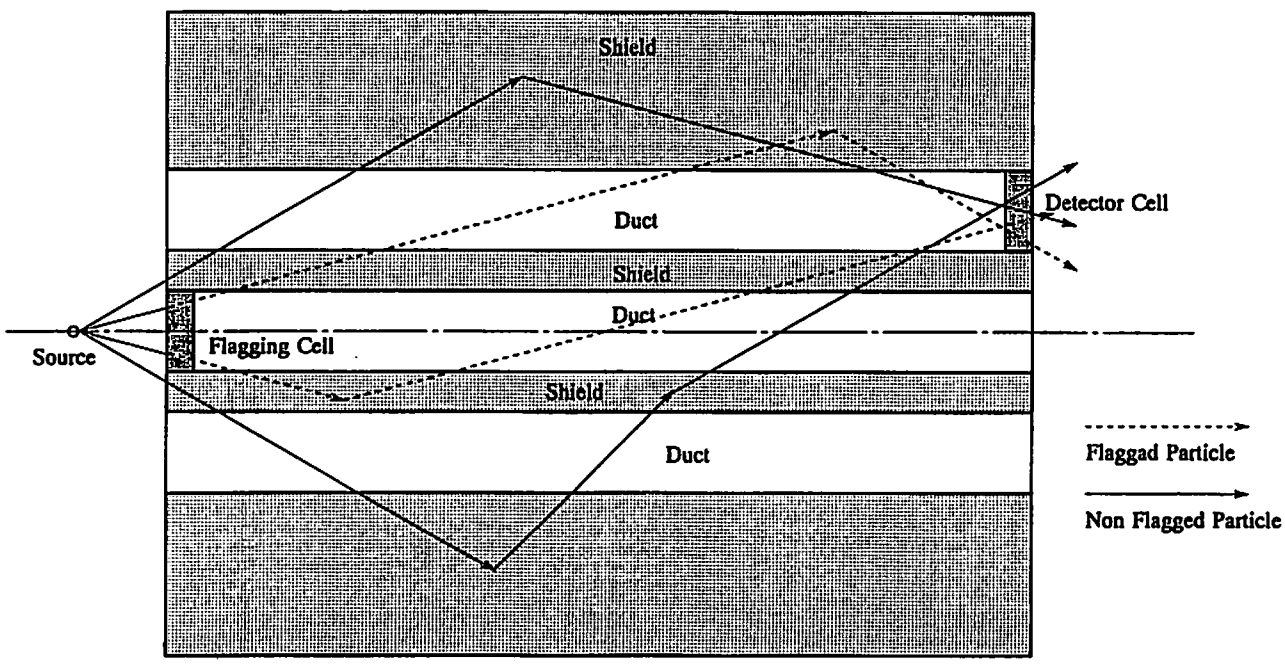

Fig. 1 Illustration of flagged and non flagged particles of the Cell-Flagging card in MCNP 4B code.

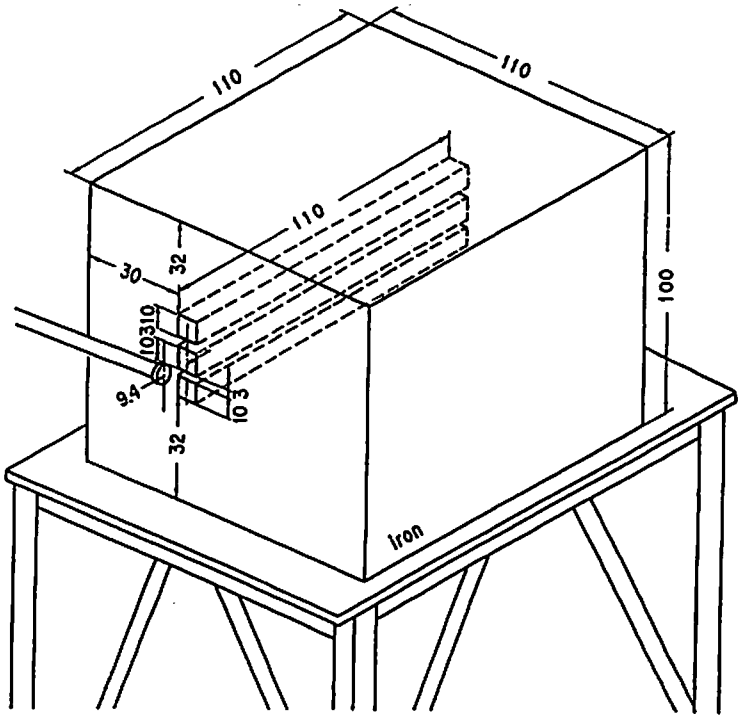

Fig. 2 Experimental arrangement of the three-ducts shielding system in the OCTAVIAN experiments with 14 MeV Neutrons. Dimensions are all in centimeters.

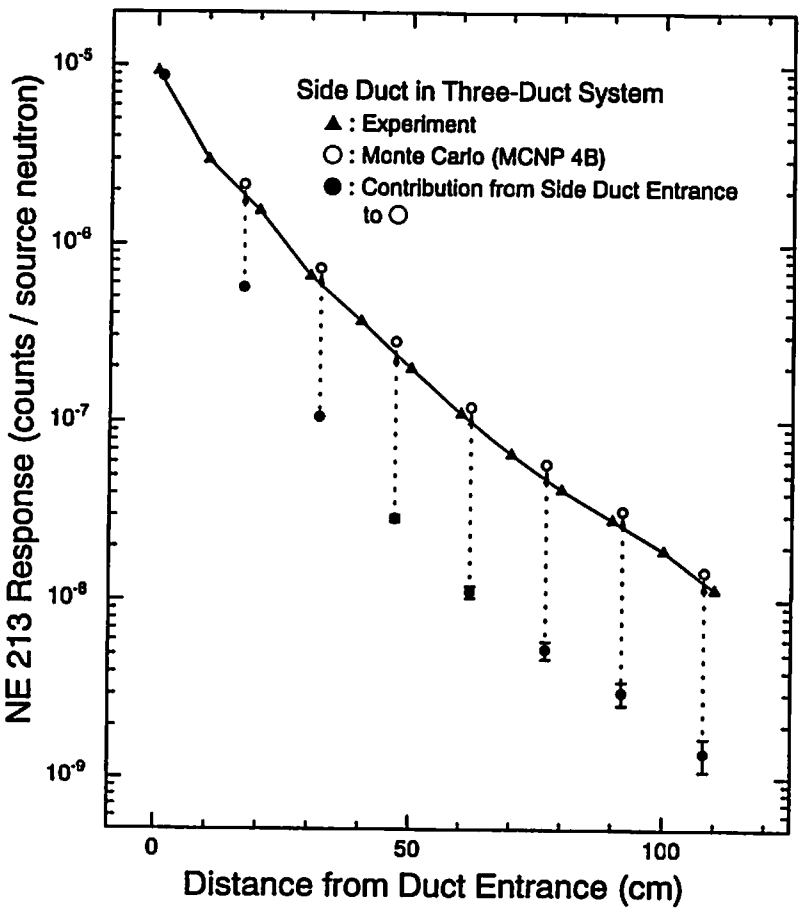

Fig. 3 Comparison of mesured and Monte Carlo analysis for NE 213 response in the side duct, and contribution profile of neutrons flagged at entrance of the side duct to detectors in the side duct of the system

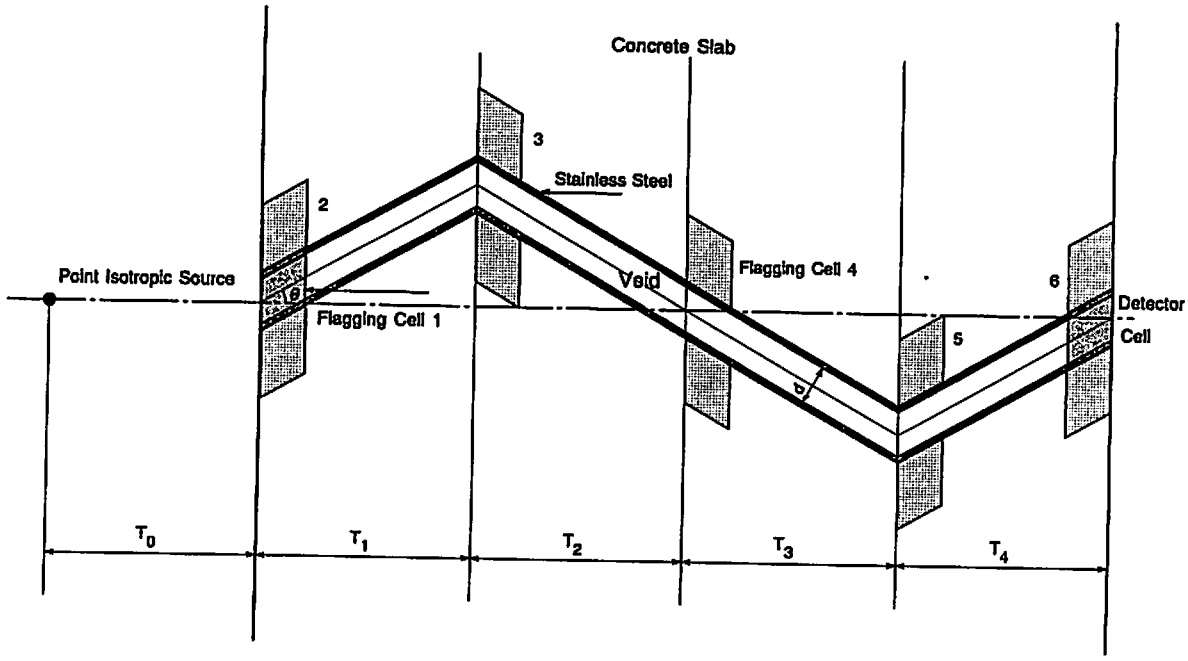

Fig. 4 Two-bend duct streaming problem. Source:14 MeV, θ=30 deg., d=10cm T_0=T_1=T_2=T_3=T_4=50cm.

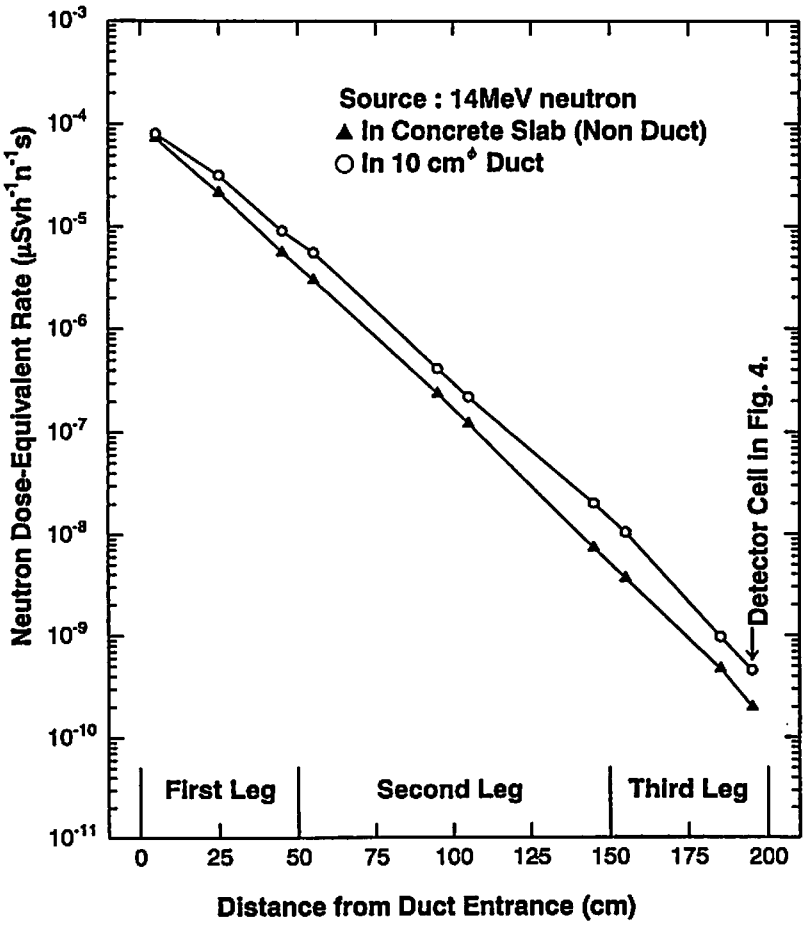

Fig. 5 Distribution of neutron dose-equivalent rates in the 30 deg. two bend duct of the concrete slab in Fig. 4.

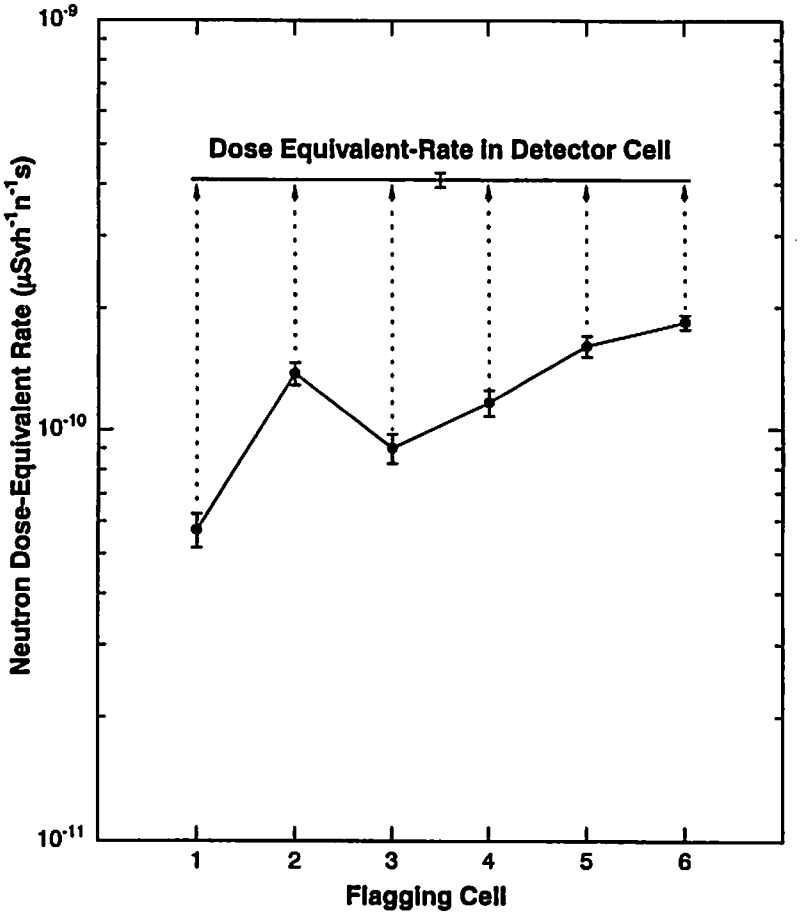

Fig. 6 Contribution of neutrons from each flagged cell to the detector cell at the duct end in Fig. 4.

SIMULATION STUDY OF A FARADAY-CUP MONITOR FOR SINGLE-BUNCH ELECTRON BEAMS

Tsuyoshi SUWADA

KEK, High Energy Accelerator Research Organization
1-1 Oho, Tsukuba-shi, Ibaraki-ken 305-0801, Japan

Abstract

A precise beam-charge measurement of single-bunch beams is being required for the KEKB injector linac in order to measure the precise beam-injection rate to the KEKB rings, and furthermore and to estimate the amount of beam-charge loss. In linac operation, wall-current monitors (WCMs) have usually been used to measure the amount of beam charges/pulse; however, it is difficult to measure the amount of beam charge for single-bunch beams with a pulse width of the order of 10 ps, since the WCMs show a strong frequency dependence upon the pulse width of the beams. Thus, a precise beam-charge measurement using a Faraday cup (FC) has been planned to measure the absolute amount of beam charge for a single-bunch beam by beam tests. This monitor can measure the absolute amount of beam charge by integrating them, and, thus, this method is independent of the beam-pulse width. Several characteristics of the FC are discussed based on a Monte-Carlo simulation using the EGS4 code. The analysis results give some necessary experimental conditions, such as the beam energy and the required vacuum pressure inside the FC for beam experiments. This report describes the characteristics of the FC, espacially, the estimation for the ionization effect, the leakage charges and backscattered charges from the monitor, etc. in detail.

1 Introduction

The KEK B-Factory (KEKB) project [1] is in progress in order to test CP violation in the decay of B mesons. The KEKB is an asymmetric electron-positron collider comprising 3.5-GeV positron and 8-GeV electron rings. The KEKB injector linac [2] is also being upgraded in order to inject single-bunch positron and electron beams directly into the KEKB rings. The beam charges are required to be 0.64nC/bunch and 1.3nC/bunch for the positron and electron beams, respectively. High-current primary electron beams (~10nC/bunch) are required in order to generate sufficient positrons. About seventy wall-current monitors (WCMs) have been newly installed in order to reinforce the beam-monitoring system in the injector linac for the KEKB. It is important to obtain precise information concerning the amount of beam charges in order to measure the precise beam-injection rate to the KEKB rings. Calibration of the WCMs has been performed by a bench test. Bench calibration was performed using fast test pulses with a width of nanoseconds, and the calibration coefficients were derived from the pulse-height response of the monitor depending upon the pulse width. The calibration system was reported elsewhere in detail [3]. It is, however, difficult to directly measure the calibration coefficient for a single-bunch beam with a pulse width of about 10ps, because the direct generation of such short test pulses is not very easy. The author has tentatively derived calibration coefficients for a 10-ps pulse width from extrapolation based on

the results of a bench calibration. It is, however, not sufficiently accurate to estimate them by this extrapolation method, because the WCM has a strong frequency response and a beam-position dependence for shorter pulses. Such characteristics of the WCM have been investigated using the test bench in detail [4]. A new method for precise beam-charge calibration using a beam-induced field, that is, the fundamental longitudinal wakefield, was performed by beam tests [3]. The new calibration method depends not upon the pulse characteristics of the beam, but only upon the amount of beam charge. Another new method using a Faraday cup (FC) has been planned to be performed using beam tests. This is a well-known monitor used to measure the amount of absolute beam charge. The beam charge can be measured by a precise beam-charge instrumentation device after the FC perfectly absorbing them. Thus, the method using the FC is simple in principle; however, we must take care of several characterisctis of the FC before any beam experiment. The following four characteristics are important to be investigated using simulations: the first is the generation of leakage charge of the incident beam from the monitor, which is mainly caused by the development of an electromagnetic cascade shower; the second is an increment of seeming charges caused by ionizations, which is generated by interactions of residual air with the beams inside the FC; the third is that the generation of escaping charge caused by backscattered particles; the final is that the generation of secondary charge at a vacuum window of the FC. These phenomena cause error contributions for precise charge measurements; it is thus important to quantitatively estimate how much error these contributions have. The author reports some detailed analysis results using the EGS4 simulation code [5] in the following sections.

2 Faraday Cup

A cross-sectional view of the FC is shown in fig.1. It was originally designed at the Laboratoty of Nuclear Science of Tohoku University about thirty years ago. Since a detailed design report is available elsewhere [6], here, the geometry and a simple discussion about its design are briefly made. The monitor comprises a vacuum vessel made of iron, a lead block, an iron block and a carbon block with cylindrical symmetry. The monitor dimensions are about 1 m in total length to the beam axis and about 660 mm in diamter; the total weight is about 1.8 ton. More precise dimensions for each material are given in the following section. The bottom thickness of the lead block is 190 mm, which corresponds to 34 radition lengths, in order to perfectly be able to absorb incident electron beams with an energy of less than 300 MeV. The monitor can be separated by the vacuum vessel and a thin vacuum window with a thickness of 0.1 mm made of stainless steel (SUS304) from the beam line. The window thickness is required to suppress as much as possible any backscattering and multiplescattering of incident beams. The carbon block is used to suppress any rapid increase of an electromagnetic shower cascade caused by incident beams in the lead block. An opening hole with a diameter of 200 mm and a depth of 600 mm in the central region needs to suppress the escape of secondary charged particles generated by an electromagnetic shower cascade in the carbon block. The geometry of the opening hole allows maximum incident angle of the beam of 20 deg. A good vacuum condition must be maintained through a vacuum port in order to suppress the generation of ions caused in the residual air gas. The inner materials are sufficiently insulated by several beryllia porcelains from the vacuum vessel, which is connected to a ground line. The insulation resistance was measured to be larger than 1000 MW. A negative electric potential was applied on an electrode in the entrance of the monitor through a vacuum feedthrough. The electrode, here being called a secondary-electron-suppression electrode, suppresses the escape of directly backscattered charged particles and secondary electrons generated by their interactions with residual air as much as possible. Several hundred volt are typically applied to it. The beam charge is extracted from a signal port, which is connected to the lead block.

3 Monte-Carlo Simulation Using the EGS4 Code

3.1 Geometry code

Since the geometry of the FC is cylindrical, it is useful to use an example given in the reference [7], where several typical geometry codes are given in detail. The geometries used in user routines are shown in figs. 2 (a) and (b), where segmentations of the FC geometry without and with a vacuum window are shown, respectively. The dimension of length is given in unit of mm in the figures. In fig.2 (a) the FC is divided by 14 regions in total, where four materials (iron (FE), lead (PB), air gas (AIR) and carbon (C)) are assinged without the vacuum window. In fig. 2 (b) it is divided by 17 regions in total, where only the vacuum-window material is added to the segmentation (a). Several materials (iron (FE), aluminum (AL) and beryllium (BE)) are assigned for the vacuum window in order to estimate the emission rate of secondary electrons at the window. The vacuum vessel of the monitor was neglected in the simulation for simplicity; furthermore, an iron frame for the lead block was incorporated into the lead region; that is, after evaluating the equivalent lead thickness, which corresponds to an equivalent radiation length of the iron frame thickness, the equivalent lead thickness was added into the lead region.

3.2 Material data bases

Several input files for the PEGS4 code to create material data have been coded by referring to reference [8]. Fig. 3 shows two examples of input files for (a) air gas and (b) lead. A mixture of material data (oxygen, nitrogen and argon) is used for the input file of the air gas. A temerature condition of 25°C was fixed and an option "IAPRIM=1" was used; also the Sternheimer-Seltzer-Berger coefficient for a density effect was specified. The cut-off energy for both electrons and photons was fixed to be 10 keV. Single material elements were specified for other materials by adding the option "IRAYL=1".

3.3 User code

An instructive user code for a cylindrical geometry is given in lecture note [9] in detail. The user routine was modified for the FC geometry based on this note. For the transport of low-energy electrons, an option "PRESTA" [10] was specified. The same cut-off energy for photons and electrons used in the material data was defined. All of the information, energy deposition, electron, positron and photon counts generated in each material region, etc., were scored in the subroutine "AUSGUB". A flag, "DISCARD=1", in the vacuum regions outside the FC was specified in a subroutine, "HOWFAR".

3.4 Analysis

Several analyses were performed in order to determine the beam energy and the vacuum pressure in the FC experiment and to quantitatively estimate the error contributions for a beam-charge measurement. The following four subjects were analyzed by simulation based on the EGS4 code. The first was an ionization effect. The incident beam can generate ion pairs caused by electromagnetic interactions with residual air gas inside the FC. The generated ions move to a secondary-electron-suppression electrode negatively biased, and the secondary electrons move to the inner materials of the FC. Thus, the ionization effect causes a seeming increment for the beam-charge measurement, which mainly depends upon the vacuum pressure inside the monitor. The second concerns the escape of backscattered charged particles. When the beams are injected into the monitor, electromagnetic shower cascades are mainly developed at the carbon and lead regions. If the backscattered charged particles are generated from the shower cascade and escape from the monitor, the effect causes a seeming reduction of the beam charge, which mainly depends upon the

beam energy. The third is the generation of leakage charged particles outside the monitor. This effect also seemingly causes a reduction for the beam-charge measurement. The fourth concerns the thickness of the vacuum window. This means that if the injected beams generate secondary charged particles at the window, they are absorbed by the inner materials because almost all of the secondary particles have forward momentum; therefore, this effect also seemingly causes an increment for the beam-charge measurement, which strongly depends upon the thickness and material species of the vacuum window.

The ionization effect has been analyzed by simulating the energy deposition in the air-gas region upon changing the vacuum pressure. The incident electron energy was fixed to be 250 MeV in this analysis, and the FC geometry (fig. 2 (a)) was used. The generation rate of ion pairs could be estimated from a calculation of the energy deposition divided by the ionization potential of air gas, the potential energy of which is 33.38 eV/ion pair. It should be noted that this calculation gives the maximum generation of ion pairs, because in real ionization processes more complex phenomena, for example the recombination of ion pairs, occur. The vacuum pressure required for the beam experiments was chosen based on this analysis.

The generation rate of backscattered charged partcles, which means secondary charged particles backscattering in the direction of the secondary-electron-suppression electrode, was estimated by changing the incident electron energy. The vacuum pressure was fixed to be 1×10^{-6} atm in this analysis. The generation rate of the leakage charged partcles outside the monitor was also estimated simultaneously.

The thickness effect of the vacuum window for several materials (FE, AL and BE) was estimated by changing the incident beam energy. The FC geometry shown in fig. 2 (b) was used. In this analysis, for simplicity, all materials, except for the vacuum window, are replaced by a vacuum. The generation rate of secondary electrons at the window was estimated by counting the number passing through the inner material regions.

4 Analysis Results

Fig. 4 gives the result of the ionaization effect by simulating the incident electrons for 50000 cases. Since each data point gives the average value by 50000 cases; the statistical error is estimated to be about 0.4%. The vacuum pressure is required to be less than 2×10^{-4} Torr, because the generation of ion pairs of 0.1% must be required in order to perform an error contribution of around the 1% level in total for a beam experiment. It shoud be noted that all the data points are normalized to one incident electron. Figure 5 shows the anaysis result of the backscattering and escaping of electrons to the outside of the FC. The positron generation was also simulated simultaneously in this analysis; however, the generation rate was negligibly small. The incident electron energy was changed from 250 MeV to 2 GeV. The vacuum pressure was fixed to be 1×10^{-6} atm. Both the generation curves of the escaping and backscattering electrons show almost the same tendensy, and for an energy greater than about 500 MeV the curves show a plateau. The incident electron energy is required to be less than 300 MeV, taking into account an error contribution of around 0.1%. Fig. 6 shows the analysis result for the vacuum window. The generation rate of secondary electrons was estimated for three materials (FE, AL and BE) with the energy of incident electrons being 250 MeV. No clear beam energy dependence appeared within the calculation error. From the figure if a generation rate of 0.1% is required, the material must be selected to be beryllium with a thickness of 20 mm; however, taking into account easy manufacturing of the window, a thickness of 50 mm is proper. In this case, the thickness gives an error contribution of around 0.2% for the beam-charge measurement.

5 Conclusion

Several characteristics of the FC were estimated using the EGS4 simulation code. An analysis for the ionization effect gave a suitable vacuum pressure of less than 2×10^{-4} Torr inside the FC. An analysis of the backscattered and escaping charged particles required an electron beam energy of less than 300 MeV. Such two phenomena contribute a systematic errors of around 0.1% for the beam-charge measurement. An analysis of the vacuum window indicates that the best material is beryllium, with a thckness required to be less than 50 mm. This phenomenon contributes a systematic error of 0.2% for the beam-charge measurement.

Acknowledgments

The author gratefully acknowledges Dr.T.Kamitani for his help in installation and useful instruction of the EGS4 simulation code.

References

[1] S. Kurokawa, et al., *KEK Report 95-7* (1995).

[2] I. Sato, et al., *KEK Report 95-18* (1996).

[3] T. Suwada and S. Ohsawa, presented at the First Asian Particle Accelerator Conference (APAC98), KEK, Tsukuba, Japan, March 23-27, 1998; *KEK Preprint 98-15* (1998).

[4] T. Suwada, et al., *Nucl. Instr. and Meth.* **A396** (1997) 1.

[5] W. R. Nelson, H. Hirayama and D. W. O. Rogers, *SLAC Report No.265* (1985).

[6] T. Ohama, et al., *Mitsubishi Electric Advance* **43** (5) p.739 (1969).

[7] H. Hirayama, "How to Code Geometry of EGS4", *KEK Internal 97-9* (1997).

[8] Y. Namito, "How to use PEGS4", *KEK Internal 97-6* (1997).

[9] H. Hirayama, "How to Write the User Code of EGS4", *KEK Internal 97-8* (1997).

[10] Y. Namito, et al., "Installation of EGS4", *KEK Internal 97-7* (1997).

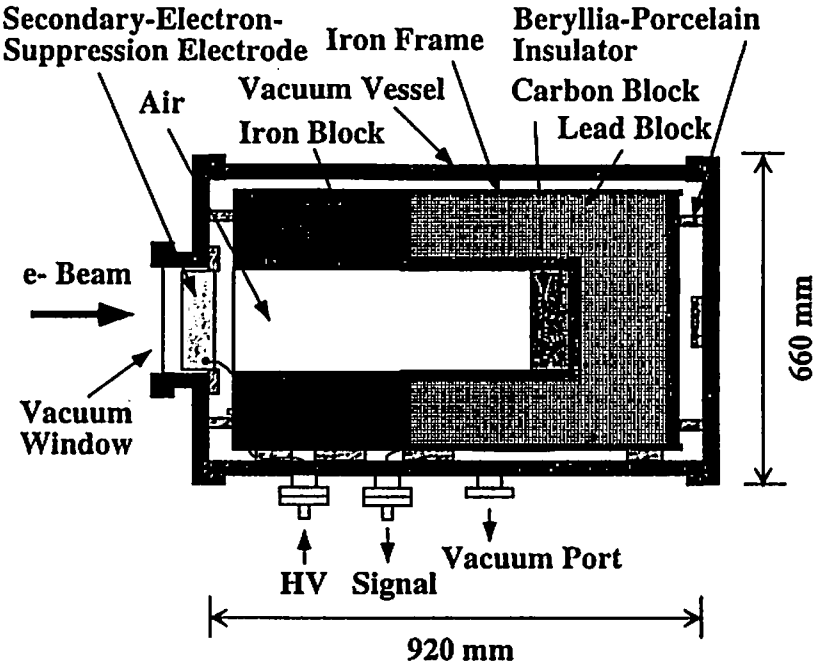

Fig.1. Cross-sectional view of the Faraday cup.

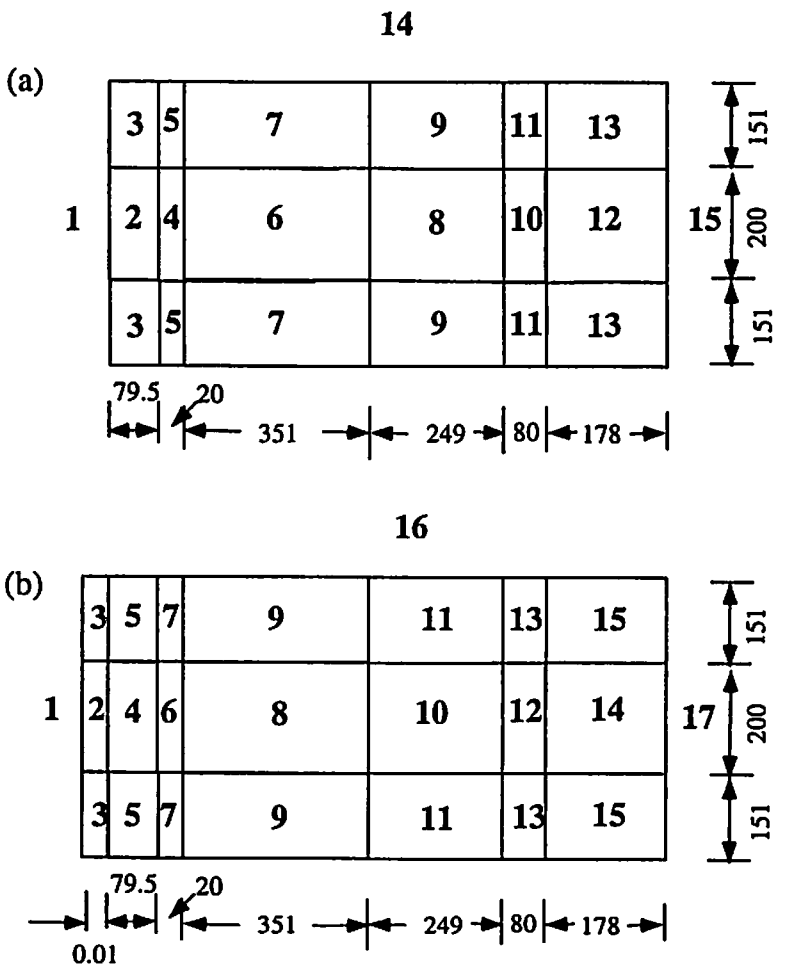

Fig.2. Cylinder slab geometries for the FC (a) without a vacuum window and (b) with it. The dimension of length is given in unit of mm. The bold letters indicate the region number and for each region one material is assigned. The assigned material species are as follows: (a) Vacuum(1, 3, 14, 15), FE(7), PB(9, 11, 12, 13), C(10), AIR(2, 4, 5, 6, 8) and (b) the vacuum window(2) is added to the geometry (a) and all the other regions are replaced with vacuum.

(a)

```
MIXT
 &INP NE=3,RHO=1.2929E-3,GASP=0.9161,RHOZ=0.75575,0.23143,0.01282,
 IAPRIM=1 &END
AIR-FARADAY              AIR-GAS
N O AR
ENER
 &INP AE=0.521,UE=2000.511,AP=.01,UP=2000.0 &END
TEST
 &INP &END
PWLF
 &INP &END
DECK
 &INP &END
```

(b)

```
ELEM
 &INP IAPRIM=1,IRAYL=1 &END
PB-FARADAY               PB
PB
ENER
 &INP AE=0.521,UE=2000.511,AP=.01,UP=2000.0 &END
TEST
 &INP &END
PWLF
 &INP &END
DECK
 &INP &END
```

Fig.3. Typical two examples of input files for PEGS code used to create material data which show (a) air gas (25°C, 1atm) and (b) lead. The cut-off energy for both electron and photon was fixed to be 10 keV and the upper limit of the kinetic energy for both electron and photon is used to be 2 GeV in these examples.

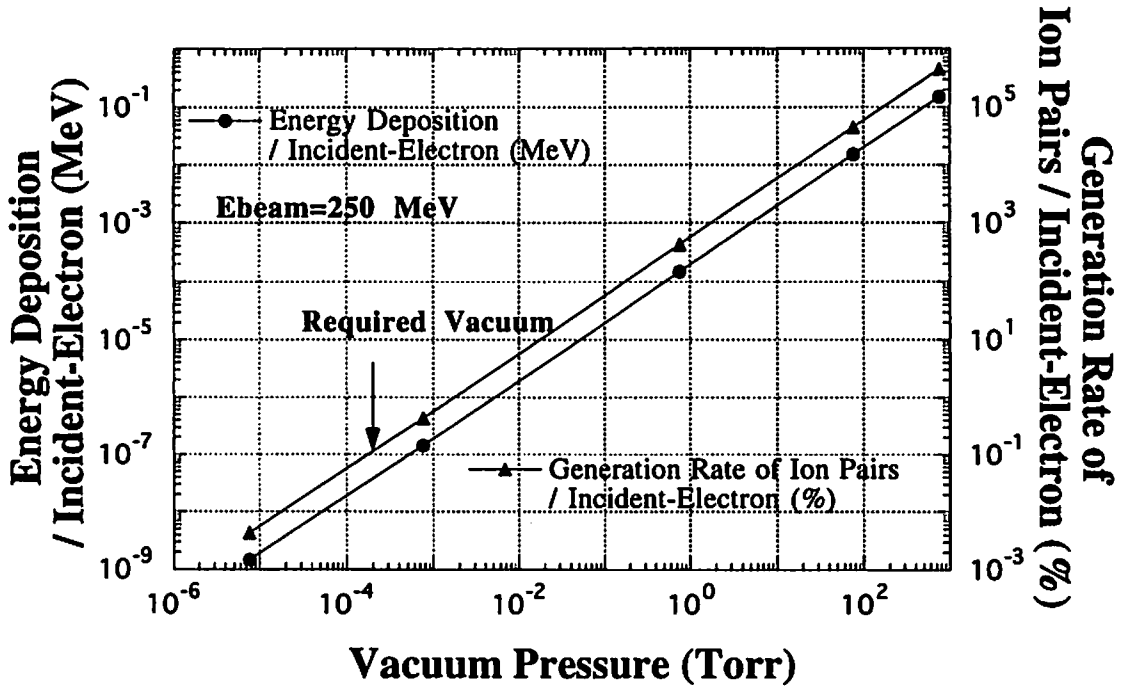

Fig.4. Variations of the generation rate of ion pairs/incident-electron (%) and the energy deposition/incident-electron (%) depending upon the vacuum pressure in the FC.

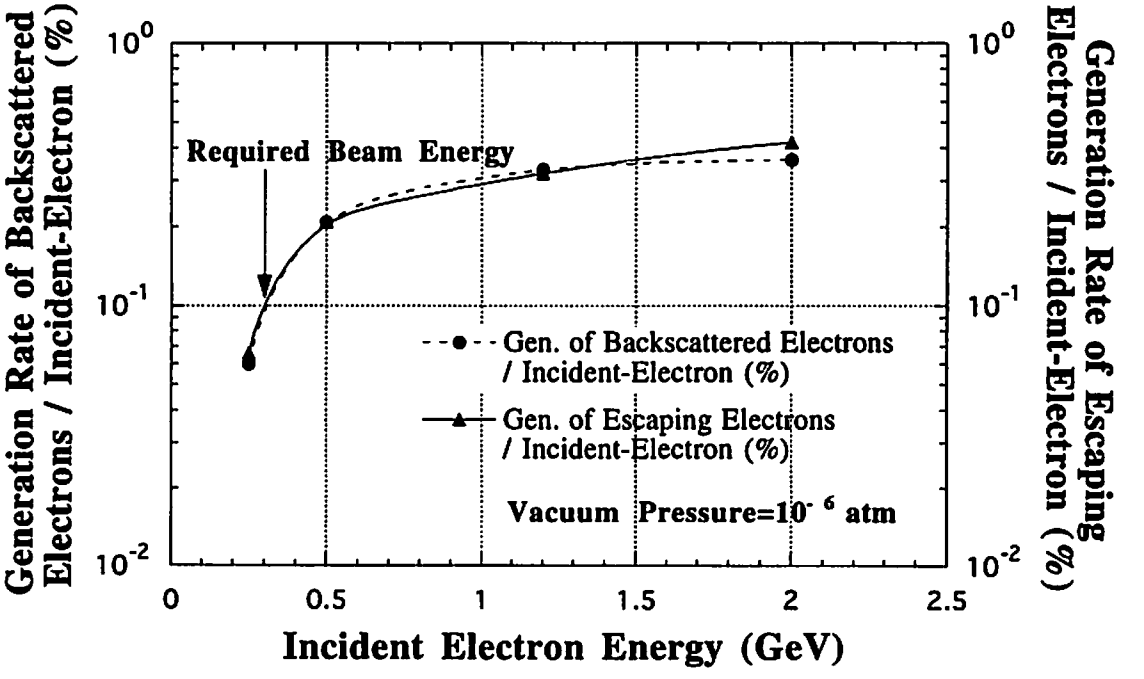

Fig.5. Variations of the generation rate of the backscattering and escaping electrons/incident electron (%) depending upon the incident electron energy.

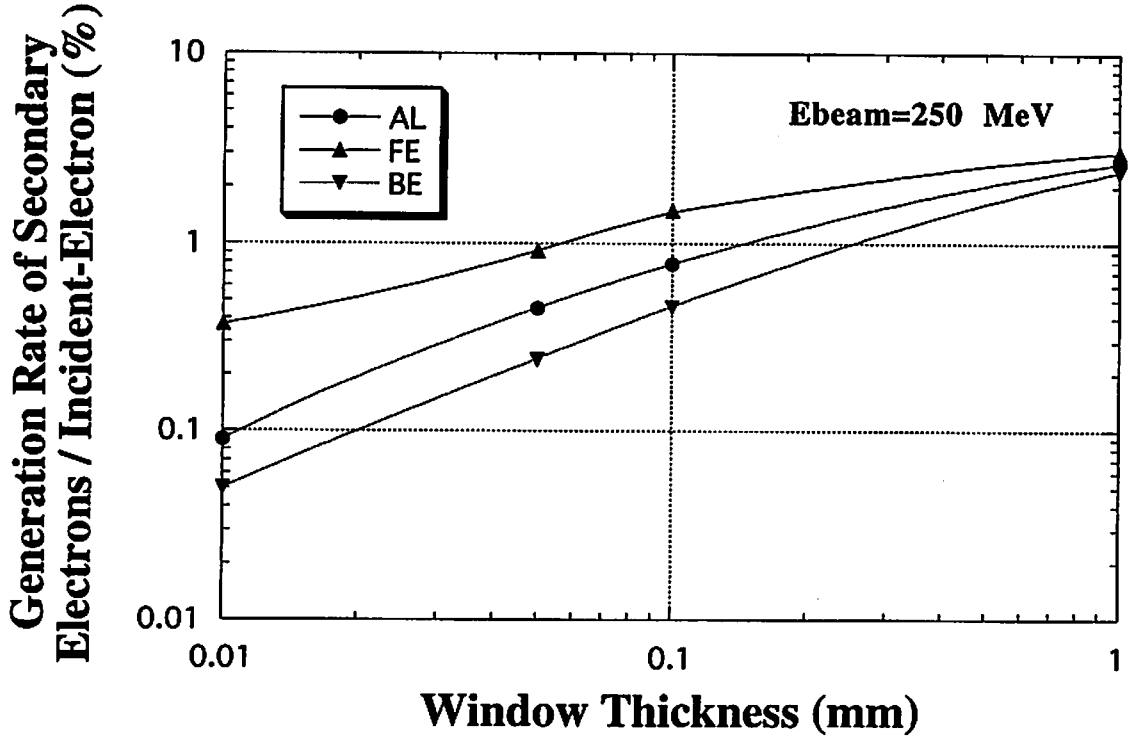

Fig.6. Variations of the generation rate of secondary electrons/incident-electron (%) depending upon the thickness of the vacuum window. The incident-electron energy was fixed to be 250 MeV.

SIMULATION OF GAUGE STATURE USED RADIOISOTOPE BY EGS4 CODE

Eiko KINOSHITA

ARTHNIX Corporation
3, Nakasakurazuka, Toyonaka-shi, Osaka 560-0881, Japan

1 Introduction

We make and sell gauge statures used radioisotope of γ-ray as Cs-137, Co-60, Ba-133 and so on. EGS4 code were introduced to have a new appreciation about its deign, to develop new statures, and to examination some problems. General Build up factors have been calculated, but it doesn't reproduce in different geometries, therefore to calculate Monte Carlo simulation by EGS4 code is very useful. I would introduce how use EGS4 code for.

2 Simulation of the Source Case

The source case of Cs-137 is made with lead for shelter. It was designed empirically, and it maybe collimates the source and has an effect on attenuation of photons. Its geometry for simulation is shown fig.1. Source is as point source, monochrome energy(0.662MeV), and incidence for 4π. Photons that reached the last plane were counted. Three dimensional graph in fig.2 is express to distribution of photons at the plane. 80% of these photons were within a radius of 15mm. The result of energy spectrum in fig.3 shows there are about 70% count of main peak. These appearance were not seen by our PHA, because of effect inside NaI scintillator. From the above, I realize that energy of γ-ray through the source case is not monochrome, and it have an effect on attenuation of photons.

3 Simulation of the Pipe Densimeter

Our "GD-2000" is to measure the density of an object inside pipe from outside, it consists of the part of a source and the part of a detector. The principle of the "GD-2000" observes that attenuation of photons are exponential. The counting rate of photons N is given by

$$N = N_0 \cdot \exp(-\kappa \cdot \rho) \tag{1}$$

ρ: density

N_0: counting rate at ρ=0

κ: constant number

The source of "GD-2000" has very low intensity(lower than 3.7MBq), and its penetrating photons are very low number, then efficiency of "GD-2000" attends statistical error. The error of a density is given by

$$\frac{\Delta N}{\Delta \rho} = N_0 \exp(-\kappa \cdot \rho) \times (-\kappa) \tag{2}$$

$$\Delta N = N \times (-\kappa) \Delta \rho \tag{3}$$

The statistical error of N defines $\sqrt{N}$, error of$\Delta\rho$ is given by

$$\Delta \rho = \frac{-\sqrt{N}}{N \cdot \kappa} = \frac{1}{\sqrt{N}\kappa} \tag{4}$$

Constant number of κ is decided by geometry, and N is the function of κ, so $\Delta\rho$ is decided by geometry. It is one of the purpose that we will find the best geometry with 3.7MBq source by EGS4 code. At first simulation of the pipe densimeter, the part of a source is only monochrome energy and divergent beam limited acute angle, but the result of a simulation didn't agree with the experiment completely. The result of the simulation of the source case are

1. the source is not monochrome energy (0.662Mev:100%, 0-0.662MeV:71%)

2. the source is collimated any angle.

By reference to those result, the simulation of the pipe densimeter reproduced the experiment approximately. In fig.4, experimented and simulated data κ divided by a inside diameter of the pipe is shown. The number of times of calculate is a few, but qualitative trend is reproduced experimented data. In future, I would simulate about Ba-133, Co-60, and about a big diameter pipe difficulty execution moreover.

4 Simulation of the Insertion Typr Densimeter

We make insertion type densimeter on probation. It measures a density by inserting in a measurement object. It observe the same principle of "GD-2000", but the part of the source and the part of the detector is unity. Its appearance is shown in fig.5, it has Ba-133(main energy is 0.566MeV) source. Experimental data at 0.0, 1.0, 1.5g/cm^3 are shown in fig.6. It has a maximum at about 1.0g/cm3, this trend may be consequence that attenuation by the measurement object between the source and the detector competes with increment of scattering in. The result of the simulation shows same trend. Its spectrum is shown in fig.7. When ρ=0.0g/cm^3, almost photons are in main peak of Ba-133, because there is not object to scatter. As the density increases, many photons make peak at about 0.1MeV. These are scattered photons of course, therefore the plotted data in fig.8 that under 0.15MeV photons are cut shows linear dependence on density. By reference to those result, experimental data with the detector added a filter to cut under 1.5MeV have useful linearity as densimeter.It is shown in fig.9.

5 Conclusion

At first, to introduce a simulation by EGS4 code is only substitution an experiment, but its result had information that we didn't obtain from experiment. Especially, we don't obtain energy distribution of photons after going through the object from our measurement system. I recognized the simulation is one of the best way to gain an essence, because it can adds and removes some conditions easily. In addition, a picture of shower written by EGS4PICT is very useful when we explain the principle of our densimeter to user who don't be familiar with radiation.

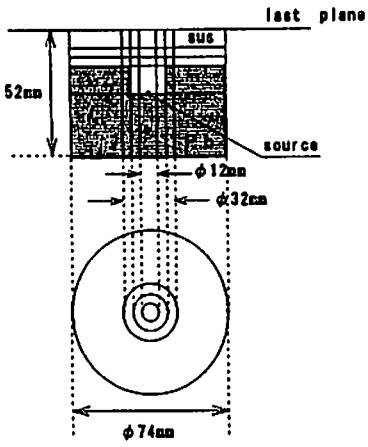

fig.1 The source case

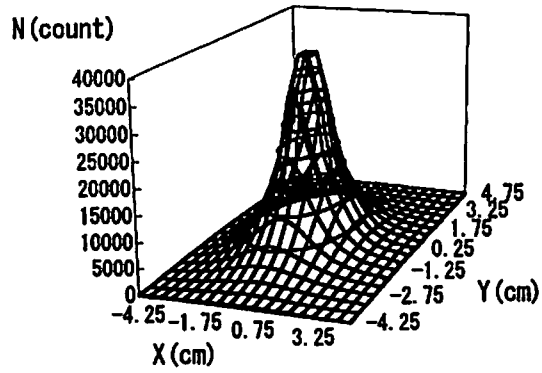

fig.2 THE SIMULATION OF THE SOURCE CASE
Distribution of photons at last plane

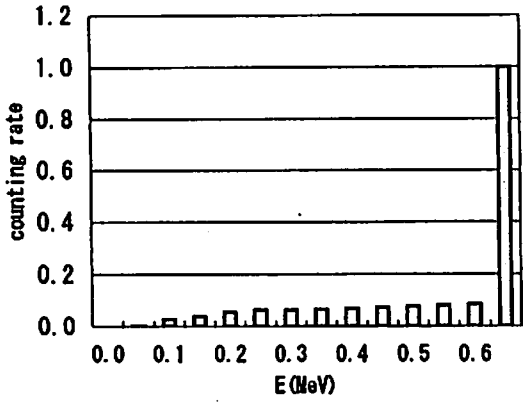

fig.3 THE SIMULATION OF THE SOURCR CASE
Spectrum of photons at last plane

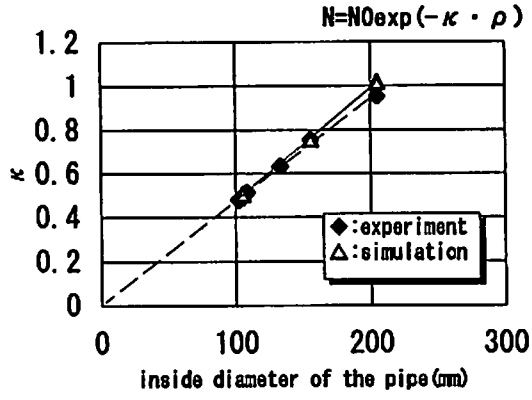

fig.4 THE SIMULATION OF THE PIPE DENSIMETER

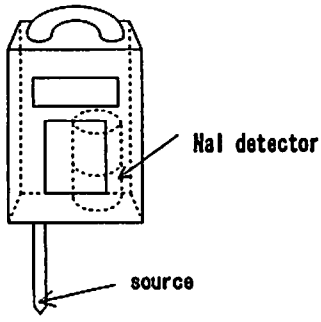

fig.5 The insertion type densimeter

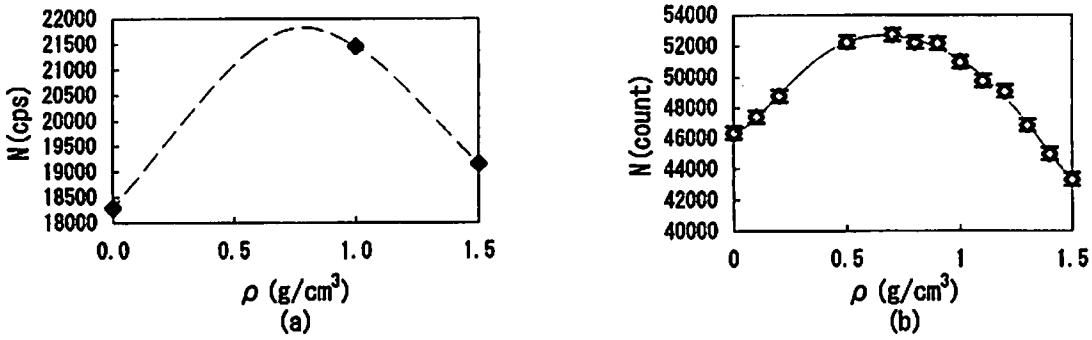

fig.6 THE SIMULATION OF THE INSERTION TYPE DENSIMETER
(a) experimental (b) EGS4

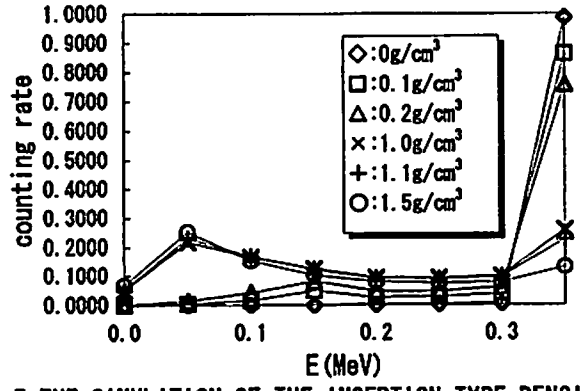

fig.7 THE SIMULATION OF THE INSERTION TYPE DENSIMETER
Spectrum of photons at detector

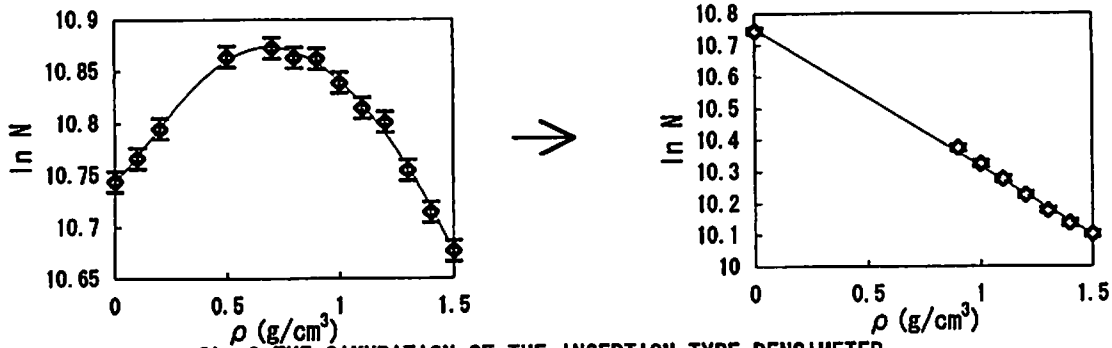

fig.8 THE SIMURATION OF THE INSERTION TYPE DENSIMETER

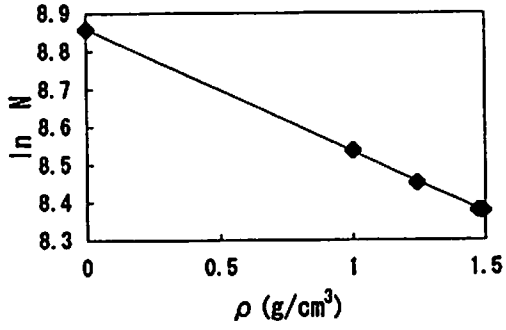

fig.9 The insertion type densimeter
ρ dependence of N with a detector added filter

STUDY OF RESPONSE FUNCTION MEASURED BY A GE DETECTOR TO A LASER COMPTON-BACKSCATTERED PHOTON BEAM COMPARED WITH CALCULATION BY EGS4/PRESTA CODE TAKING ACCOUNT OF THE SOURCE SIZE

K. KUDO, N. TAKEDA, H. OHGAKI, H. TOYOKAWA, and T. SUGITA[1]

Quantum Radiation Division, Electrotechnical Laboratory
1-1-4 Umezono, Tsukuba-shi, Ibaraki 305-8568, Japan
kkudo@etl.go.jp and ntakeda@etl.go.jp

[1]*Science System Laboratory*
1342-6 Sumiyoshi, Tomobe-cho, Ibaraki 309-17, Japan

Abstract

A laser Compton-backscattered (LCS) photon beam, which has a quasi-monoenergetic distribution in the energy range up to 20 MeV, can be used for the calibration purpose of γ-ray detectors.

In order to determine the fluence of a LCS photon beam by using a coaxial type Ge detector, the EGS4/PRESTA Monte Carlo code has been used to calculate response functions, total and full-energy peak efficiencies. An uniform rectangular parallelepiped source model used before in the EGS4 code has been replaced by the model which has a more realistic model expressed by a x-direction or y-direction gaussian distribution on the cross section perpendicular to the electron beam. The calculation was performed under the beam condition incident on the different position on the detector, vertically and horizontally. The results suggested that the pulse height spectra calculated by the EGS4/PRESTA code agreed very well with the measured spectra, if the LCS beam was incident at the center of the cylindrical Ge detector vertically and at the $\pm$2.02 cm position from the cylindrical axis of a Ge crystal horizontally. The full-energy peak efficiency became larger in these cases.

These beam conditions would be used as a reference irradiation condition to measure the photon fluence precisely. A further measurement and a improvement of the calculation for the LCS photon beam would be continued at other energies to establish a photon calibration field at high energy region.

1 Introduction

A Laser Compton-scattered (LCS) photon beam is expected to be a high energy photon source for the calibration of γ-ray detectors in the energy range from 2 MeV to 20 MeV. The Electrotechnical Laboratory has developed a source of polarized photons as shown in Fig. 1[1]. The high energy photon beam is produced by the interaction of a second harmonic light of Yttrium Lithium Fluoride (YLF) laser (wavelength 527nm, minimum pulse width 150 ns and pulse reputation rate

2 -50 kHz) with relativistic electrons (energy 300-800 MeV, maximum beam current 300mA, pulse reputation rate 166 MHz) in the storage ring of TERAS. The photon produced in the straight section of 180 cm in length have a continuous energy distribution corresponding to the emission angle with the maximum energy at zero degree to the electron beam direction. After passing through a lead collimator of 20 cm in length with a re-entrant hole of 0.2 cm in diameter located on the electron beam axis, the collimated photon beam has a quasi-monoenergetic distribution with the energy interval defined by the collimator hole size and the electron energy. If the hole size of a lead collimator is selected to be smaller, the monocromaticity becomes better naturally. However the beam intensity becomes weaker and narrower for the detector calibration purpose.

To obtain the better understanding of physical properties on the LCS photon beam, we performed several experiments measured by a relatively larger cylindrical Ge detector (GEM-120225-P manufactured by EG&G ORTEC). First, we quantitatively estimated the peak pile-up rate of two pulses and three pulses by assuming a Poisson time distribution for the pulsed photon beam incident on the Ge detector and corrected counting losses up to 20% under the current setup[2]. Second, we found that the pulse height distribution of a Ge detector to the LCS photon beam changes greatly depending on the photon incident position because the narrow beam interacts with the inside material of Ge crystal, aluminum housing or the central cavity along the track. Naturally, the secondary electrons produced thorough the detection of photons in the detector also suffer the wall and the boundary effect simultaneously. For example, the on-axis incidence on a cylindrical Ge detector causes the decrease of the total and full-energy peak efficiencies due to the central anode cavity. In order to study the response function of a Ge detector, the EGS4/PRESTA-CG Monte Carlo code[3,4] was used under the different conditions such as different beam directions incident on the detector parallel to the axis of the Ge cylinder, or vertical to the axis. However, the calculated response function did not agree with the pulse height distribution measured at the photon maximum energy of 5.969 MeV.

In this paper, we present the response functions, total and full-energy peak efficiencies of the Ge detector calculated by the EGS4/PRESTA-CG Monte Carlo code using a precise source model of photons, which takes into accounts the x and y space-dependent Gaussian distribution with an arbitrary parameter of FWHM in space spread. The calculated response functions would be compared with the pulse height spectra measured by the Ge detector at the maximum energy of 5.969 MeV.

2 Monte Carlo Simulations with the EGS4/PRESTA Code

The EGS4 (Electron Gamma Shower Version 4) is a general code for the Monte Carlo simulation of the coupled transport of photons, electrons and positrons in three dimensional geometry for energies above 10 keV for electrons and positrons and above 1 keV for photons up to several TeV. The PRESTA (Parameter Reduced Electron-Step Transport Algorithm) routine was developed to minimize the dependence of the results on the step length in the electron transport simulation[5]. We therefore adopted the EGS4/PRESTA code combined with the Combinational Geometry (CG)[4] to calculate the energy distribution of high energy photons at the entrance of the Ge detector and the energy distribution deposited in the Ge crystal which is assumed to be equal to a pulse height spectrum.

The geometry routine were written according to the facility layout shown in Fig.1 by taking into account a detail configuration of the whole system, which consisted of a photon volume source, a lead collimator, a coaxial Ge detector and air in the surroundings. At the beginning of the calculation , the photon volume source was assumed to be a rectangular parallelepiped of the size of (x cm) x (y cm) x (180 cm) having a uniform photon source distribution in the volume. However, the actual photon intensity on the vertical cross section was not uniform and hence we adopted a Gaussian space distribution as a simulation model for the x-direction and y-direction vertical

to the electron beam direction, independently. The beam size of x- and y-direction in the EGS4 calculation were determined by changing the FWHM of a Gaussian distribution.

The backscattered photon energy and the corresponding emission angle to the backward direction were randomly generated by following a kinematic formula for the Compton scattering, as the input data for the EGS4/PRESTA calculation. The effects of electron beam divergence and the energy spread were not considered in this report, although these effects can be calculated in this program. In order to shorten the computing time, the maximum solid angle cone to the backward emission was limited to be a little larger than the re-entrant hole of the lead collimator, which was positioned at 503.6 cm apart from the center of the volume source. The coaxial type Ge detector was positioned at 830.9 cm from the center of the source. The geometry of the Ge detector used in the EGS4 calculation was assumed to be composed of multi-layer cylinders of Ge, aluminum and cavity vacuum with a anode contact pin according to the factory information.

3 Results and Discussion

The photon energy distributions at the entrance of the Ge detector calculated by the EGS4/ PRESTA code assuming the different size of a source cross section are shown in Fig.2 at the maximum photon energy of 5.969 MeV. The quasi-monoenergetic photon peak produced by the lead collimator has an unsymmetric shape with the full energy spread of 1.5 MeV between the well-defined maximum and minimum energy edges and a steeply decreasing slope from the upper edge to the lower edge. The FWHM (Full Width at Half Maximum) and the FW(1/10)M (Full Width at 1/10 Maximum) for the lead collimator of 0.2 cm in diameter were 3.5% and 11.2%, respectively.

Fig. 3-(a), 3-(b) and 3-(c) (from the top figure to the bottom one) show the computational pulse height spectrum best-fitted with the experimental one. In order to obtain the best fitted spectrum, Both the FWHM parameters of each Gaussian distribution of x and y direction on the cross section perpendicular to the electron beam were changed independently as the input data of the EGS4 calculation and the result was fitted to the measured spectrum. The best fitted spectrum was selected by using a χ-square testing. The collimated beam was incident on the Ge detector vertically at 0 cm (from the vertical center of a cylindrical Ge crystal), -4.1 cm and +4.5 cm, respectively. The channel unit on the energy axis equals to 10 keV. The peak and total efficiencies calculated by the EGS4 code are also shown ranging from 1.6% to 8.7% and from 81.6% to 82.1%, respectively. From the upper energy region to the lower energy direction on the spectra, the full energy peak at 596.9 ch., a single escape peak of annihilation photons at 545.8ch. and a double escape peak at 494.7 ch. can be seen in the figure. The Compton edge can be seen slightly between the full energy peak and the single escape peak. In the lower energy region, 0.51 MeV and 1.02 MeV peaks produced by the detection of annihilation photons could be seen especially in the cases of (a) and (b), because the contact pin in the anode cavity became a source of annihilation photons. In the case of 3-(a), the fairly good agreement between the calculation and the experiment could be obtained on the whole pulse height region. However, the beam was incident on the edge part of the Ge crystal, some discrepancy was seen at the full energy peak region. In this case, the full energy peak area decreased to 4.2% and the single- and double-escape peaks became dominant parts of the pulse height spectrum.

Fig.4-(a), 4-(b) and 4-(c) (from the top to the bottom) also show the calculated pulse height spectra compared with the experimental data in the case of horizontal beam incidence on the detector at three different points of +2.02 cm (from the axis of a cylindrical Ge crystal), 0 cm (center) and +3.60 cm, respectively. If the collimated beam was incident on the middle point (+2.02cm) between the center and the outer surface of the Ge detector, the calculated spectrum agreed very well with the experimental one.

On the other hand, If the collimated beam was incident on the axis of cylindrical Ge crystal,

the full energy peak efficiency naturally decreased down to 1.6% compared with the efficiency of 8.7% in the case of 2.02 cm incidence because of the existence of an anode cavity with a contact pin. The calculated pulse height spectrum agreed well in the higher pulse height region, however, the spectrum was underestimated in the middle energy region. The disagreement can be also seen when the collimated beam was incident on the edge part at 3.60 cm from the central axis of Ge crystal.

The full-energy peak efficiency shows a remarkable increase, if the traversing track of the incident photon and secondary electrons are located inside the sensitive region and far from the detector boundary and the anode cavity.

4 Conclusion

In order to determine the fluence of a LCS photon beam by using a coaxial type Ge detector, the EGS4/PRESTA Monte Carlo code has been used to calculate response functions, total and full-energy peak efficiencies taking into accounts the practical source model under the beam condition incident on the different position on the detector, vertically and horizontally. The results suggested that the pulse height spectra calculated by the EGS4/PRESTA code agreed very well with the measured spectra, if the LCS beam was incident at the center of the cylindrical Ge detector vertically and at the +2.02 cm position from the cylindrical axis of a Ge crystal horizontally. The full energy peak efficiency became larger in these cases. The fluence of the LCS photon beam would be determined by the reference measurement described above.

A further measurement and a improvement of the calculation for the LCS photon beam would be continued to establish a photon calibration field at high energy region.

References

[1] H. Ohgaki, S.Sugiyama, T. Yamazaki, T. Mikado, M. Chiwaki, K. Yamada, R. Suzuki, T. Noguchi and T. Tomimasu, *IEEE Trans. Nucl. Sci.*, **38** (1991) 386.

[2] K. Kudo, N. Takeda, A. Fukuda, T. Noguchi, H. Ohgaki and T. Yamazaki and T. Sugita, Proceedings of the Fourth EGS4 Users' Meeting in Japan, *KEK Proceedings 96-10*, 47 (1996).

[3] W.R. Nelson, H.Hirayama and W. O. Roger, *SLAC-Report-265* (1985).

[4] T. Sugita, T. Torii and H. Ando, Proceedings of the Fourth EGS4 Users' Meeting in Japan, *KEK Proceedings 94-8*, 9 (1994).

[5] A.F. Bielajew and D. W. O. Rogers, *Nucl. Instr. and Meth.*, **B18** (1987) 165.

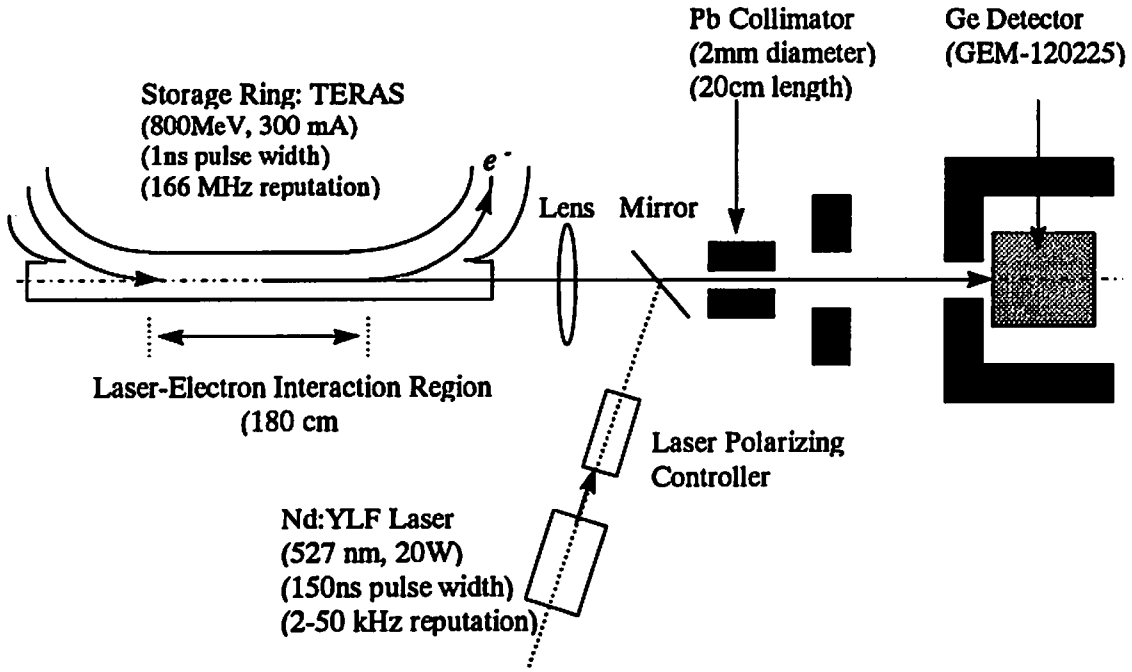

Fig. 1 Layout of the facility of laser-induced compton backscattered photons

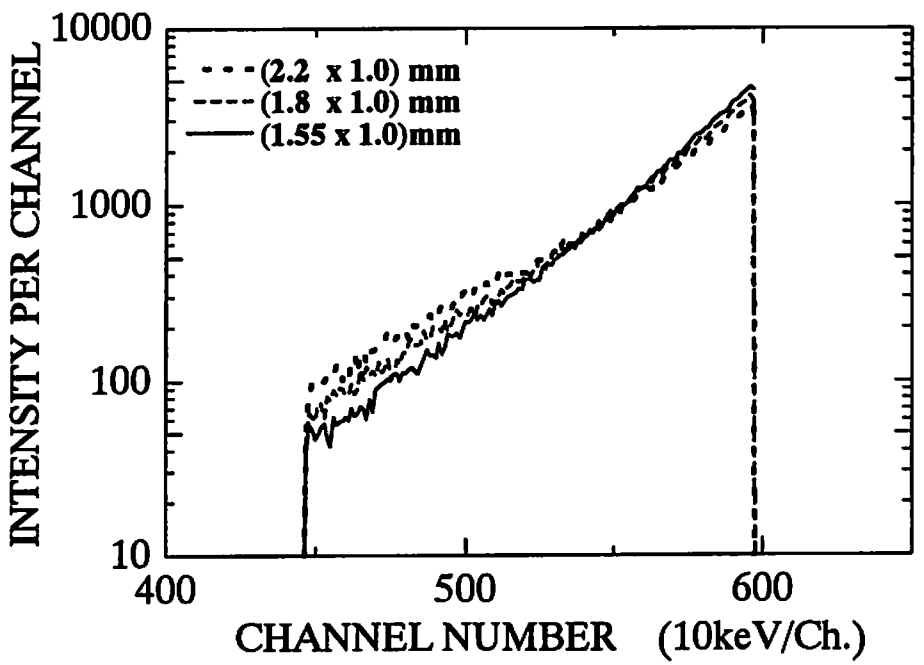

Fig. 2 Photon energy spectrum at the entrance of a Ge detector at the maximum energy of 5.969 MeV with different source size of x-y cross section

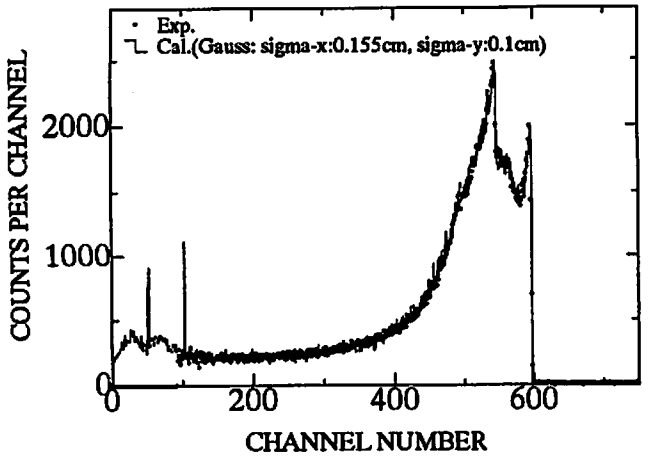

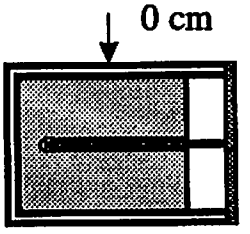

Peak effciency = 7.1%
Total efficiency=74.4%

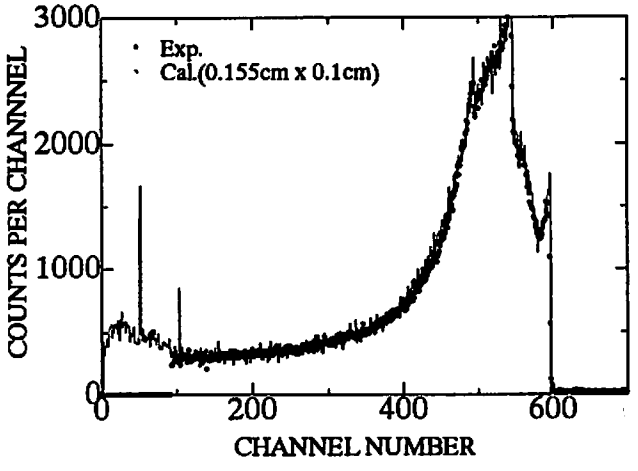

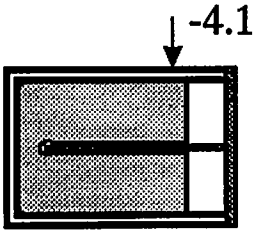

Peak effciency = 4.4%
Total efficiency=74.0%

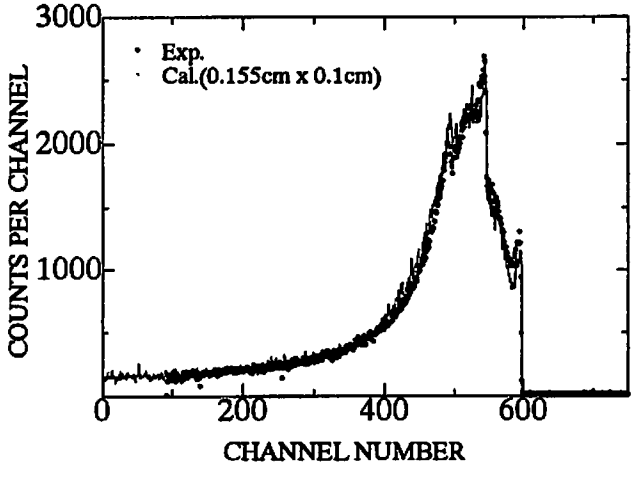

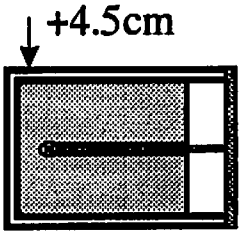

Peak effciency = 4.2%
Total efficiency=74.7%

Fig.3 Comparison of a calculated pulse height spectrum with an experimental one at 5.959 MeV to the collimated beam incident on the Ge detector at three different points, vertically.

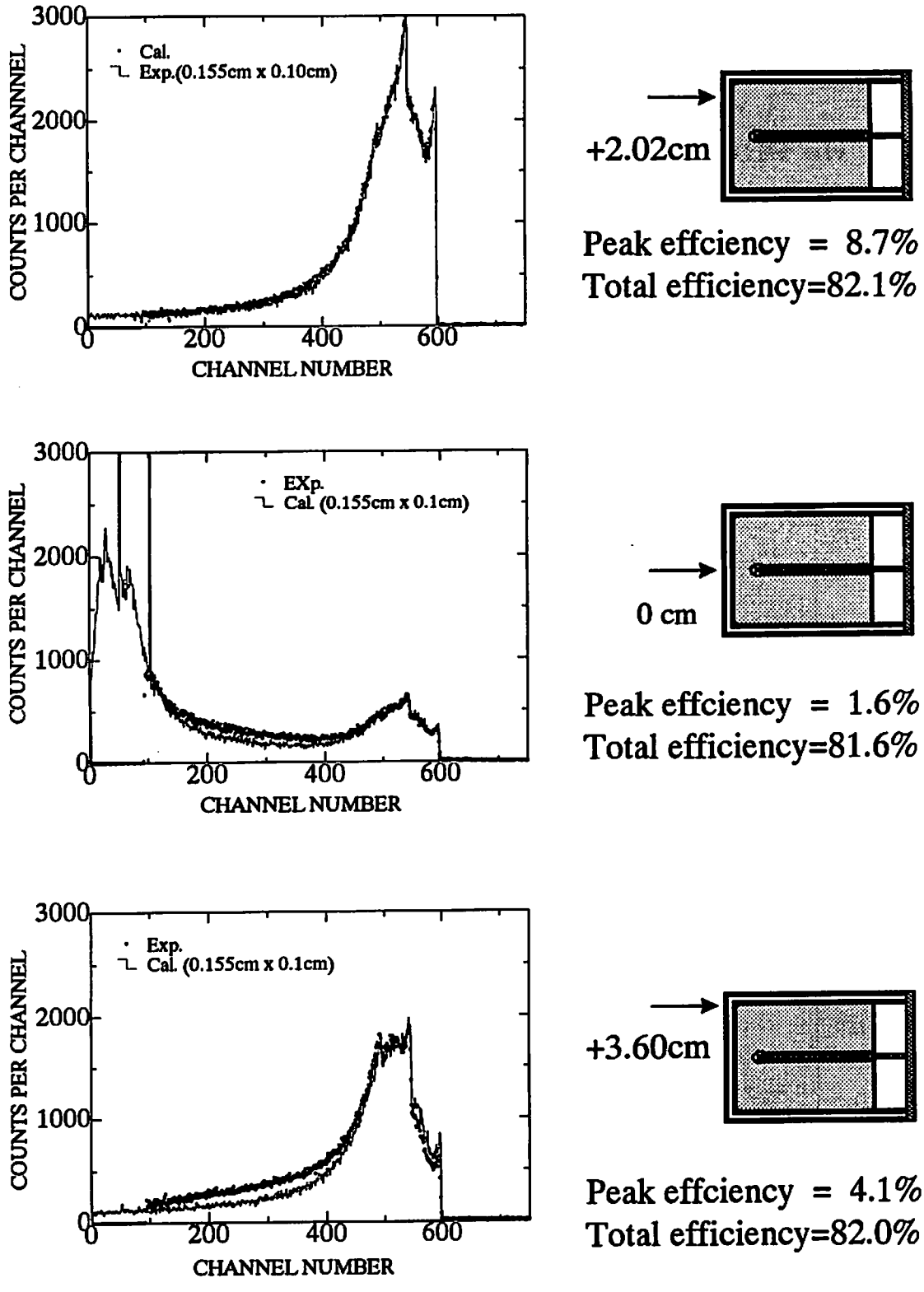

Fig.4 Comparison of a calculated pulse height spectrum with an experimental one at 5.959 MeV to the collimated beam incident on the Ge detector at three different points, horizontally.

EVALUATION OF γ-RAY RESPONSE OF ^{3}He PROPORTIONAL COUNTER BY USING EGS4

N. TAKEDA, K. KUDO, H. HASHIMOTO*[1], Y. KAWADA*, T. SUGITA**, H. HIRAYAMA***, Y. NAMITO*** and S. BAN***

Electrotechnical Laboratory
1-1-4 Umezono, Tsukuba, Ibaraki 305-8568, Japan

**Seikei University*
3-3-1 Kichijoji-Kitamachi, Musasino-shi Tokyo 180, Japan

***Science System Laboratory*
1342-6 Sumiyoshi, Tomobe-cho, Nishiibaraki-Gun, Ibaraki 309-17, Japan

****High Energy Accelerator Research Organization*
1-1 Oho, Tsukuba-shi, Ibaraki 305-0801 Japan

Abstract

The γ-ray response function of the 3He proportional counter for energy range from 20keV to 1.333MeV were calculated by the EGS4. The calculated results showed good agreements with measured pulse height distributions. The estimated γ-ray detection efficiency of the counter by the EGS4 also showed good agreements with measurements.

1 Introduction

It is often required in neutron calibration purposes to determine the contribution of γ-rays produced in a neutron source and in the surroundings, because some types of neutron detectors are sensitive both to neutrons and to γ-rays. The pulse signal produced in the process of a neutron detection must be discriminated against γ-ray signals in a neutron detector. In an experiment of a ^{124}Sb-Be photoneutron source, very intense γ-rays of 10^5 emitted from ^{124}Sb interact to produce only 2.1 neutrons[1] and hence the small amount of neutrons appear in much more intense γ-ray background. In this case, the intense γ-ray signals cause a distortion of pulse height spectrum due to pulse pileup such as resolution degradation and summed pulse height distribution. Therefore, it is important for the precision neutron measurements that the γ-ray response of a neutron detector will be estimated precisely.

In this study, the γ-ray response function of a ^{3}He proportional counter would be calculated by the EGS4 (Electron Gamma Shower Version 4) Monte Carlo code[2]. The calculated results would be compared to measured ones in order to verify the availability of the EGS4 code for evaluation of γ-ray response of neutron detectors.

[1]Present affiliation is Oki Electric Industry Co., Ltd.

2 Measurement of γ-ray Response

The response function of a commercially available 3He proportional counter (Reuter-Stokes RS-P4-0806) was measured. The counter has 25.4mm in diameter and 204.05mm long. A filled gas is a mixture of ^{3}He (400kPa) + Ar (200kPa) and a 1% partial pressure of CO_2 as a quench gas. A wall material of the counter is 304 stainless steel and a ratio of its constituent elements is Ni:Cr:Fe=0.08:0.18:0.74. The wall thickness estimated at 0.45mm.

Three radioisotope γ-ray sources and a monoenergetic x-ray field of KEK were used for the measurement of response. The activities of radioisotope sources were calibrated by Amersham Buchler GmbH & Co KG (as energy calibration standards), and their activities at an experimental time were calculated as shown in Table 1 taking into account their half lives.

Table 1. γ-Ray Sources Used for the Measurement of Response

Source	γ-ray energy [keV]	Activity [kBq]	Error of Activity
^{60}Co	1173 (100%)	15.9	±4%
	1333 (100%)		
^{137}Cs	662 (90%)	35.0	±5%
^{241}Am	26.3 (2.4%)	41.8	±5%
	59.5 (36%)		

A layout of the measurement is shown in Fig. 1. In the calibration by using radioisotope γ-ray sources, the sources were located vertically to the axis of anode wire at the distance of 5.5 cm apart from the center of anode wire. The γ-ray was irradiated to all parts of the counter. In the case of monoenergetic x-ray field, the x-ray was collimated in the diameter of 0.3mm, and irradiated center of the counter perpendicular to anode wire.

3 Calculation of Response Function by EGS4

The response functions have been calculated with the EGS4 Monte Carlo code. The calculations were performed under the following conditions;

1. The radioisotope γ-ray sources were assumed to be an isotropic point source. The monoenergetic x-ray were assumed to be a collimated beam which has 0.3mm diameter. A linear polarization effect was taken account of the monoenergetic x-ray property.

2. The outer size of the counter was assumed to be 25.4mm in diameter and 204.05mm long, and an anode connector was ignored. The detail inner structure of the counter were not informed by the manufacturer, then it was assumed that the counter wall thickness was 0.45mm, the anode wire diameter was 30 μm and the field tube diameter was 1mm, as shown in Fig. 1.

3. The materials of the counter wall, the anode wire and the field tube were assumed to be 304 stainless steel.

4. The small amount of quench gas of CO_2 was ignored and the mixture of ^{3}He (400kPa) + Ar (200kPa) gas was taken into account.

5. An edge effect of the counter[3] was taking into the calculation. The counter was divided into several regions by some perpendicular planes to the anode axis. Measured gas multiplication factors (as shown in Fig. 2) were adopted for these regions. In the calculation, it was multiplied the multiplication factors by an energy deposition of electrons in gas regions.

6. The calculation options of EGS4 such as Rayleigh scattering, incoherent scattering and Compton profile, were taken consideration at all regions.

4 Results and Discussion

4.1 Pulse height distribution

The comparison of the calculated pulse height distributions with measured data obtained using three γ-ray sources are shown in Fig. 3. In the pulse height distributions for γ-rays emitted from ^{60}Co and ^{137}Cs, continuous spectra were observed gradually decreasing with the increase of energy as shown in Fig. 3, however, a photoelectron peak or a Compton edge were not observed. It is concluded that the energetic electrons produced mainly in the counter wall have ranges longer than the directional chord length of the gas region and they lose their energy partially in the gas region. Therefore, in the case of ^{60}Co and ^{137}Cs, the photoelectron peak and the Compton edge were not observed. On the other hand, in the pulse height distribution obtained in the measurement of low energy photons from the ^{241}Am source, the energy of electrons produced by γ-ray interactions is very low and hence the photoelectron peak and the Compton edge appeared clearly. All simulated results for radioisotope γ-ray sources showed good agreement with experiments.

The comparison of the calculated pulse height distributions with measured data using monoenergetic x-rays at 20keV (upper figure) and at 40keV (bottom figure) are shown in Fig. 4. In the monoenergetic x-ray field, there are some higher harmonics of fundamental energy. Then some peaks were observed in the same pulse height distributions. In these cases, some Compton edges had different features between the calculated and the measured data. The difference of these parts could not be explained by the effects of the polarization of x-ray beam or Compton profile as shown in Fig. 5 and Fig. 6. The more precise calculation model would be expected to obtain the better agreement between the calculation and the experiment by taking account of the precise configuration of the experimental setup such as a X0rat fluence monitor and setting devices between the counter and the x-ray collimator.

4.2 γ-ray source activity measurement

The response function of the ^{3}He counter at the fixed position was calculated by the EGS4 code under the condition of the isotropic point source. The activities of each source were determined by fitting the simulated response functions to the experimental data. The comparison of the source activities derived from the simulation to the reference values provided by the manufacturer is listed in Table 2. The measured γ-ray activities also showed good agreements with the reference activities.

Table 2. Comparison of Reference and Measured Activities.

Source	Reference Activity [kBq]	Measured Activity [kBq]
^{60}Co	15.9±0.6	17.0±0.9
^{137}Cs	35.0±1.8	35.9±1.8
^{241}Am	41.8±2.1	42.5±2.1

5 Conclusion

The γ-rays response functions of the ^{3}He proportional counter for energy range from 20keV (monoenergetic x-ray) to 1.333MeV (^{60}Co) were calculated by the EGS4 Monte Carlo code. The calculated pulse height spectra were compared with the experimental data and showed good agreements. The measured activities also showed good agreement with the reference activities calibrated by a manufacturer. It is concluded that the EGS4 simulation is available for the estimation of γ-ray response function for neutron detectors used in a neutron field.

References

[1] G. F. Knoll, "Radiation Detector and Measurement", Second Edition, John Wiley & Sons, Inc.

[2] W. R. Nelson, H. Hirayama and D. W. O. Roger, *SLAC-265* (1985).

[3] N. Takeda and K. Kudo, *IEEE Trans. on Nucl. Sci.* 41 (1994) 880-883.

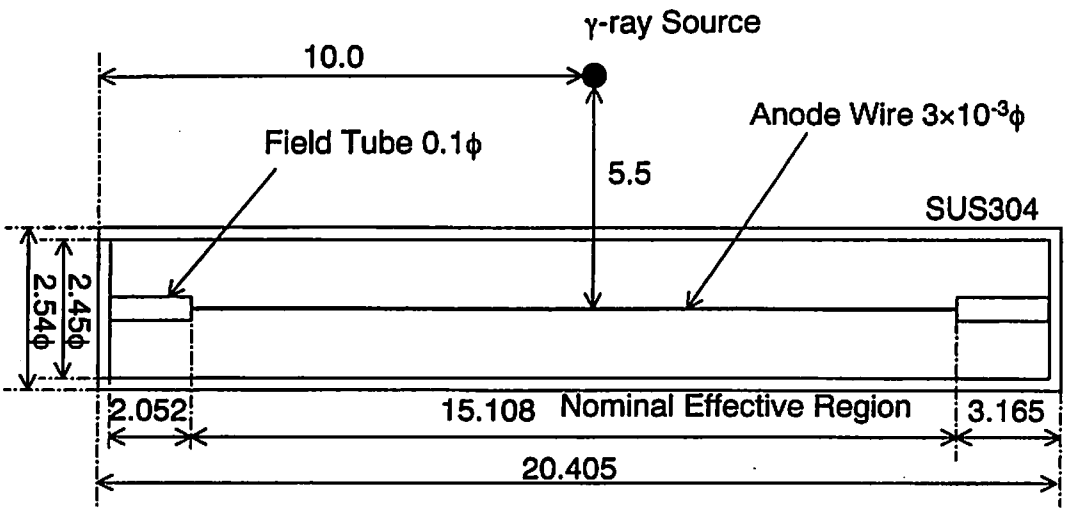

Fig. 1 A layout of the γ-ray response measurement for a ^{3}He proportional counter.

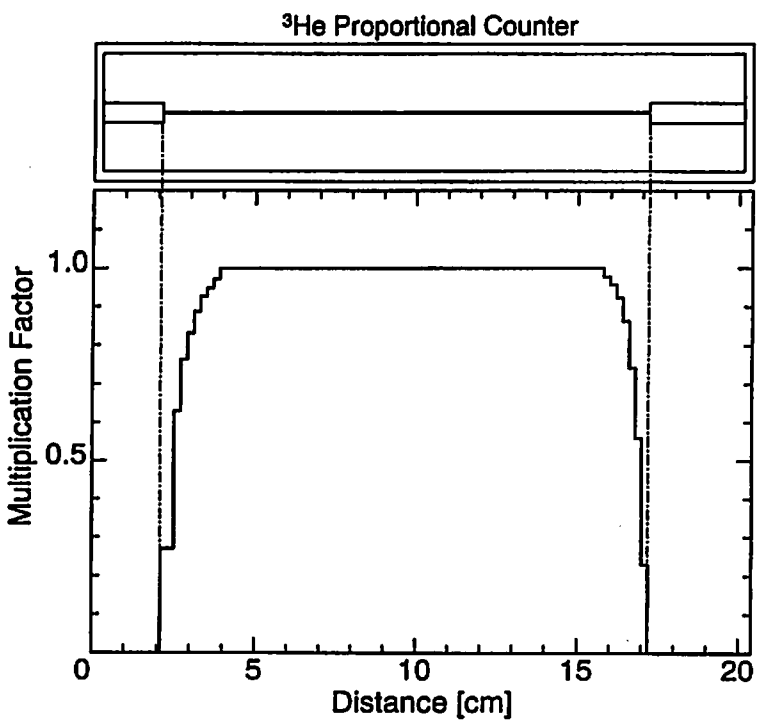

Fig. 2 Gas multiplication factor as function of position.

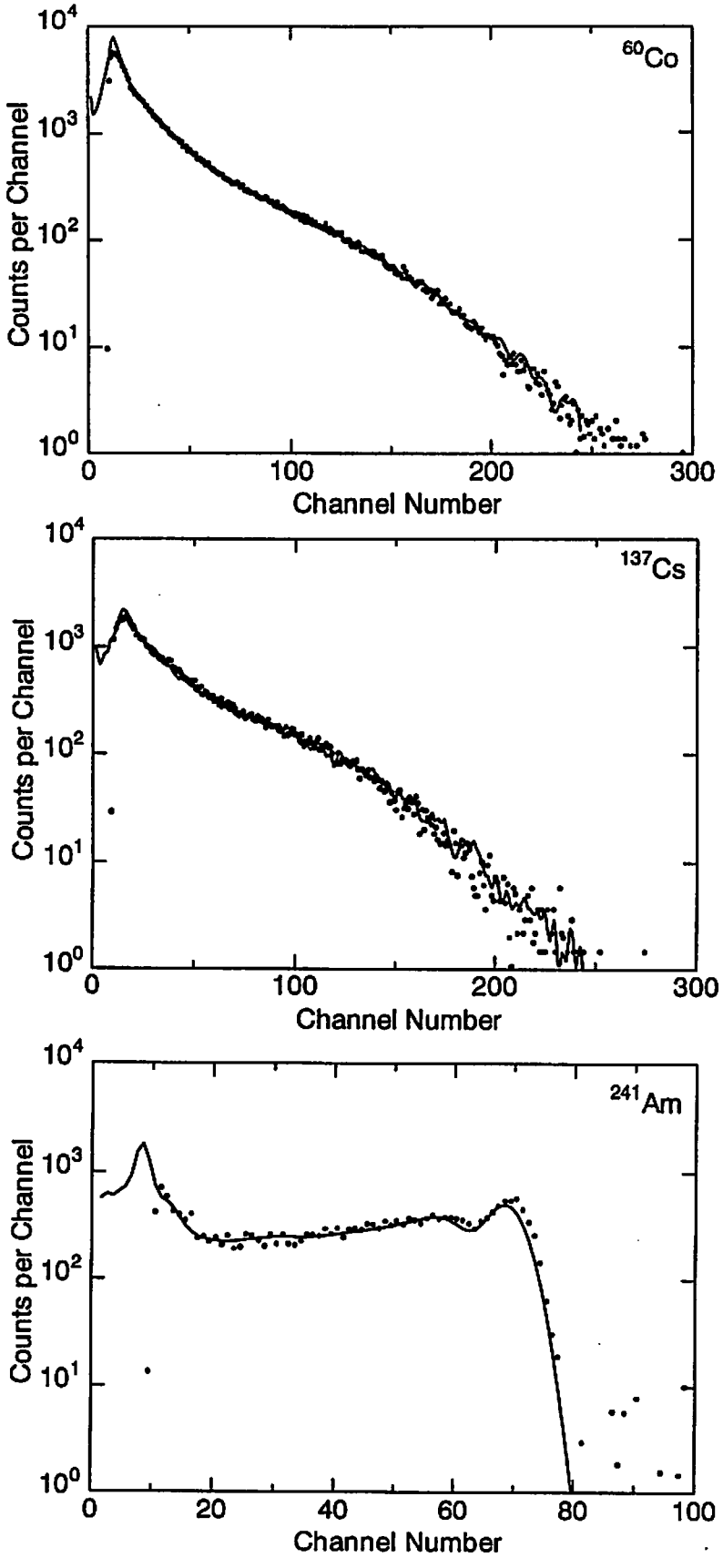

Fig. 3 Measured (dots) and calculated (solid line) pulse height spectra for the radio isotope γ-ray source.

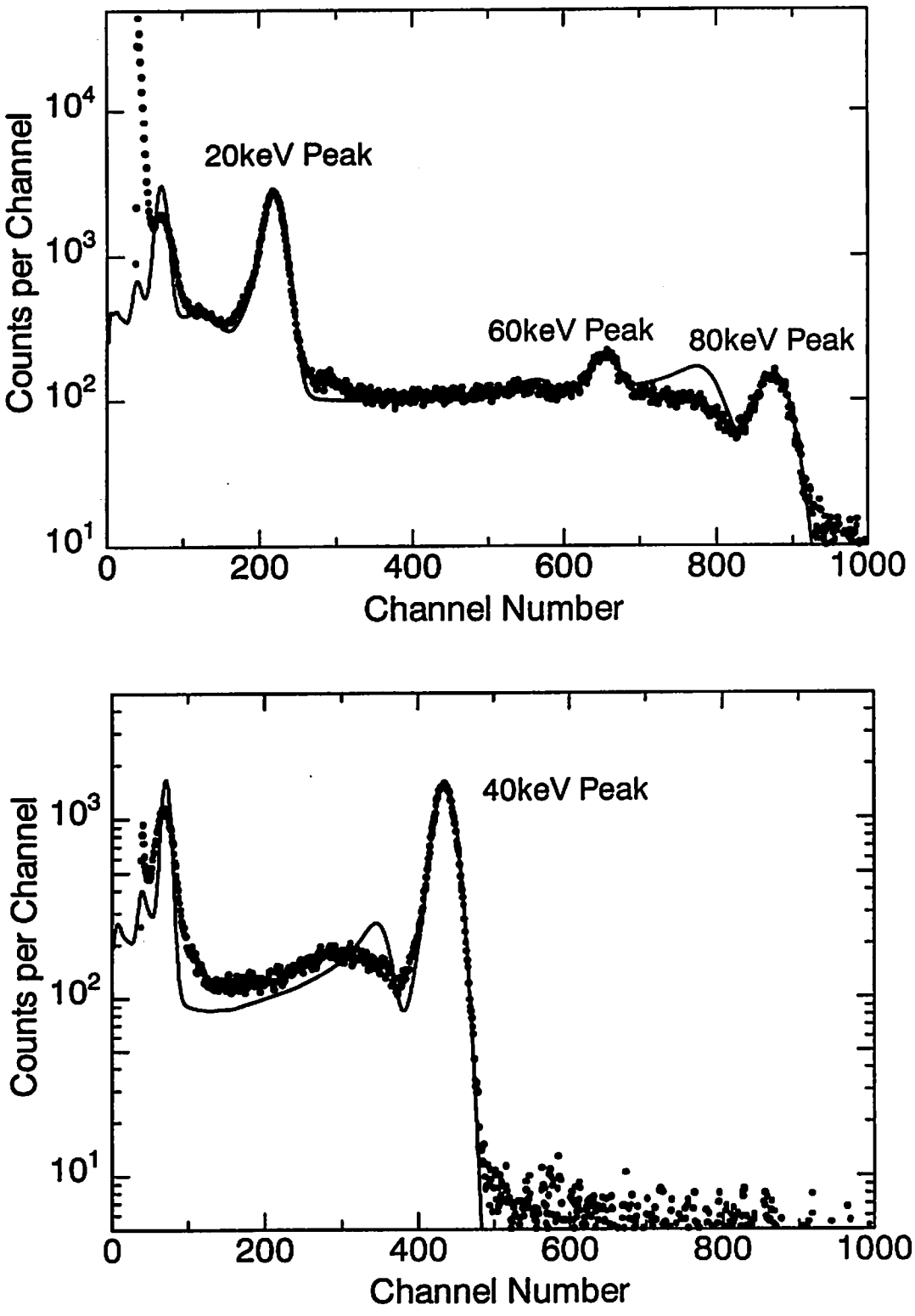

Fig. 4 Measured (dots) and calculated (solid line) pulse height spectra for the monoenergetic X-ray.

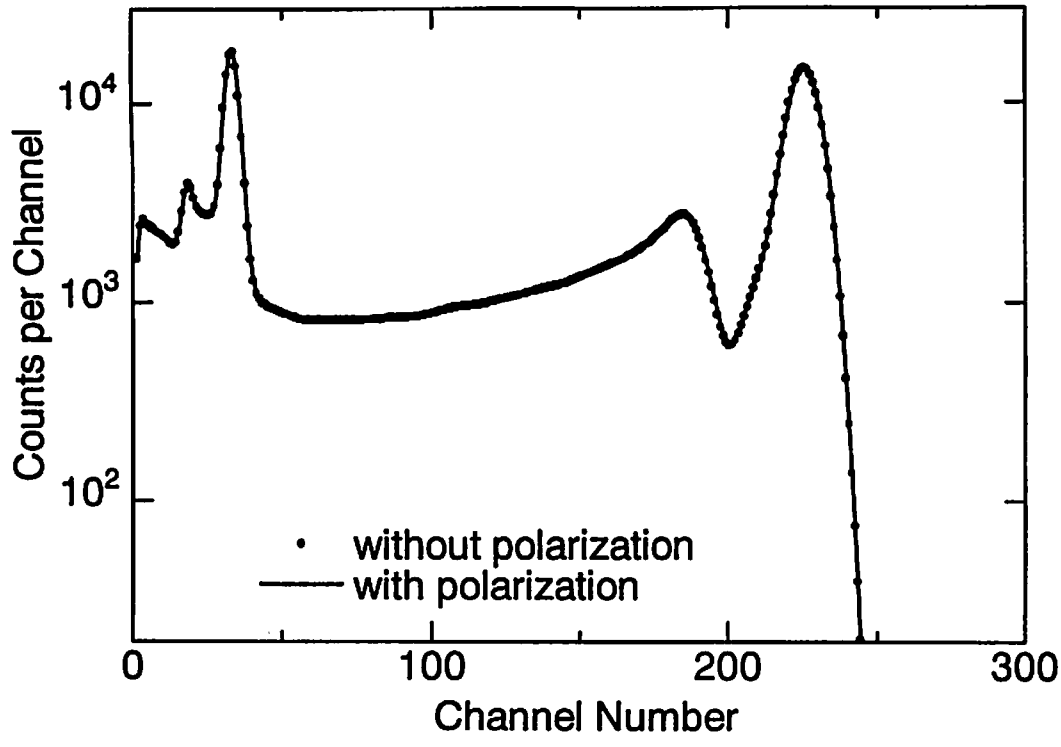

Fig. 5 Comparison of the response function with and without consideration of X-ray polarization.

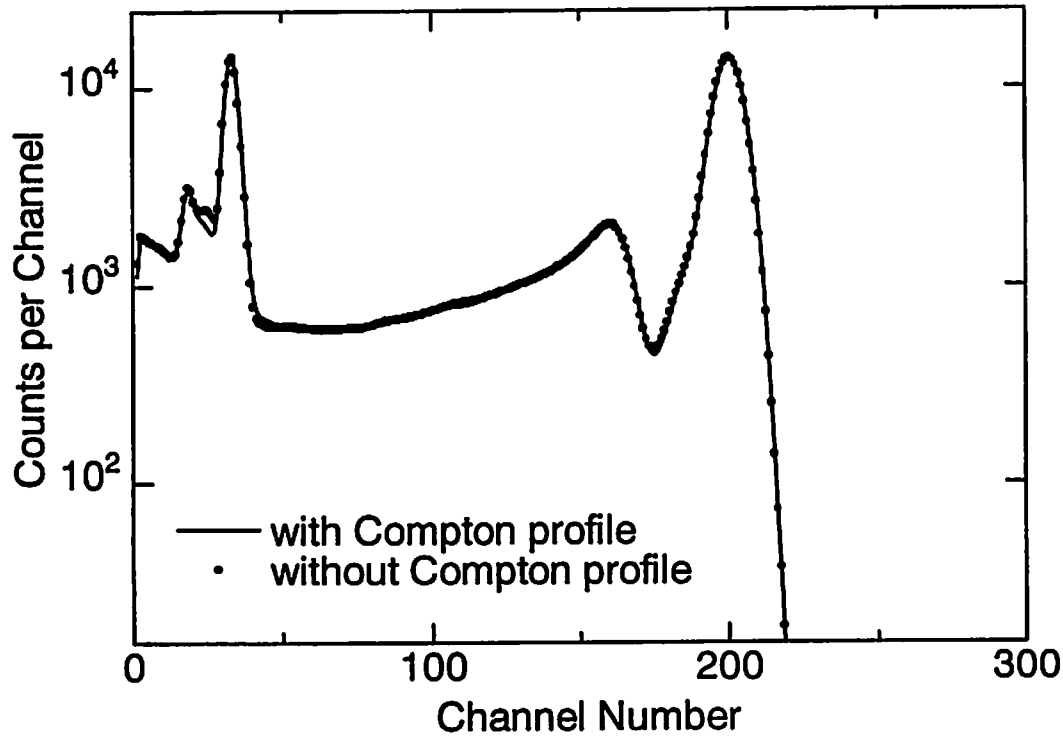

Fig. 6 Comparison of the response function with and without consideration of Compton profile.

RESPONSE FUNCTION SIMULATION FOR HPGE AND BGO SCINTILLATION DETECTOR FOR MONOENERGETIC ELECTRONS UP TO AROUND 10 MEV

M. SHIBATA, Y. KOJIMA, H. UNO, T. UCHINO, H. YAMAMOTO, K. KAWADE, A. TANIGUCHI[1] and Y. KAWASE[1]

Department of Energy Engineering and Science, Nagoya University
Furo-cho, Chikusa-ku, Nagoya 464-8603, Japan

[1]*Research Reactor Institute, Kyoto University*
Kumatori, Sennan, Osaka 590-0494 Japan

Abstract

For determination of β-ray maximum energy of unstable nuclei far off stability line with HPGe detectors, it is necessary to determine response functions for monoenergetic electrons in order to unfold measured spectra. The response functions for some planer type Ge detectors were simulated and compared to experimental response functions. Furthermore the simulations of detection efficiency for new type β-ray detectors have been done. These simulations represented that a total absorption detector composed of two large BGO scintillators were powerful for measurements of high energy β-rays, while, for HPGe detector, it was important to raise the detection efficiency for side scattering bremsstrahlung as a high efficiency β-ray detector.

1 Introduction

Atomic masses are fundamental physical constants and essential quantities concerning nuclear stability. For determination of atomic masses, a β-ray maximum energy measurement is one of the reliable and precise methods. Particularly, a usage of HPGe detectors has advantages of good energy resolution and reliable energy calibration to high energy($\sim$10 MeV) with γ-rays. While, a disadvantage is that the response for electrons is quite complicated due to high atomic number for Ge(Z=32) compared to plastic scintillators or Si detectors(Z=14).

We have adopted small size planer type Ge detectors(LEPS : Low Energy Photon Spectrometer commercially available by ORTEC) as a β-ray detector so as to have less sensitivity for high energy γ-rays. The response functions for quasi-monoenergetic electrons have been determined experimentally up to 4.5 MeV using β-ray sources (^{90}Sr/Y, ^{38}Cl for β^--ray and ^{68}Ge/Ga ^{34}Cl for β^+-ray) and a β-ray spectrometer at KURRI(Kyoto University Research Reactor Institute). For much higher energy region(5$\sim$10 MeV), e^+/e^- cascade shower produced by electron LINAC beams at KURRI and some convenient hand-made electron spectrometers were utilized.[1,2] Using these response functions, the Q_β values of neutron-rich and -deficient nuclei have been determined with good accuracy(uncertainty of 50 keV) by means of Fermi-Kurie plot[3-5].

Nowadays, for measurements of high Q_β values and small amount radioactive nuclei like a new isotope, we are developing new type β-ray detectors, e.g. a total absorption detector, which consists of two large BGO scintillators. In these detectors, it is difficult to determine the response functions experimentally due to their geometrical conditions. So it is necessary to determine the response functions by simulation. This paper, as the first step of development, describes differences between experimental and simulated response functions for the LEPSs. Moreover some results concerning detection efficiency simulations for new type detectors are described.

2 Response Function Simulation for Monoenergetic Electrons

For measurements of β-ray, three LEPSs($36mm^{\phi}\times13mm^{t}$, $25mm^{\phi}\times13mm^{t}$ and $16mm^{\phi}\times10mm^{t}$) were used. The β-ray spectrometer at KURRI can measure up to 5 MeV electron/positrons. In these measurements, energy resolution of the β-ray spectrometer was set about 15 keV.

Figure 1 shows an obtained simulated and experimental response spectra with the LEPS ($36mm^{\phi}\times13mm^{t}$). In the simulation, the energy resolution was not taken into account. The response spectra are considered to be simplified in three parts, that is a full energy absorption(A), a bremsstrahlung escape(B) and a back- or side-scattering escape(C)(see an inset of Fig.1). Here, the differences in C between them are clearly observed. Figure 2 shows the energy dependence of each part in the spectra. It shows A and B by experiment are 60% smaller than those of simulation and C by experiment is larger than that of simulation. This character was similarly observed in all size LEPSs. Moreover this situation is also quite similar in positron response functions.

So far the reason is not clear, but in this simulation, the detector condition in simulation was too simplified. The detector was assumed that the Ge crystal was just covered with thin Al. It should be recalculated with more realistic geometrical condition including β source condition. However, it should be also mentioned that extremely good linearity could be obtained by means of Fermi-Kurie plots from the measured standard β-ray spectra of ^{32}P, $^{90}Sr/Y$, ^{38}Cl and so on after unfolding with the experimental response functions. It is considered, as far as Fermi-Kurie plot analysis is adopted, the experimental response functions for quasi-monoenergetic electrons reproduce real response functions of monoenegetic electrons fairly well.

3 Scattering Free β-ray Detector and Total Absorption Detector

As shown in Fig.2, the scattering part C becomes larger as electron energy rises. For detection of scattering electrons more efficiently, high efficiency detector, that is a scattering free detector, has been developed. This detector is composed of two identical LEPSs ($36mm^{\phi}\times13mm^{t}$)(Fig.3). They are put face to face in close geometry and measured energy sum of two detectors. In this case, it is difficult to get the response functions experimentally. They must be determined by simulation. In high energy β-ray, the geometrical condition, that is a distance of two detector, is most important factor to detect multiple scattering β-particles since the β-particles enable to go out easily from detectors during multiple scattering. As the results of measurements of ^{32}P, ^{42}K and ^{38}Cl, about 20% scattering electrons could detect in this geometry.

This scattering free detector can detect back-scattering electrons efficiently but it can not detect bremsstrahlung γ-ray owing to small crystal in high energy β-rays. In order to increase detection efficiency for bremsstrahlung, a total absorption detector, which has high efficiency and high energy resolution, is an ideal detector. However, it is difficult to fulfill two demands at a time. For high efficiency, a BGO scintillator is favorable. For high energy resolution, a large volume Ge array detector is possible.

The former total absorption detector, which consists of two large volume BGO scintillators ($120mm^{\phi}\times100mm^{t}$) put face to face, is under development. Energy sum of two BGO detectors is

measured. The simulated efficiency of this detector is shown in Fig.3. This detector can detect almost all radiation from source not only β-rays but also γ-rays. The efficiencies for β- and γ-ray are almost 100% and more than 70%, respectively. The energy resolution is worse than that of Ge detectors, but the efficiency is three order of magnitude larger than that of the LEPS. It is suitable for measurements of small amount nuclei like a new isotope. It is supposed to work coupled with an on-line mass separator in vacuum condition without a window of detector surface in order to decrease the energy loss as small as possible.

The latter detector is still planning. Figure 5 represents an evaluation of energy escape from large Ge crystal ($5cm^{\phi} \times 7cm^{t}$) for incident electrons. As shown in an inset of Fig.5, electrons go in to a crystal from left side. The "peak" represents full energy absorption in the crystal. The "forward", "side scatt." and "back scatt." represent the escape of each direction. It shows that, even in such a large volume Ge detector, the bremsstrahlung escape is quite large. At 8 MeV, back scattering electrons become small, while, side scattering escape by photons becomes about 50% of all escape. It is considered that side scattering escape is due to the compton scattering in the Ge crystal by high energy bremsstrahlung γ-rays. As the results, as not only good resolution but also high efficiency β-ray detector, the cluster detector in EUROBALL, which consists in seven large Ge crystals(The six crystals are put like flower petals surrounded one crystal), is effective. But it should have a thin Be window and It is favorable that it has a ΔE detector in front of center crystal in order to distinguish β-rays from γ-rays. Of course, putting two detectors face to face as close as possible is necessary for high efficiency detector.

4 Conclusion

The response functions for monoenergetic electrons for Ge detectors as a β-ray detector. The obtained response functions by experiment and simulation are different each other. It is necessary to make clear the reasons of these differences by simulation under more realistic condition. The usage of simulation code give us important information concerning development of new β-ray detectors.

References

[1] Y. Kojima, T. Ikuta, M. Asai, A. Taniguchi, M. Shibata, H. Yamamoto, K. Kawade, *Nucl. Instr. and Meth.* **B126** (1997) 419-422.

[2] A.Osa, T.Ikuta, M.Shibata, M.Miyachi, H.Yamamoto and K.Kawade, *Nucl. Instr. and Meth.* **A332** (1993) 169-174.

[3] T.Ikuta, A.Taniguchi, H.Yamamoto, K.Kawade and Y.Kawase, *J. Phys. Soc. Jpn.* **64** (1995) 3244.

[4] A.Osa, T. Ikuta, K. Kawade, H. Yamamoto and S. Ichikawa, *J. Phys. Soc. Jpn.* **65** (1996) 928-934.

[5] Y.Kojima, M.Asai, A.Osa, M.Koizumi, T.Sekine, M.Shibata, H.Yamamoto, K.Kawade and T.Tachibana. *J. Phys. Soc. Jpn.* in printing.

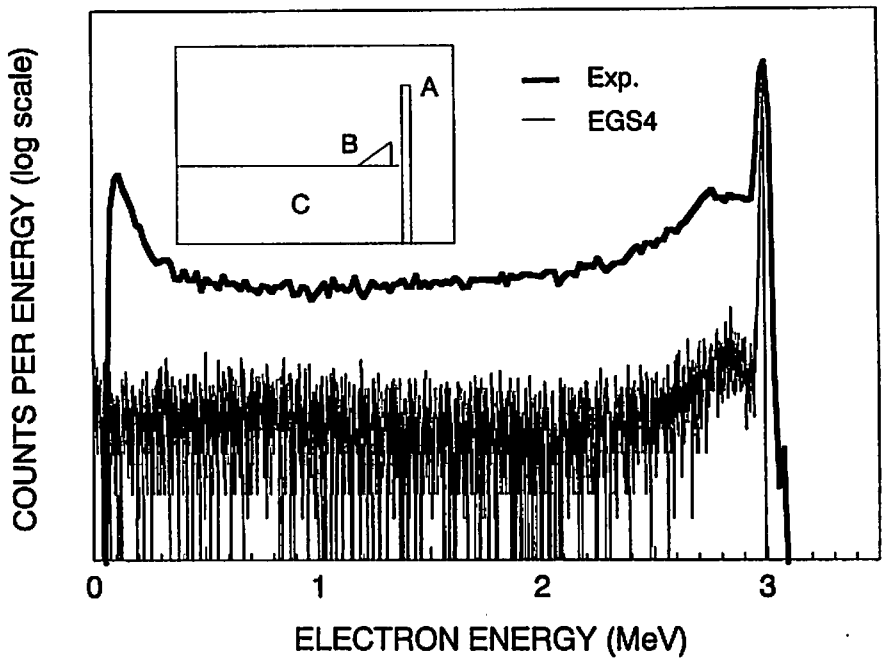

Fig.1 Typical response function for 3 MeV monoenergetic electrons for a Ge detector ($36mm^{\phi} \times 13mm^{t}$).

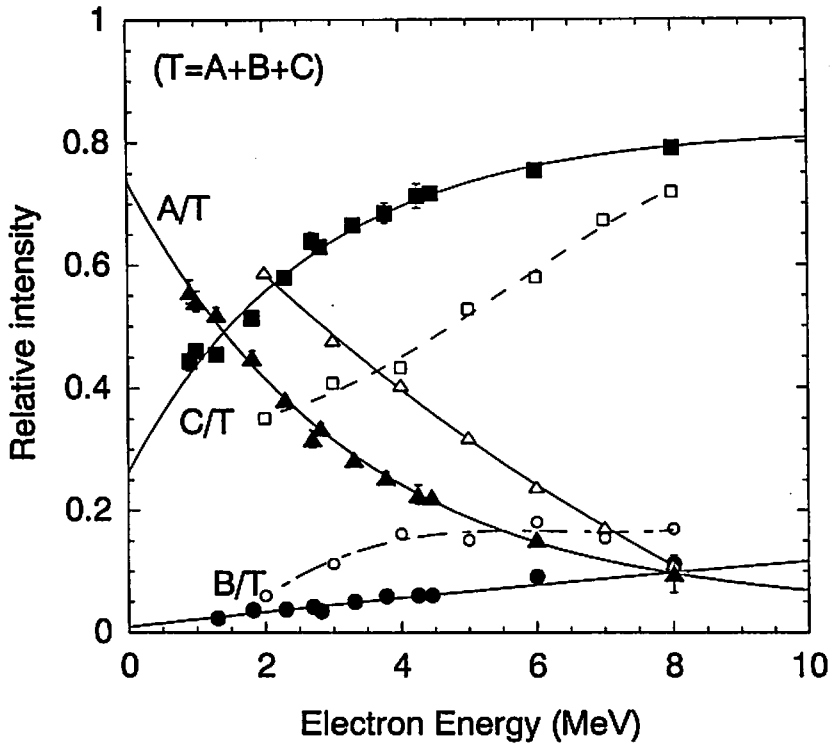

Fig.2 Energy dependense of the experimental and simulated response functions for monoenergetic electrons for LEPS ($16mm^{\phi} \times 10mm^{t}$). Solid and open symbols indicate the experimental and simulated data, respectively.

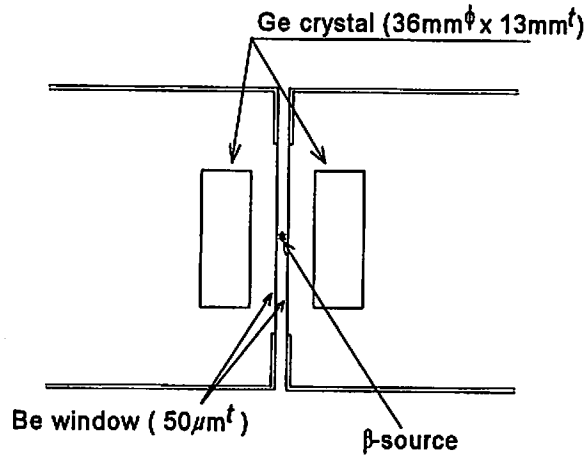

Fig.3 A schematic view of a scattering free β-ray detector.

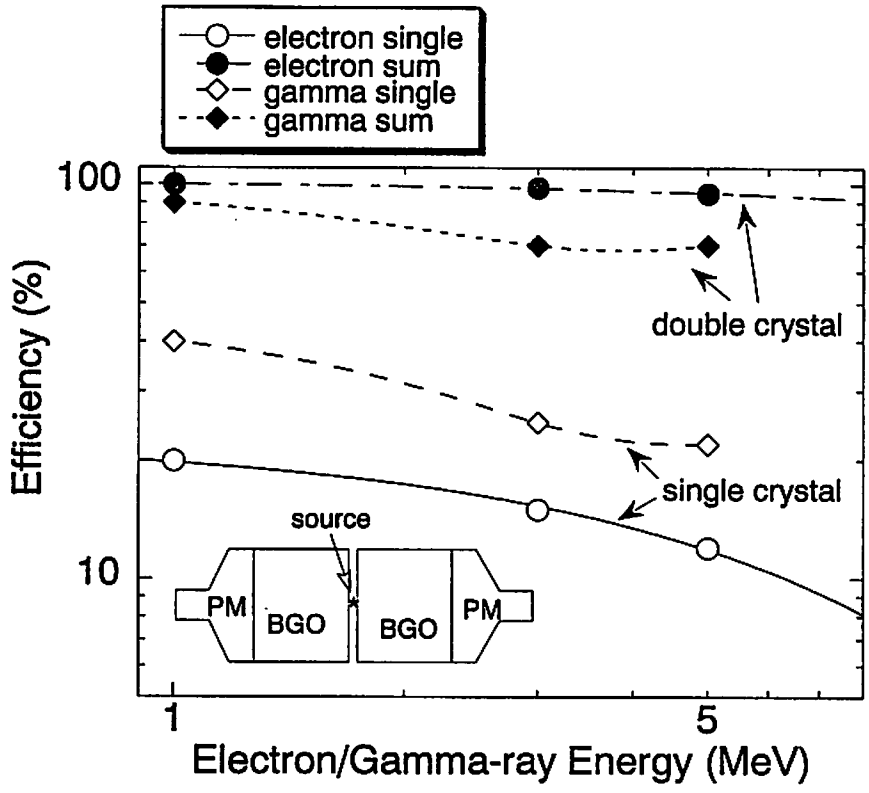

Fig.4 Simulated detection efficiencies for β- and γ-rays for single BGO detector(open symbols) and for a total absorption detector(solid symbols), respectively.

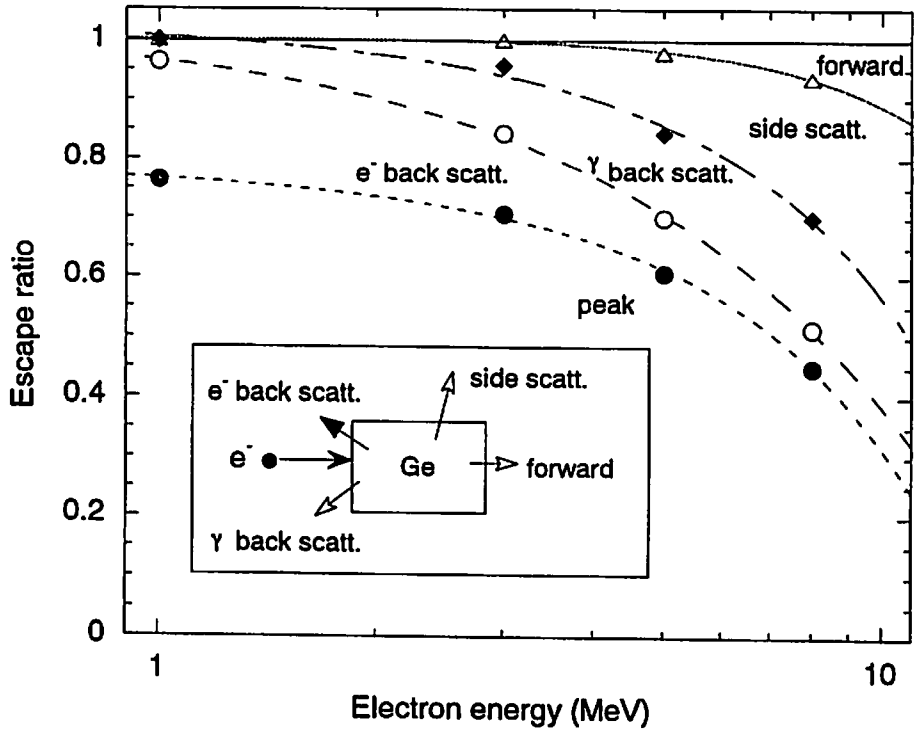

Fig.5 The energy escape ratio from a $5cm^{\phi} \times 7cm^{t}$ Ge crystal when electrons go into crystal as shown in an inset. The "peak" means the full energy absorption. The other parts represent the escape ratio of each direction as shown in an inset.

AN ADAPTIVE ESTIMATE OF A SUPERCONDUCTING MAGNET FOR A POSITRON FOCUSING DEVICE

H. TAKEI, T. EMOTO, Y. TANIMOTO*[2] and A. ENOMOTO*[3]

Japan Nuclear Cycle Development Institute [1] *(JNC)*
4002 Narita, Oarai-machi, Ibaraki 311-1393 Japan

**High Energy Accelerator Research Organization (KEK)*
1-1 Oho, Tsukuba-shi, Ibaraki 305-0801 Japan

Abstract

In the Japan Nuclear Cycle Development Institute (JNC), the following are examined as part of an application technology using a high power electron linac: monochromatic gamma ray sources, free electron lasers, and intense positron sources. This report presents an adaptive estimate of a superconducting magnet in order to efficiently converge a positron beam for the development of an intense positron source.

By comparing the intensity of a positron beam using a superconducting magnet with a normal conducting magnet, the intensity obtained is more than double. In addition, a small magnet is manufactured in order to examine the characteristics of the superconducting magnet as a solenoid coil. An excitement test is carried out with rated current. The result of measuring the maximum magnetic field on the central axis is 5.6 Tesla, which is the designed value.

1 Introduction

Presently, JNC is investigating the best way to treat high-level radioactive nuclear waste from reactors as a link in the chain of the Japanese government's policy; "OMEGA Project"[1]. For basic research into the transmutation of fission products, JNC developed a high-power CW electron linac for various applications: monochromatic gamma ray sources, free electron lasers, and intense positron sources.

As part of this application technology, basic research on the generation and convergence of an intense positron beam using an electron linac has been carried out. Until now, a converter target had been developed, which consists of heavy metal and functional gradient material to decrease the thermal stress. This report describes an adaptive estimate of a superconducting magnet in order to efficiently converge a positron beam for the development of an intense positron source.

[1]Power Reactor and Nuclear Fuel Development Corporation (PNC) was reorganized to JNC.
[2]Past staff at PNC
[3]Past guest scientist at PNC

2 Design Assumptions

A room temperature bore of a superconducting magnet is enough to include a target mounted inside a vacuum chamber, while the maximum magnetic field on the central axis is as large as possible. Therefore, the maximum value is set at 6 Tesla referring to a conduction cooled type superconducting magnet for X-band klystron [2], which has an extended bore. Let us assume that the superconducting magnet is located at the injector system in KEK.

3 Design Results

3.1 Size optimization

In designing superconducting magnets, it is taken into account that the critical current in the wire is limited by the cooling temperature and the magnetic field at the wire. In addition, the magnet volume must be minimized in order to hold the heat generation in the magnet by the radiation from a tungsten target. Considering these points, the dimensions of the magnet are optimized using Boom-Livingston's method [3]. Optimum dimensions are 330mm outer diameter, 250mm inside diameter, and 150mm length.

3.2 Comparison of positron intensities

In order to obtain the difference between a superconducting magnet and a normal conduction magnet, the orbit of the positron in each magnet is calculated, and intensities are compared to each other. First, positions and their momentum at the exit of the target are calculated using the EGS4 [4] code, provided that 10^3 electrons of 4 GeV are injected onto the cylindrical target with an optimum diameter of 8 mm, and thickness of 14 mm. The EGS4 code performs Monte Carlo simulations of the radiation transport of electrons, positrons and photons in any material. Second, using these values, equations of motion of the positrons in the electromagnetic fields are solved by numerical integration, the Runge-Kutta method, and orbits are obtained. Here, the electromagnetic system utilizes the beam transport system, that is, solenoidal coils, accelerater tubes, and quadrupoles at the injector system in KEK. The maximum magnet field on the central axis is set to 6.0 Tesla in the case of a superconducting magnet, and 2.3 Tesla in a normal conducting magnet.

Fig. 1 shows the relationship between the number of positrons and the transported length. The solid line shows the number of transported positrons using the superconducting magnet, and the dotted line shows positrons using the normal conducting magnet. As this result, the intensity obtained is more than double, even if the positron is transported about 13 m from the target.

3.3 Thermal analysis of the superconducting magnet

The superconducting magnet must be installed downstream of the target in order to increase the intensity of the positron beam. Because the magnet is installed downstream, however, the heat generation in the magnet increases, so the heat generation by the radiation from the target is estimated in this section. The energy deposit in the superconducting wire is calculated using the EGS4 code because a quench in the wire occurs by local heating.

3.3.1 Calculation model

The calculation model used in the EGS4 code is shown in Fig. 2. This model consists of the target, a lead, and the superconducting magnet. The target is made of tungsten, which has the same dimensions as in section 3.2. The exit of the target is located at the middle of the magnet.

The cylindrical lead is installed between the target and the superconducting magnet in order to shield the radiation. There are two types of thickness in this model: 25 mm and 50 mm.

Dimensions of the magnet are 330 mm outer diameter, 250 mm inside diameter. The length is 300 mm, which is doubled in section 3.1. The reason is for estimating the heat generation when the magnet is moved 150 mm upstream from the exit of the target.

The superconducting wire with 0.65mm diameter constitutes two materials, one is niobium titanium (NbTi) in the center, the other is copper around it. It is assumed for this wire that the material to generate the heat and maintain the superconductive state is copper, which is 1.8 times as heavy as NbTi. Therefore, the superconducting magnet with 40 mm thickness is supposed to be a collection of 20 copper cylinders, which are coaxial. These cylinders with 1mm thickness are spaced every 1 mm. In this model, the energy deposit of each cylinder for every 10mm length is calculated.

3.3.2 Setting cutoff energies

Cutoff energies in the EGS4 code must be decided, depending on the calculation model. Cutoff energies for electrons, positrons, and photons are set at six types: 20 keV, 50 keV, 100 keV, 500 keV, 1 MeV and 10 MeV, and the energy deposits in the tungsten, lead and copper are compared to each other. As cutoff energies increase, the calculation time shortens while the calculation accuracy tends to decrease.

In order that the calculation time shortens and the energy deposit corresponds with an accuracy of 10% of the deposit at the minimum value, 20 keV, cutoff energies are set to 1 MeV. However, cutoff energies in the lead with 50mm thickness are set to 100 keV so that the accuracy of the energy deposit in the copper is good.

3.3.3 Results

To give an example of the calculation, Fig. 3 shows the energy deposit in the first layer, the closest layer to the target, where the radiation damage was estimated to be hard. The maximum energy deposit of 10 mm length is found to be 20 mW, downstream of the target using a lead with 50 mm thickness. That is to say, the total energy deposit is 3W or less, when the magnet with 150mm length is installed downstream from the exit of the target. Therefore, it is possible to remove the total heat generation in the magnet, because the ability of a small liquid helium refrigerator is about 3W [5].

4 An Excitement Test with a Small Magnet

A small magnet is manufactured in order to examine the characteristics of a superconducting magnet as a solenoid coil. An excitement test is carried out with rated current. Although the magnet is smaller than the optimum magnet, the result of the excitement test may be reflected in the design of the superconduction magnet, since the value of the maximum magnetic field, 5.6 Tesla, is approximate to the optimum value.

Fig. 4 shows the result of measuring the magnetic field on the central axis. This result achieved 5.6 Tesla, which is the designed value of the small magnet.

5 Conclusion

This report describes an adaptive estimate of a superconducting magnet in order to efficiently converge a positron beam for the development of an intense positron source. Comparing the

intensity of a positron beam using a superconducting magnet with a normal conducting magnet, the intensity obtained is more than double.

In addition, a small magnet is manufactured in order to examine the characteristics of a superconducting magnet as a solenoid coil. An excitement test is carried out with rated current. The result of measuring the maximum magnetic field on the central axis is 5.6 Tesla, which is the designed value.

Therefore, it is confirmed to function as a focusing device, when the superconducting magnet is used to converge the positron beam.

Acknowledgment

We are deeply indebted to Prof. K. Hosoyama and Dr. T. Kamitani, KEK, for their considerable assistance.

References

[1] S. Toyama, Y. Himeno *et. al.*, "Transmutation of long-lived Fission Products (^{137}Cs,^{90}Sr) by a Reactor-Accelerator System", Proc. 2nd International Symposium on Advanced Nuclear Energy Research, 1990.

[2] S. Yokoyama *et. al.*, "Cryogen Free Conduction Cooled NbTi Superconducting Magnet for a X-band Klystron", *IEEE Transactions on Magnetics*, **vol.32**, no.4, July 1996.

[3] R. W. Boom and R. S. Livingston, "Superconducting Solenoids", Proc. of the IRE, March 1962.

[4] W. R. Nelson, H. Hirayama and D. W. O. Rogers, "The EGS4 Code System", *SLAC-265*, December 1985.

[5] R. Li, "Gifford-McMahon cryocooler", *OYO BUTURI*, **vol.67** no.4 (1998) 449.

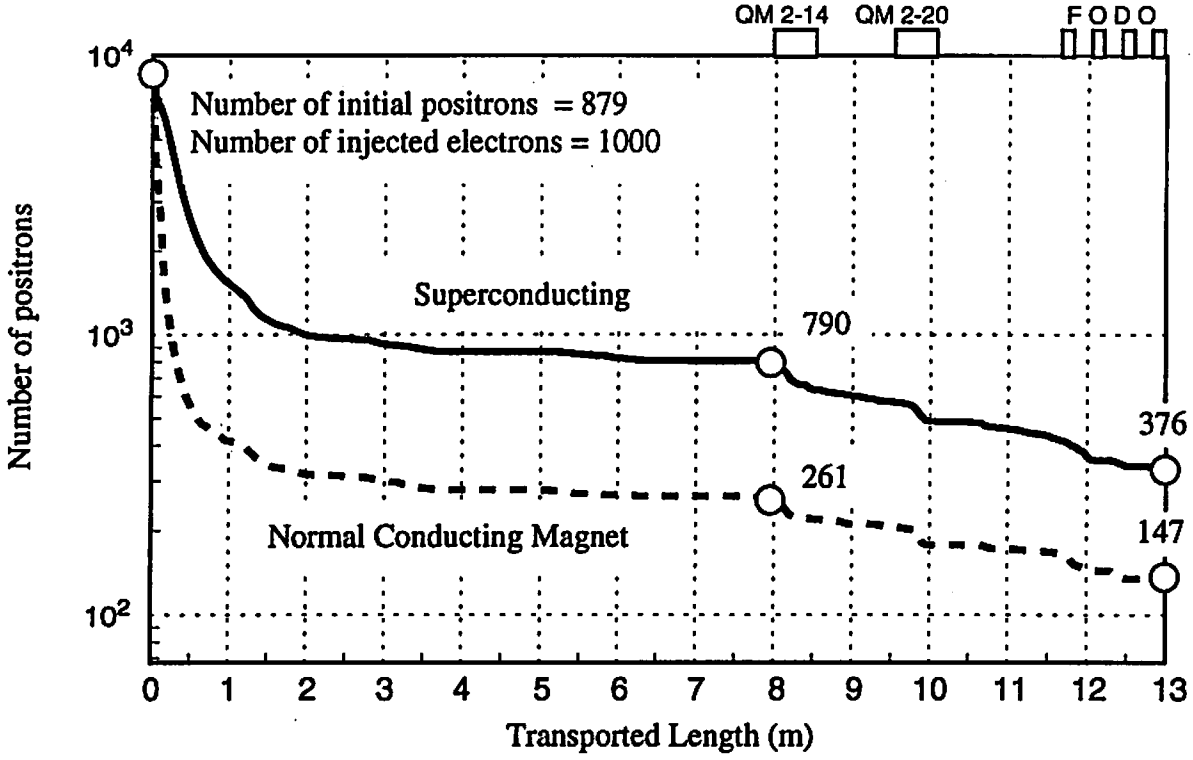

Fig. 1. Relationship between the number of positrons and the transported length

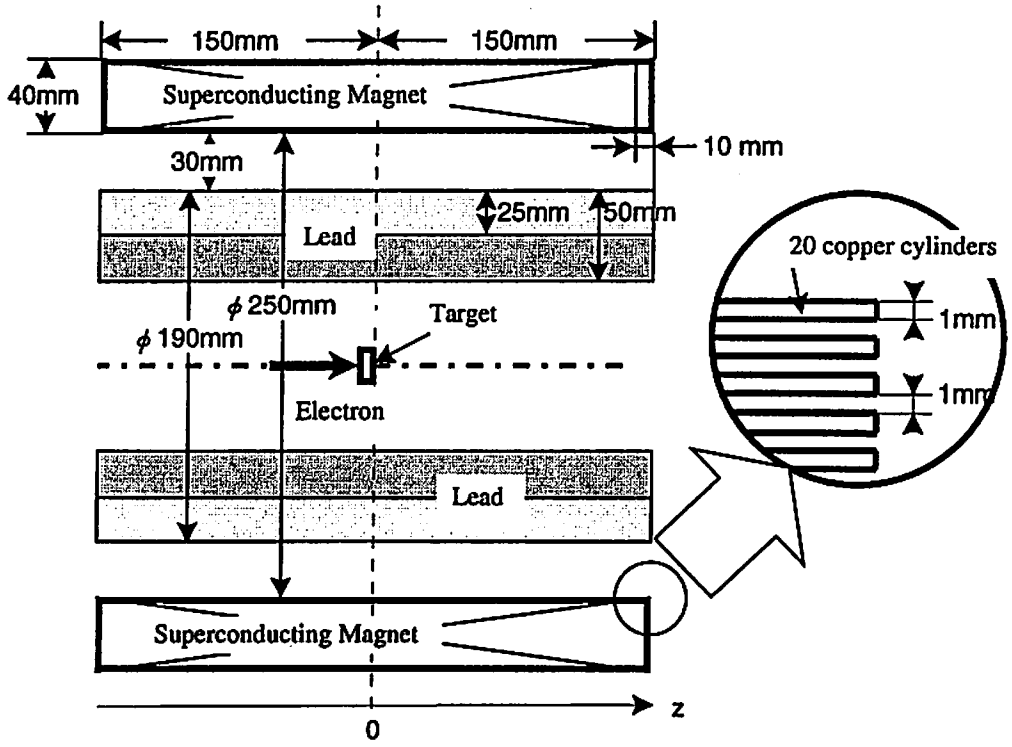

Fig. 2. Cross-sectional view of the calculation model in the EGS4 code

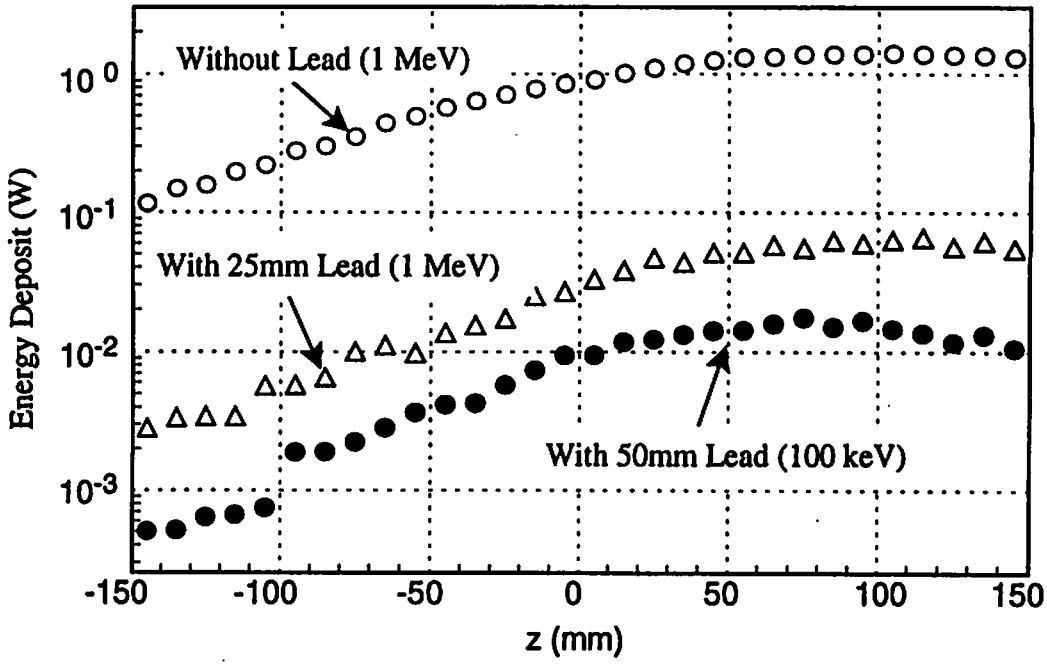

Fig. 3. Energy deposit in the first layer. The number in the parenthesis presents cutoff energies in materials.

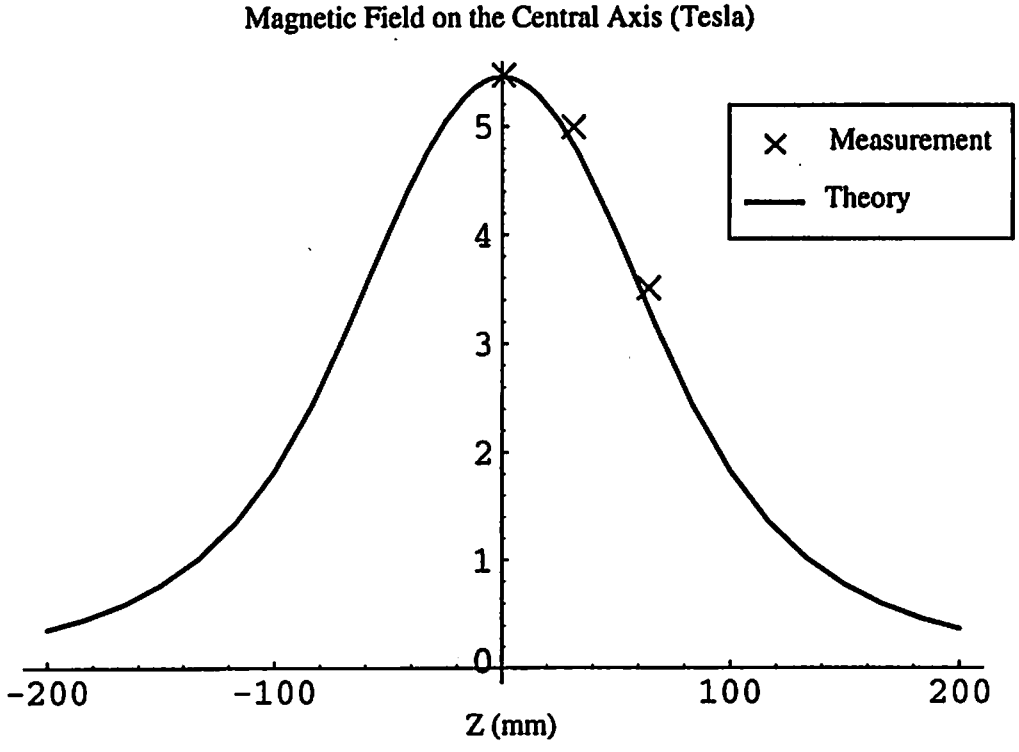

Fig. 4. A result of measuring the magnetic field on the central axis

CALCULATIONS OF PULSE-HEIGHT DISTRIBUTIONS BY COSMIC-RAY ELECTRONS IN THE LOWER ATMOSPHERE

H.SAGAWA and I.URABE

Faculty of Engineering, Fukuyama University
Gakuen-cho 1, Fukuyama-shi, Hiroshima 729-0292, Japan

Abstract

Pulse-height spectra by muons and electrons could be separated of the pulse-height spectrum by cosmic-ray electrons from that measured by using a spherical plastic scintillator. The pulse-height spectra of cosmic-ray electrons were calculated on the basis of the probability distributions of absorbed energy of incident electrons with energies up to 10 GeV and the energy spectrum of cosmic-ray electrons in the lower atmosphere.

1 Introduction

From the view point of health physics, many studies have been carried out for the estimation of the cosmic-ray dose which is one of the main sources of external exposures in the natural environment.[1] A spherical plastic scintillation spectrometer has been used for measuring system of cosmic-ray charged particles at the place of interest. Since this system was useful to detect flux density of cosmic-rays in a short time, it is often used for the estimation of variation of cosmic-ray doses around nuclear facilities. This method was based on the assumption that the energy loss per unit path length in the crystal is constant for both cosmic-ray muons and electrons.[2,3] But, it was quite possible that the flux density of cosmic-ray charged particles included some errors by the difference of their energy deposition mechanism in the crystal. So, in this investigation, the probability distribution of energy absorption by electrons in the plastic scintillator was calculated, and pulse-height distribution of cosmic-ray electrons in the atmosphere was estimated.

2 Calculation

The scintillation spectrometer used for cosmic-ray measurements was shown in Fig.1. The pulse-height distributions were obtained using a spherical plastic scintillator of 7.6cm in diameter. In the coincidence counting method, cylindrical plane organic scintillator of 10cm in diameter and 2cm in thickness was set for obtaining gate signals. The absorbed energy spectra of cosmic-ray electrons were simulated for the single detector and the coincidence counting method using the EGS4 Monte Carlo code.[4] In this calculation, the program that was changed in the region of UCNAI3P.MOR was used. The spherical scintillation detector was assumed to be consisted of many cylindrical scintillators shown in Fig.2. Radii of cylinders were determined so that the volume

of each cylinder equal to volumes of the divided part of the spherical scintillator. The radius of the inmost side of the cylinder was 1.4cm, difference between the internal radius and the external radius of most outer cylinder was 0.08cm.

A longitudinal section of organic scintillators is schematically shown in Fig.3. The materials were allocated to the numbers in the region of each block shown in the figure. The blocks with lightly dotted were polystyrene resin $(CH(C_6H_5)CH_2)n$. The blocks with darkly dotted show the regions of the detector consisting of many cylindrical scintillators. When single detector was simulated, blocks with lightly dotted were set to air material. And when coincidence method was simulated, the blocks were set to polystyrene material. No painted blocks show air regions. Electron isotropically entered to the lightly dotted areas. Cut off energy of electrons and photons were 0.521MeV and 0.01MeV, respectively. Histories of 10^7 were calculated for the determination of probability distributions of absorbed energy caused by cosmic-ray electrons below 10GeV. The energy spectrum of the cosmic-ray electrons reported by O.C.Allkofer was used for the calculation of pulse-height distributions given by cosmic-ray electrons in the natural environment.[5]

3 Results

Results of calculation of pulse-height distribution by cosmic-ray electrons were shown in Fig.4. The horizontal axis shows the electron energy absorbed in a plastic detector, the vertical axis shows the counting rate at each energies. The result of single detector and coincidence method were shown by solid triangles and open triangles, respectively. These results show that follow.

- Unlike muons count rate of cosmic-ray electrons were large at low energy as a whole.
- Above energy of 15MeV, counting rates were markedly decreased with higher energy. This energy change with a detector size.
- Under energy of 15MeV, counting rates by single detector were larger than by coincidence method. Counting rate of electrons was easily influenced by the cylindrical plane scintillator for coincidence method at lower energy.

4 Conclusions

Though the pulse-height distribution of cosmic-ray could be determined by using the coincidence counting method, much attention had to be paid to the distortion of pulse-height spectra for estimation of flux density of cosmic-ray electrons in the lower energy region.

References

[1] Rep.UNSCEAR, "Sources, Effects and Risks of Ionizing Radiation", 52 (1988),UN.

[2] Y. Nakashima and S. Furuta, *J.Japan Health Phys. Soc.* 16, 83-97 (1981).

[3] I. Urabe, Y. Ogawa, T. Yoshimoto, T. Tsujimoto and Y.Nakashima, *J.Health Phys.* 32, (1997).

[4] W. R. Nelson, H. Hirayama and D. W. O. Rogers, *SLAC-265* (1985).

[5] O. C. Allkofer, "Introduction to Cosmic Radiation", 106-130 (1975), Verlag K Thiemig.

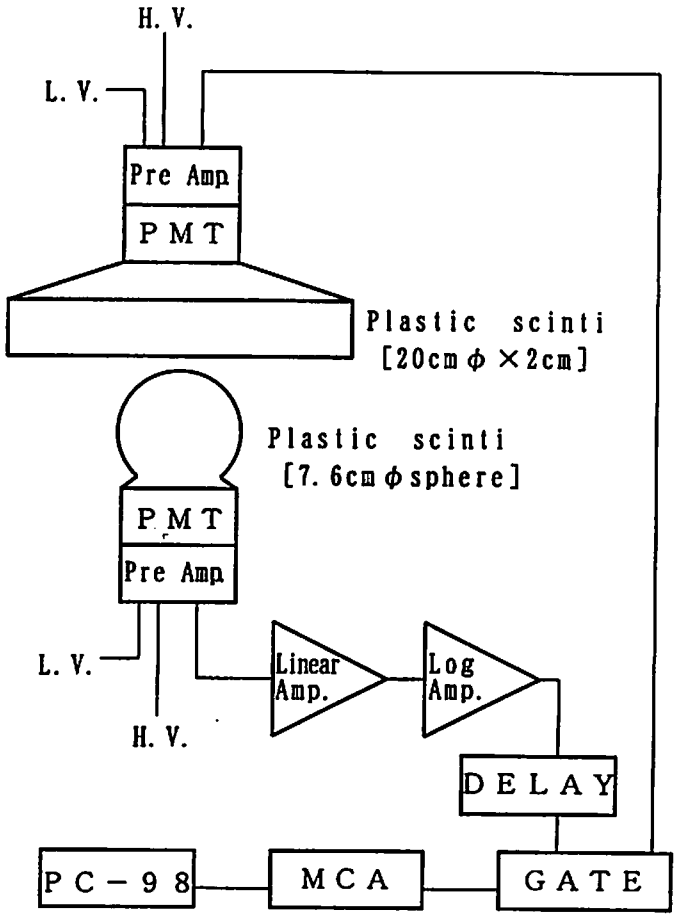

Fig.1 Measuring system for estimation of flux densities of cosmic-ray charged particles.

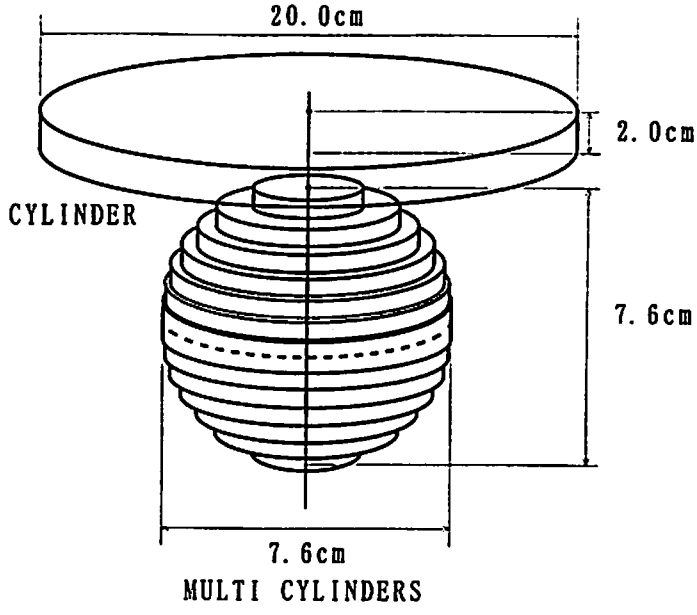

Fig.2 Model of multi-cylindrical detectors used for simulation of electron behavior in a spherical scintillator and a cylindrical scintillator.

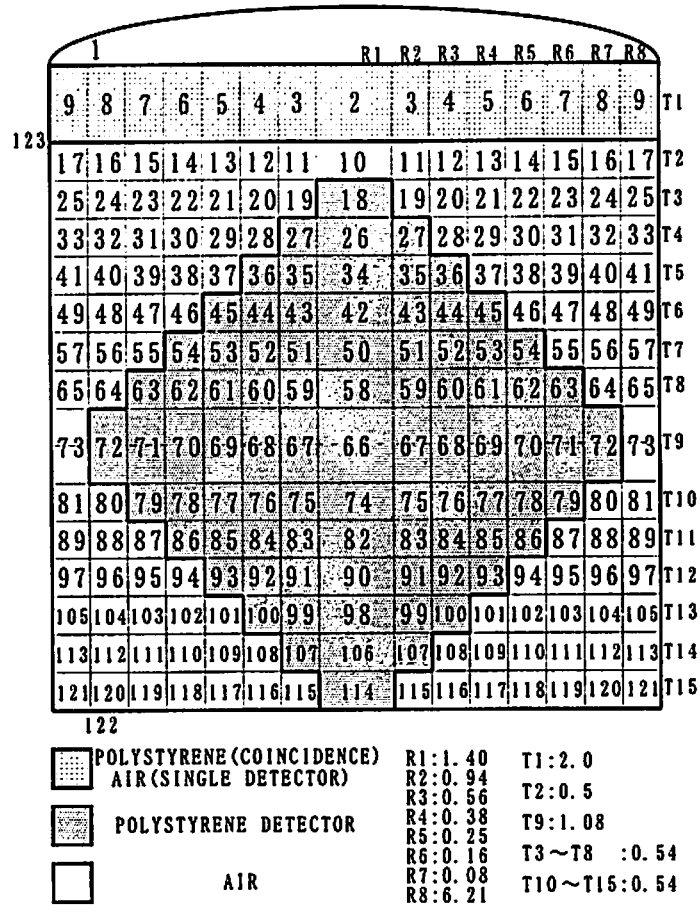

Fig.3 A longitudinal section of organic scintillators and the numbers allocated in the region.

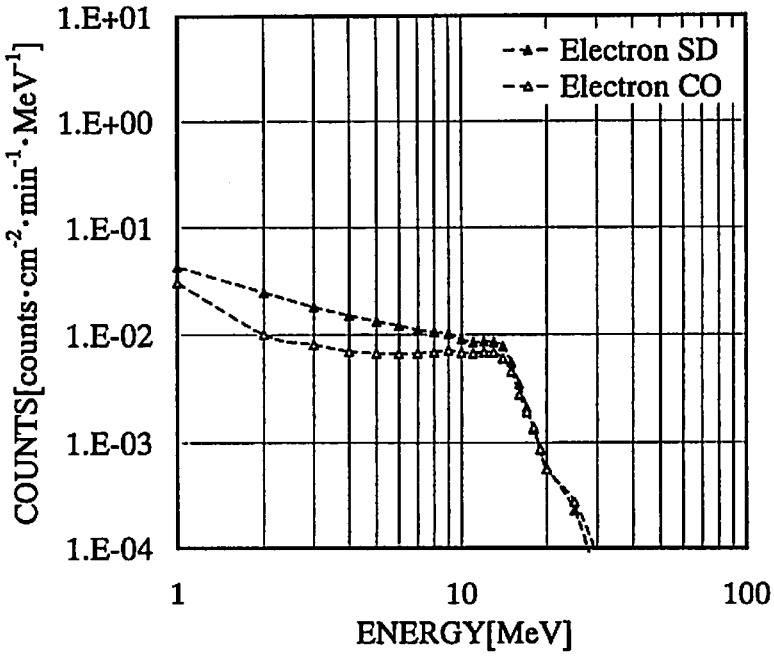

Fig.4 Pulse-height distributions by cosmic-ray electrons calculated by using the EGS4 Monte Carlo code.

MEASUREMENT OF PHOTO-NEUTRON YIELD FROM THICK LEAD TARGET BOMBARDED BY 1.2 GeV ELECTRONS

K. SHIN, T. SATO, S. BAN[1], H. NAKAMURA[1],
Y. NAMITO[1], H. HIRAYAMA[1], and S. ROKNI[2]

Department of Nuclear Engineering, Kyoto University,
Yoshida, Sakyo-ku, Kyoto 606-8501

[1]*High Energy Accelerator Research Organization,*
1-1 Oho, Tsukuba, Ibaraki 305-0801, Japan

[2]*Stanfor Linear Accelerator Center,*
Stanford CA 94309, USA

1 Introduction

Recently, number of high energy electron accelerators is vastly increasing for generation of SOR or FEL. As a source term of these electron accelerator facilities, data of thick target neutron yield are strongly required. Unfortunately, there is almost no measured data of the neutron yields for intermediate and high energy electrons. The only one measurement reported is the one by Eyss et al.[1], where 150~270 MeV electrons were used and thick target neutron yields at 90° were measured by TOF method, using about 26-m long flight path. Above this energy range, no measurement has been reported. Generally the electron accelerators mentions above are in GeV energy range, and the neutron yield data at this energy range are now strongly requested to be measured.

The final goal of our work is to extend the data of Eyss et al. to higher energy range without using a dedicated TOF facility. In this report, we describe results of the preliminary trial experiment, by which we searched for an appropriate experimental conditions to measure neutrons at about 1 GeV electron energy with relatively short flight path condition.

2 Experimental Method

The measurement was made at the ATF Linac of KEK. Used electrons were at 1.2-GeV energy, and are pulsed to 10 ps width with repetition rate of 6.25 Hz, where the beam current was 3×10^8 e/pulse.

A Pb target of 50-mm width by 50-mm height and 20-mm thickness($\sim$ 3.9 rl) was located in a vacuum chamber and irradiated by electrons of 1×10^{12} per each run, which corresponds only 10-minute irradiation. Neutrons emitted at 90° were detected by 2-in. diameter by 2-in. length PILOT-U plastic scintillator, which was shielded by 10-cm thick lead collimator of 40-cm length, at

a distance of 5.6 m from the target. Figure 1 shows experimental arrangement of the measurement. The 1-m thick concrete shield was located at 1.8-m height above the beam line and a 16-cm diameter detecting hole was drilled just above the target. To suppress the gamma flash 10-cm thick lead shield with 3-cm wide slit was located on the target chamber. Also 5~15 cm thick lead shield was put at the exit of the detecting hole. Additional lead shields were located around the exit shield of the detecting hole and the detector collimator.

The time analyzer of 0.5 ns time resolution was utilized in the measurement. Since the n-γ discrimination technique was unable to be applied, neutrons and gamma rays were separated by only flight time difference. The discrimination level in the pulse height was determined by the pulse height of ^{60}Co, ^{137}Cs and Am-Be sources. The level was varied during the experiment to search for the optimal level to avoid disturbance due to reflection of very large gamma flash pulse. Finally the discrimination level was set at about ^{60}Co gamma-ray Compton edge in pulse height.

The background was estimated with a 25-cm iron plug being put not the 15-cm lead shield at the exit of the detecting hole.

Since the lead collimator covered the detector, neutron efficiency may be affected by injection of scattered neutrons or secondary gamma rays from the collimator to the detector. To calibrate these effect, neutron efficiencies at 35, 70, 90 and 135 MeV were later measured by quasi-monoenergetic neutron field at cyclotrons of Riken and CYRIC of Tohoku University. It was found from these measurements that the collimator contributions to the detector efficiency was dominant at lower pulse height (less than about 3 MeVee), and for the discrimination level set at the ATF experiment, the influence was about 30%.

3 Analysis

The measured time spectra were converted to energy spectra and correction was made for the neutron attenuation by the lead shield at the exit of the detecting hole, by using total cross sections of lead, where the detector efficiency was estimated by the SCINFUL code[2] (assuming NE-110) and Cecil's code[3] (NE-213) without the lead collimator in the model.

The calculation of the neutron spectrum was made by the following procedure;

1. Estimate gamma-ray energy and spatial distributions by EGS4;
2. Calculate differential photo-neutron production cross sections at 90° by modified PICA95/4/ at many photon energies;3)Multiply the photon fluxes with cross sections and integrate over the energy and the target volume.

In this calculation, neutron and secondary hadron transport in the target was completely neglected. The lead shield on the path from the target to the detector was not considered. Since our interest is in the higher energy component, evaporation component was not included in the PICA95 calculations.

4 Results and Discussions

Before comparing the calculation with the present experiment, we test the calculation method by the data of Eyss et al. Results for the Pb target are demonstrated in Fig. 2 at 150 and 266 MeV. Note that low energy part below 15 MeV should not be compared with each other because of the neglect of evaporation component in the calculation. It is seen that at 150 MeV, the calculation underestimates the measured data by 30~100%. The agreement between the calculated and the measured data is better for 266 MeV, although a structure seen in 70~100 MeV in the experimental data was not reproduced by the calculation. The reason of this discrepancy is due to the neglect of pion re-absorption reactions in target nuclei.

Keeping these results in mind, the calculated one shown in Fig. 3 for the ATF experiment looks too small as compared with the measured data. The discrepancy is over a factor of 4.

The attenuation curves of neutrons were measured with varying the thickness of the lead shield at the exit of the detecting hole. We checked the attenuation rate at several energies from 10-cm lead thickness to 15 cm thickness. It was found the attenuation rate was much smaller than that estimated with the lead total cross sections.

Then we used nonelestic cross sections, which gave closer attenuation rate to measured one than the total cross sections did, for the correction of the lead attenuation effect. Also the detector efficiency was increased by 30% taking the collimator influence into the consideration.

The final result of the measured data is compared in Fig. 4, giving much better agreement with the calculation. It is pointed out that in higher energy part above ~70 MeV the measure data looks higher than the calculated one, although the statistics of the measured data are very bad.

It is concluded that the measurement of photo-neutrons is possible by the present experimental condition. However, since many lead shields were used around the target-detector line such as the gamma-flash shield, detector collimator, lead slit on the chamber, additional shield around the collimator. The target itself also works as shield. The result of the present experiment is very sensitive to the attenuation correction by the gamma flash shield. There are possibilities of disturbance by neutron production and scattering in these shield, in addition to the influence due to the secondary hadrons. We need to make more sophisticated calculation to correct these effects. These are for future work, since we concentrated on showing the possibility of photo-neutron measurement the present report.

5 Conclusion

We searched for the possibility of detecting photo-neutrons at the ATF Linac facility without a special TOF equipment flight tube. And it was showed that the measurement of photo-neutrons is possible by the present experimental condition. However, the result of the present experiment was very sensitive to the attenuation correction by the gamma flash shield. We need corrections based on sophisticated calculations to get much better neutron yield data; photo-production of neutrons and other hadrons and their transport in lead shields used on and around the target-detector line.

Acknowledgments

The authors wish to thank Dr. J. Urakawa and Dr. N. Terunuma in the ATF for their support in carrying out the experiment.

References

[1] H. J. Eyss and G. Luhrs, *Z. Physik* **262**,393 (1973).

[2] K. Dickens,"SCINFUL:A Monte Carlo Based Computer Program to Determine a Scintillator Full Energy Response to Neutron Detector for En between 0.1 and 80 MeV", *ORNL-6436* (1988).

[3] A. Cecil et al., *Nucl. Instr. Methods* **161**, 439 (1978).

[4] T. Sato et al., "Radiative Nuclides Induced in Al, Fe, Cu, Nb, Au and Pb Foils by Irradaiation of 2.5-GeV Electrons in Beam Stop", Proc. 1998 ANS Rad. Protec. Shielding Topical Conf., April 19-23, 1998, Nashville, Tennessee, pp. II-379.

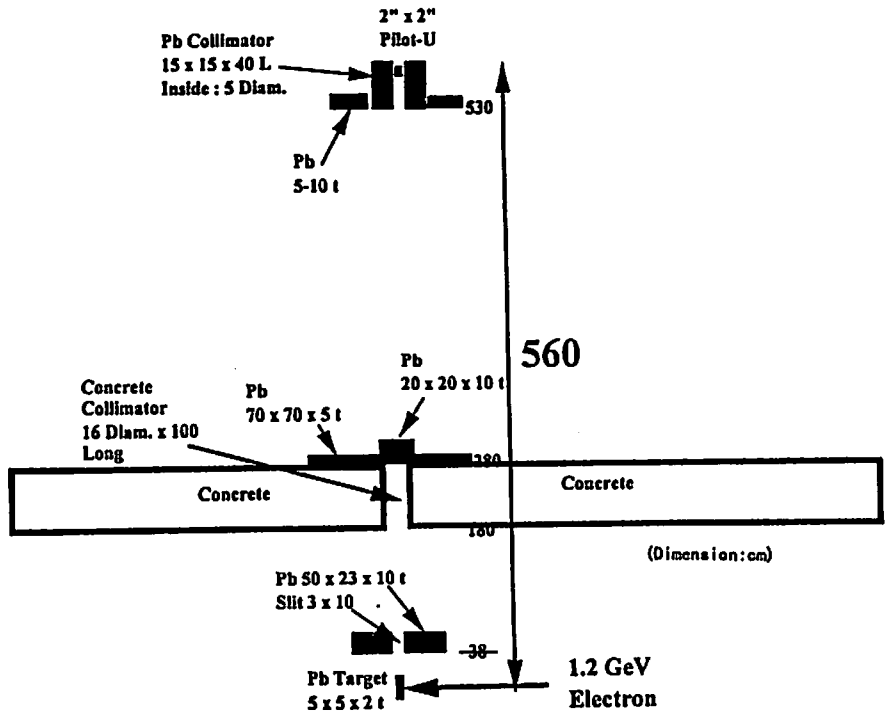

Fig.1 Experimental arrangement.

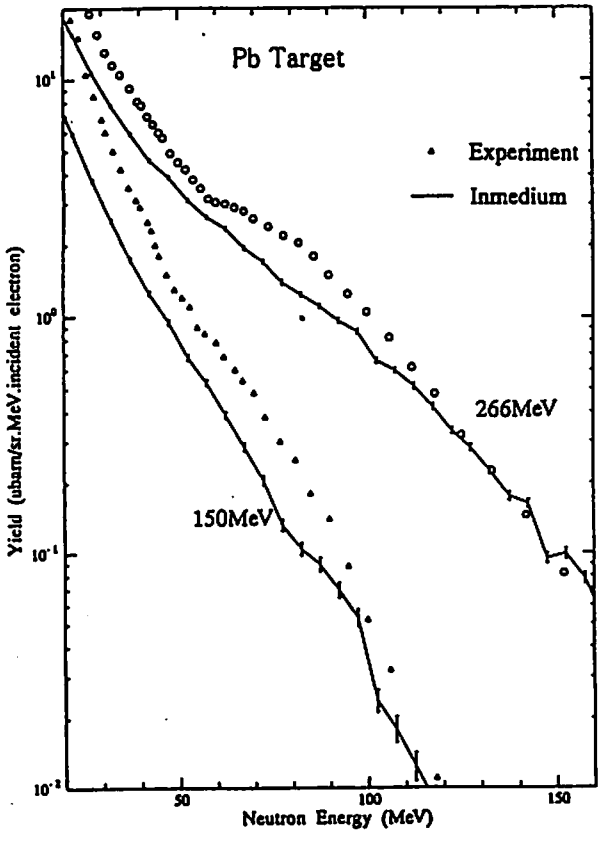

Fig.2 Comparison of neutron yields between present calculation and Eyss experiment.

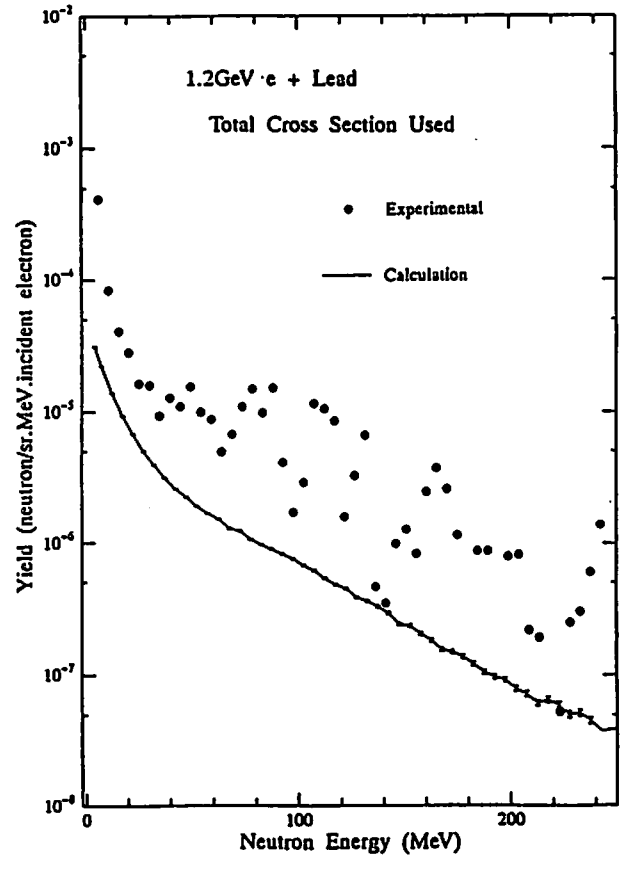

Fig.3 Comparison of measured neutron yield obtained with correction by total cross sections with calculation.

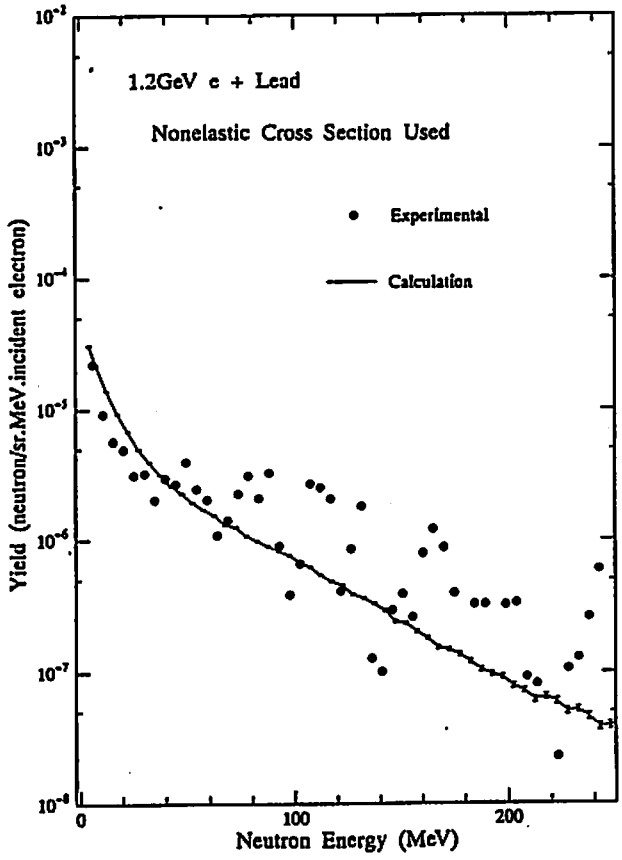

Fig.4 Comparison of measured neutron yield obtained with correction by nonelastic cross sections with calculation.

FUNDAMENTAL RESEARCH OF SUBPICOSECOND TIME RESOLVED X-RAY DIFFRACTOMETRY USING ELECTRON LINAC

H. HARANO, K. KINOSHITA, K. YOSHII, T. UEDA and M. UESAKA

Nuclear Engineering Research Laboratory,
Graduate School of Engineering, University of Tokyo
2-22 Shirakata, Shirane, Tokai, Naka, Ibaraki, 319-1106 Japan

Abstract

We have proposed a new pump-and-probe technique, subpicosecond time resolved X-ray diffractometry, which enables the direct observation of the lattice movement in the transient processes of the subpicosecond order. This technique uses a subpicosecond electron pulse from a linac, which produces various radiations as a pump pulse and the characteristic X-ray in a copper target as a probe pulse. Using the EGS4 code, we have found that the subpicosecond X-ray pulse can be generated in a sufficient intensity and purity for this technique. Preliminary experiments have been also performed using the NERL electron linac and several diffraction images were obtained for typical monocrystals such as silicon.

1 Introduction

Recent remarkable progresses on ultrashort pulse generation technology brought entirely new possibilities to change the current static way of material property research into dynamic one. The electron single pulses of 700 fs[1] and 440 fs[2] are available from the S-band twin linear accelerator (linac) system at the Nuclear Engineering Research Laboratory (NERL). The X-band linac has been planned to be introduced in future, which is evaluated to produce 100 fs pulse[3]. Here, as the new application of these linacs, a new pump-and-probe technique, subpicosecond time resolved X-ray diffractometry is proposed, which enables the direct observation of the lattice movement, namely the temporal change of the three-dimensional atomic arrangement in the transient phenomena of the subpicosecond order. This technique uses a subpicosecond electron pulse from a linac, which produces various radiations like a transition radiation[4] as a pump pulse and the characteristic X-ray in a copper target as a probe pulse.

Fig. 1 shows an example of the system configuration in case of using the far-infrared coherent synchrotron radiation as a pump pulse. The time delay between these two pulses is controlled only through adjustment of the path length of the pump pulse, so this method has an intrinsic advantage that there is no time jitter which may cause serious problems in adding up accumulated results. Further, by choosing the pump pulse properly, various ultrafast phenomena can be treated such as lattice vibration (phonon), thermal expansion, phase transition and so on, which may result in experimental verification for the existing solid state physics and molecular dynamics calculations.

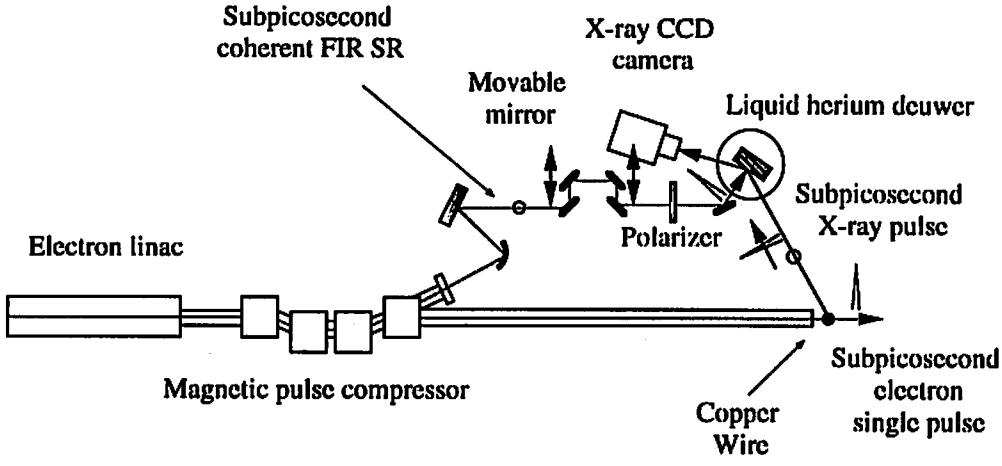

Figure 1. Schematic of linac-based subpicosecond time resolved X-ray diffractometry system.

In this study, the converted X-ray probe pulses have been totally characterized numerically using the EGS4 code[5] and their applicability to this technique is investigated. Preliminary experiments have been performed to generate the characteristic X-ray pulses and to obtain their diffraction images for several typical monocrystals at the linac.

2 Simulations

In this technique, the electron pulses impinge upon the copper wire and converted into KX-ray pulses. The KX-ray generation is mainly occured through the two channels: 1. bremsstrahlung followed by K-shell photoionization (PI) and 2. K-shell electron-impact ionization (EII). The latter process is domimant in the electron energy range of 18-35 MeV available from our linacs but not treated in the default EGS4 code. Here, the modified version of the EGS4 code is used which Y.Namito et al.[6] have developed to include the K-shell EII. In the EGS4 calculation, the incident electron beam with the monoenergy of 35 MeV is pencil-like (zero width) and incident perpendicularly on the central axis of the copper wire.

Strong angular dependencies were found in both the X-ray intensity and spectrum. Fig. 2 shows the calculated spectra of forward-emitted and side-emitted X-ray from the $100\mu m\phi$ copper wire. Each spectrum is normalized to have unity at the KX-ray's peak position($\sim$ 8.1keV). The fraction of the background, mainly due to the bremsstrahlung, of the side-emitted X-ray was smaller than that of the forward-emitted X-ray by a factor of about 100. The characteristic X-ray is isotropically generated, while the bremsstrahlung is forward generated. Most of the X-rays were found to be emitted sharply straight forward. However, we should make use of the side-emitted X-ray in order to realize high S/N measurement.

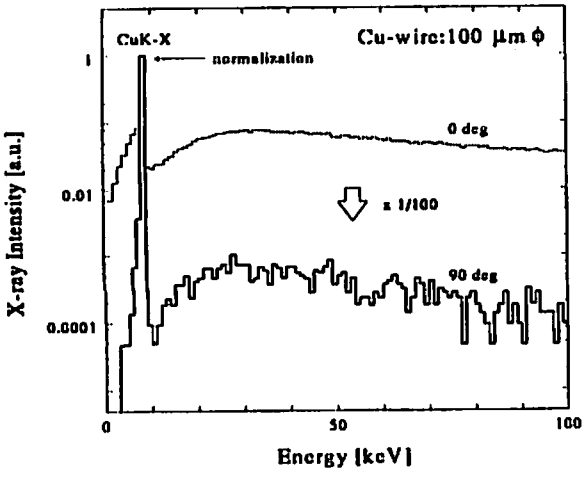

Figure 2. Comparison of (a) forward-emitted and (b)side-emitted X-ray spectra.

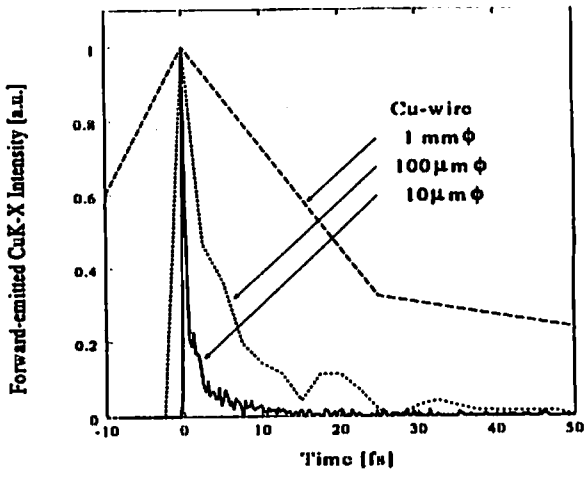

Figure 3. CuK-X pulse shapes for various sizes of copper wire.

As shown in Fig. 3, the pulse shapes were also calculated by adding up the transit time of the every trasport step in the EGS4 user code. The hole in the K-shell has an ultrashort lifetime of about 1 fs[7], which was disregarded so that the KX-rays were emitted immediately after the K-shell ionization. The incident electron pulse duration was regarded as zero. The obtained pulse durations of the forward-emitted KX-ray were much shorter than that of the actual electron pulses, that is, subpicosecond. This slight elongation of the KX-ray pulse duration is mainly due to the multiple scattering of the electron before the EII. It should be noted that the side-emitted KX-ray pulse is subject to much more pulse expansion due to the geometrical factor since there is a certain time lag of the KX-ray genaration at upstream and downstream. The light travels 300 μm for 1 ps. Of course, this time lag will be cancelled for the forward-emitted KX-rays if the electron energy is relativistic.

Table 1 summarizes the calculated results for various sizes of the copper wire. The imaging plate (IP) is an excellent imaging device and widely used for not only an X-ray diffractometry but also many purposes. Typically, it has a significant sensitivity to the X-ray energy of less than 150 keV. For the side-emitted X-ray, the S/N ratio is defined as the ratio of the KX-ray to the other IP-sensitive X-ray. The number of the KX-ray reaching the sample crystal surface per pulse is also tabulated. For this derivation, it was assumed that the electron pulse of 1 nC was generated at 10 pps and the sample of several cm^2 located 1 m from the copper wire. Further, the irradiation time necessary to form the Bragg spot composed of the 10000 diffracted KX-rays was roughly estimated assuming that the diffraction efficiency was 1/100. It can been seen from Table 1 that the subpicosecond X-ray pulses are generated in enough intensity and quality for this technique and the copper wire of around 100μmϕ was found to be optimum.

Table 1. Summary of the calculated results.

Diameter of Copper Wire	10 μmϕ	100 μmϕ	1 mmϕ	10 mmϕ
Pulse Duration	0.2-0.3 fs	2-3 fs	20-30 fs	-
S/N Ratio	$\sim$ 7	$\sim$ 6	$\sim$ 0.4	$\sim$ 0.003
KX-rays on Sample	$\sim$ 10	$\sim$ 200	$\sim$ 500	$\sim$ 500
Irradiation Time	$\sim$ 3 hrs	$\sim$ 10 mins	$\sim$ 5 mins	$\sim$ 5 mins

3 Experimenys

Based on the above information obtained from the EGS4 simulations, preliminary experiments have been done at the NERL linac. The experimental configuraion is shown in Fig. 4. The sample monocrystal was mounted on the goniometer, and it was placed inside the lead shielding together with the imaging plate for taking photographs of the X-ray diffraction image. For the photoneutron shielding, the polyethylenes were provided around the lead shielding and the beam dump consisting of the carbon block. The X-ray pulses were generated from the copper foil/wire irradiated by the linac electron pulse and lead to the surface of the sample crystal through the slit of 5 mm width in the lead shielding. The linac produced the multi-bunch pulse of 1 ns duration with the electron energy of 28 MeV at the frequency of 50 pps. The electric charge per pulse was a little less than 1 nC and the beam size was about 5 mmϕ.

Fig. 5 shows the diffraction image by the Si(111) plane for the silicon wafer. The irradiation time was about 20 minutes and the copper foil of 15 μm^t was employed for the X-ray converter. Three types of spot were seen on the image, the direct X-ray spot from the copper foil, the shadow behind the silicon wafer and the Bragg spot. For Si(111) plane, the Bragg angle of the KX-ray is 14.24 degrees, while the Bragg spot appeared only in the goniometer angle of 14-14.75 degrees. The diffraction images for the GaAs(400) plane and the NaCl(200) plane were obtained as well. Using the copper wire of 100 μmϕ, we also succeeded in taking the finer Bragg spot composed of two clearly separated lines due to the CuK$\alpha_{1,2}$.

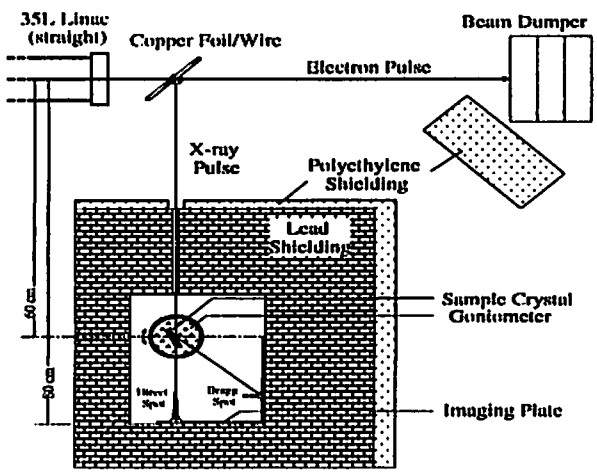

Figure 4. Experimental setup of the X-ray diffractometry at NERL linac.

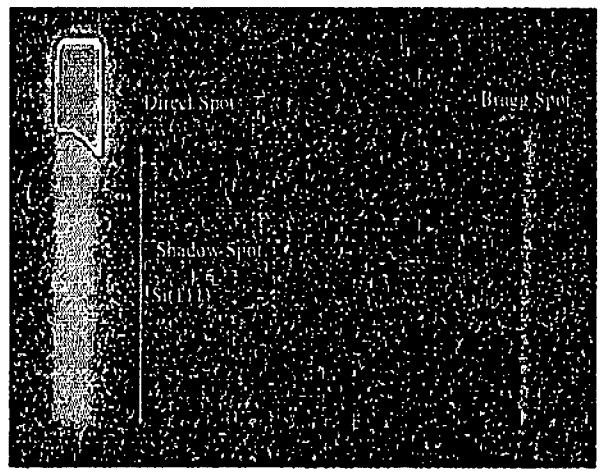

Figure 5. Si(111) diffraction image for 15 μm^t copper foil.

4 Summary

The subpicosecond time resolved X-ray diffractometry was newly proposed and its feasibility with the NERL linacs were investigated. By the EGS4 code simulation, the size of the copper wire, as the X-ray converter, was optimized so that the subpicosecond X-ray pulses were generated with the sufficient intensity and quality. Preliminary experiments have been carried out using the NERL linac and the diffraction images of the CuKX-ray were obtaied for several typical monocrystals successfully.

References

[1] M.Uesaka et al., *Phys. Rev. E* **50**, 3068 (1994).

[2] M.Uesaka et al., *Proc. of APAC'98* (1998) (in press).

[3] A.Takeshita et al., *Nucl. Instrum. and Methods* **B** (1998) (in press).

[4] T.Watanabe et al., *Proc. of APAC'98* (1998) (in press).

[5] W.R.Nelson et al., *SLAC-265* (1985).

[6] Y.Namito et al., *Nucl. Instrum. and Methods* **A** (1998) (in submission).

[7] S.T.Manson et al., *Atomic Data and Nuclear Data Tables* **14**, 111 (1974).

RELATIONSHIP BETWEEN DOSE IN TEETH AND EFFECTIVE DOSE FOR PHOTON INCIDENCE

F. TAKAHASHI, Y. YAMAGUCHI, M. IWASAKI[1] and C. MIYAZAWA[1]

Department of Health Physics, Japan Atomic Energy Research Institute
Tokai-mura, Ibaraki-ken 319-1195, Japan

[1]*School of Dentistry, Ohu University*
31-1 Misumido, Tomita-machi, Koriyama-shi, Fukushima-ken 963-8611, Japan

Abstract

Relationship between dose in teeth and effective dose was studied for some photon incidences in order to develop a method that enables to predict individual dose based on doses in teeth measured by ESR. Absorbed dose in some teeth parts and effective dose were calculated using EGS4 code in combination with a mathematical phantom. Experiments were also performed to determine the absorbed dose distribution in the mouth with TLDs put in a head phantom made of tissue-equivalent materials. Comparison between calculated and measured results gave a good agreement. Results on relationship between dose in teeth and effective dose can be useful for individual dose estimation in accidental or retrospective situation.

1 Introduction

Electron spin resonance (ESR) dosimetry using dental enamel is expected to be a promising technique for monitoring dose to a human body, in the case where no dose information can be taken from dosimeters, such as in radiation-accident and retrospective situations [1]. The ESR signal in the dental enamel is proportional to the number of unpaired electrons produced by irradiation and consequently to the absorbed dose. Several groups examined ESR signals from many kinds of biological materials. The hydroxyapatite crystals in the dental enamel is considered to be the most favorable material at present, which can easily trap free electrons in the defects in the crystal lattice. Methodology for ESR dosimetry using dental enamel has been studied in detail [2,3] and applied for accident dosimetry in investigations of the victims of the Hiroshima and Nagasaki atomic bomb [1], and Chernobyl nuclear accident in 1986 [4].

The ultimate quantity to be estimated is the organ or tissue doses and/or effective dose, risk-weighted average of organ doses over a human body. Therefore the absorbed dose in teeth measured by ESR should be quantitatively related to these doses. We studied the relationship between dose in teeth and effective dose for photon irradiation by computational simulation and experiment using a realistic head phantom.

2 Computation

EGS4 code [5] in conjunction with user's code UCGEN [6] and a mathematical phantom was used to calculate absorbed doses to organs or tissues including teeth. The MIRD-5 type

mathematical phantom [7] was modified to calculated absorbed doses in some teeth parts. The teeth region composed by five parts was newly defined at the position where a part of the facial skeleton was scrapped away. Figure 1 shows the cross-sectional views of the mathematical phantom and teeth region. The track length estimator was used to calculate energy-differential fluences in each organ or tissue and the kerma approximation to convert them into absorbed dose. Photon parallel beam of energies from 20 keV to 2.5 MeV was assumed to be incident on the body in antero-posterior (AP) and postero-anterior (PA) geometries. In addition to those, dose calculations were performed for 10 incident angles with 30 degrees interval from AP to PA directions in order to study the angular characteristics of the doses.

3 Experiment

A very realistic head phantom placed on the Alderson RANDO torso phantom was exposed to gamma rays from ^{137}Cs and ^{60}Co sources. The head phantom is made of real human skull and polyurethane-based soft tissue substitute. Thermo-luminescence dosimeters (TLDs) of $CaSO_4(Tm)$ were set at tooth positions in the mouth to measure the absorbed dose in teeth. In addition to this experiment, another irradiation with ^{60}Co source was carried out using a set of real human teeth put in the mouth of the phantom. ESR measurement was performed for irradiated dental enamel samples separated mechanically from other part of the tooth and crushed into appropriate grain size [2].

4 Results and Discussion

Figure 2 shows a comparison of dose in teeth and effective dose in AP irradiation geometry as a function of incident photon energy. The tooth receives very higher doses than other tissues because it contains elements with higher atomic numbers such as Ca and P than those of soft tissue. For photons less than 100 keV, energy absorption through photoelectric effect is enhanced and the dose in tooth increases. For photons more than 200 keV, Compton scattering process is dominant interaction with tissues and energy absorption through this process does not significantly depend on the element. For this reason, the difference between dose in tooth and effective dose becomes small in this energy region.

Figure 3 shows an angular dependence of dose in tooth and effective dose for 1250 keV photon beam incident on the body in parallel. The dose in tooth is depicted as the dose averaged over all the teeth in the mouth. For incidences from the front with an extent of -60 to +60 degrees, the dose in tooth is very close to the effective dose. This means that we can think of the measured dose in tooth as the effective dose for 1250 keV photons incident from anterior and anteriorly oblique angles. For posterior and posteriorly oblique incidences, the effective dose appears to be higher than the dose in tooth, because the red bone marrow contained in the spine contributes to the effective dose. On the contrary, for incidence from right or left lateral side, the dose in tooth is higher than the effective dose because many organs contributing the effective dose are well shielded by the human tissues in this irradiation geometry. Averaging the tooth dose and the effective dose over the all incident angles, the two doses are very close each other, 7.53 and 7.57 mSv/R, respectively. It can be concluded from this result that we can think of the measured dose in tooth as the effective dose in the case where photons more than 1 MeV are uniformly incident on the body from all the horizontal angles.

Table 1 compares doses in teeth measured by ESR with the results by EGS4 simulation for gamma rays from ^{60}Co source, incident on the body in AP and PA geometries. Since definitive relation between ESR signal and tooth dose has not been determined yet, doses in the table are relative to the dose in the front tooth. A very good agreement between measurement and calculation

was obtained in dose distribution in the mouth for both of AP and PA irradiation.

5 Conclusion

Experiments and calculation were performed to correlate quantitatively the dose in tooth with the effective dose for external gamma irradiation and a tentative result was obtained. Energy and angular dependence of tooth dose were obtained by the calculation using EGS4. Experimental results gave a validity to the calculations for some energies and incident directions of gamma rays. To get to the final goal of this work, the following major problems should be solved; development of precise phantom and consideration of energy spectrum of incident gamma rays.

References

[1] M. Ikeya, A. Kai, T. Miki and M. Hoshi, "ESR dosimetry of A-bomb radiation using tooth enamel and granite rocks", *Radiat. Prot, Dosim.* **17**, 181-184 (1986).

[2] M. Iwasaki, C. Miyazawa, T. Uesawa, and K. Niwa, "Effect of sample grain size on the CO_3^{3-} signal intensity in ESR dosimetry of human tooth enamel", *Radioisotopes* **42**, 470-473 (1993).

[3] M. Iwasaki, C. Myazawa, I. Itoh, T. Uesawa and K. Niwa, "Differences in the radiation sensitivity of human tooth enamel in an individual and among the individuals in dental ESR dosimetry", *ibid.* **44**, 785-788 (1995).

[4] V. A. Serezhenkov et al.,"Radiation dosimetry for residents of the Chernobyl region: A comparison of cytogenetic and electron spin resonance methods", *Radiat. Prot, Dosim.* **42**, 33-36 (1992).

[5] W. R. Nelson, H. Hirayama and D. W. O. Rogers, "The EGS4 Code System", *SLAC Report-265* (1985).

[6] I. Nojiri, S. Iwai, O. Sato, S. Takagi, S. Sawamura and Y. Fukasaku, "Development of EGS4 User's Code for General Purpose", *Donen-Giho* **No.102**, 59-66 (1997) (in Japanese).

[7] W. S. Snyder, M. R. Ford, G. G. Warner and H. L. Jr. Fisher, "Estimates of specific absorbed fractions for photon sources uniformly distributed in various organs of a heterogeneous phantom", *Medical Internal Radiation Dose Committee Pamphlet No.5* (*J. Nucl. Med.* 10(1969) Supplement No.3).

Table 1 Comparison of tooth doses calculated by EGS4 code with those by ESR dosimetry for irradiation of gamma rays from ^{60}Co source.

Direction	Method	Front teeth	Middle teeth	Back teeth
AP	EGS4 calculation	1.0	1.0	0.9
	ESR dosimetry		1.0	0.9
PA	EGS4 calculation		1.1	1.1
	ESR dosimetry		1.1	1.2

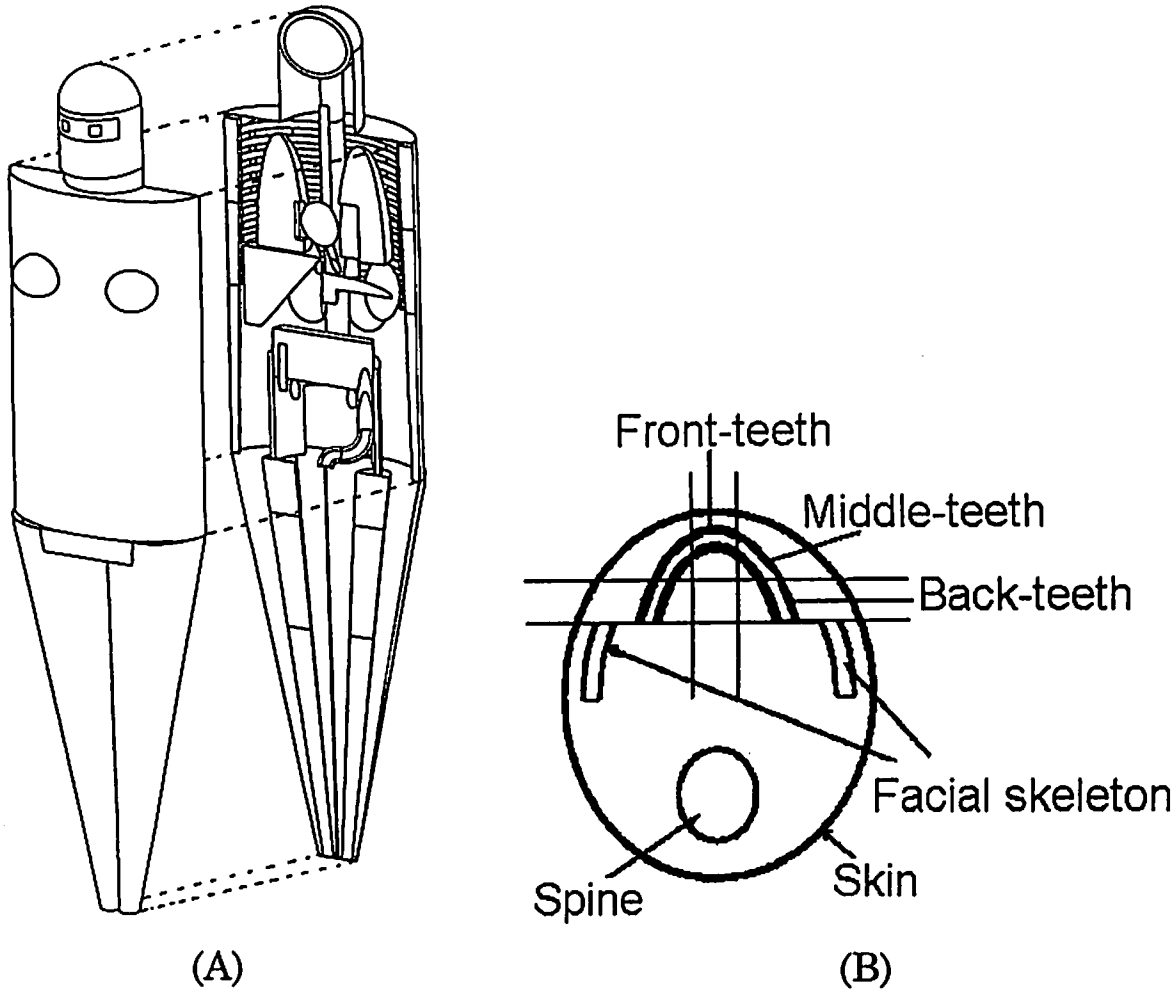

Fig. 1 Cross-sectional views of (A) MIRD-5 type mathematical phantom and (B) teeth region newly defined for this work.

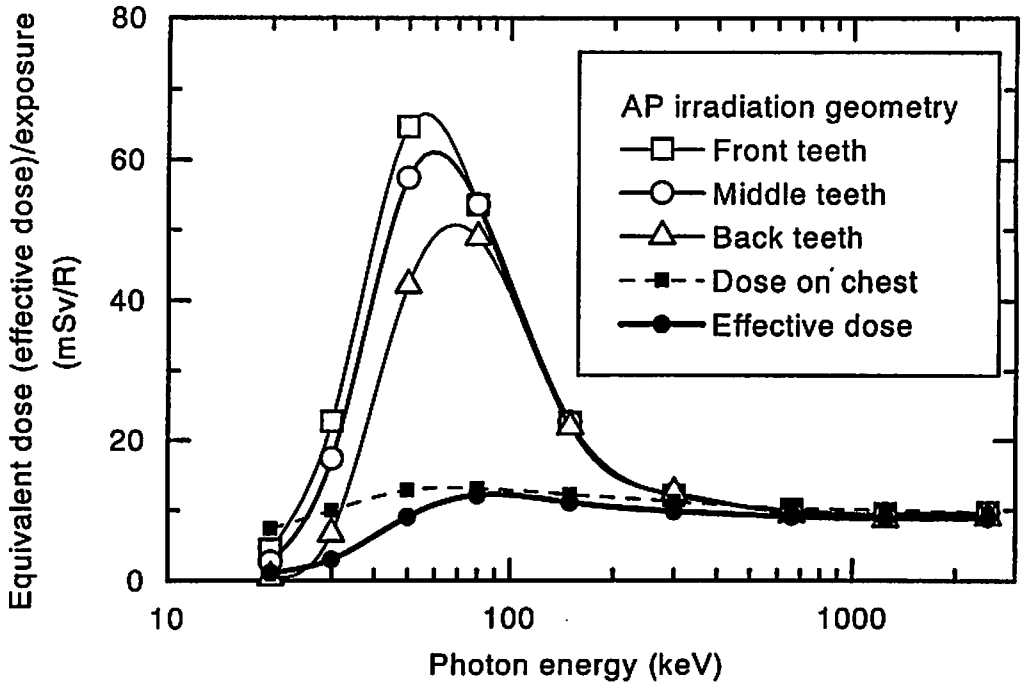

Fig. 2 Comparison of doses in some parts of teeth with effective dose for photons incident in parallel on the body from posterior.

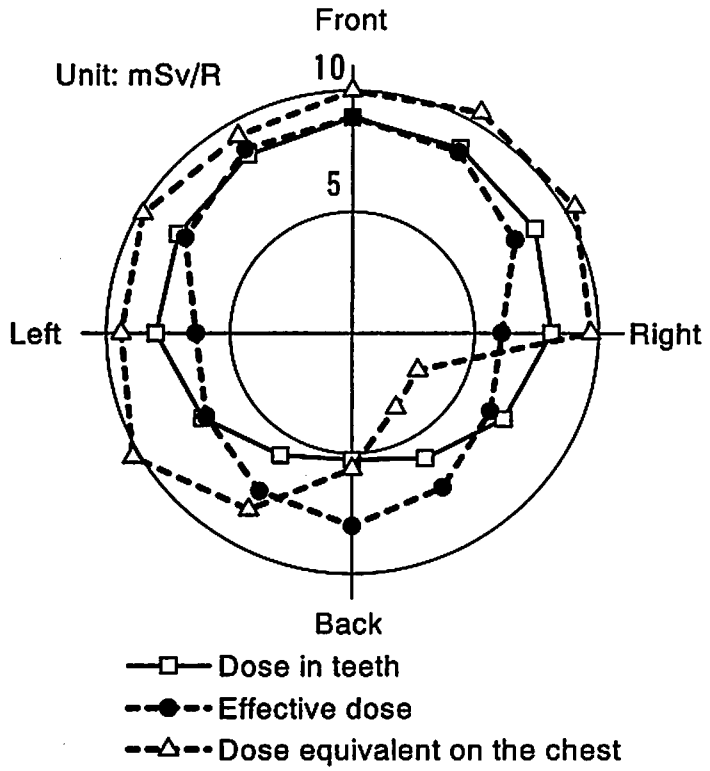

Fig. 3 Angular dependence of dose averaged over the teeth compared with effective dose and dose on the chest surface for 1250 keV photons incident in parallel on the body.

EXAMINATION OF THE X-RAY PIPING DIAGNOSTIC SYSTEM USING EGS4

G. KAJIWARA

Shimizu Corporation Institute of Technology
3-4-7 Etchujima, Koto-ku, Tokyo 135-8530, Japan

Abstract

With the purpose of testing the influence of rust in a corroded pipe on X-ray piping diagnostic system measurements, the EGS4 code was used to simulate an exposure of an X-ray film under conditions similar to the practical radiography arrangement. The deviation in the energy absorption value, which is assumed to correspond to the density increase of the exposure film, turned out to be larger than that for actual measurements. However, the simulation results matched qualitatively the measurements when intensifying screen and a number of emulsion layers were added. More work is needed to decide whether the EGS4 code is applicable or not to this sort of study.

1 Introduction

It has nearly been ten years since the X-ray piping diagnostic system[1] was developed and began to be practically used in buildings. This system is able to measure the thickness of a wall in an old pipe and with this data, it is able to exactly calculate the residual years of the pipe. The influence of rust blisters on the inside surface of a piping wall has not been taken into account. Because of the low density of rust, it has been assumed that the presence of rust does not significantly attenuate an X-ray radiography beam. A simple experiment using artificially made rust partially confirmed this assumption. However, particular experiment was not able to represent all combinations of rust and steel wall. Until recently, there has been no way to test the overall validity of this assumption. In my most recent research, I used EGS4 (Electron Gamma Shower ver.4) code to simulate an X-ray film exposure for the purpose of testing the effect of rust in a pipe on X-ray radiograph.

2 X-ray Piping Diagnostic System

This system uses X-ray radiography to evaluate the residual years of an old pipe. The procedure is illustrated in Fig. 1. X-ray film is used as a detector, because it is highly sensitive, is easy to handle on site, produces quick results, and is cheap. The scanning densitometer is used to read the film density exactly, and with this density data the thickness of the wall of an old pipe can be calculated. It works for old piping under 100-mm diameter, and the pipes can be either empty or water-filled. The measurement error for this range of piping is less than 10%.

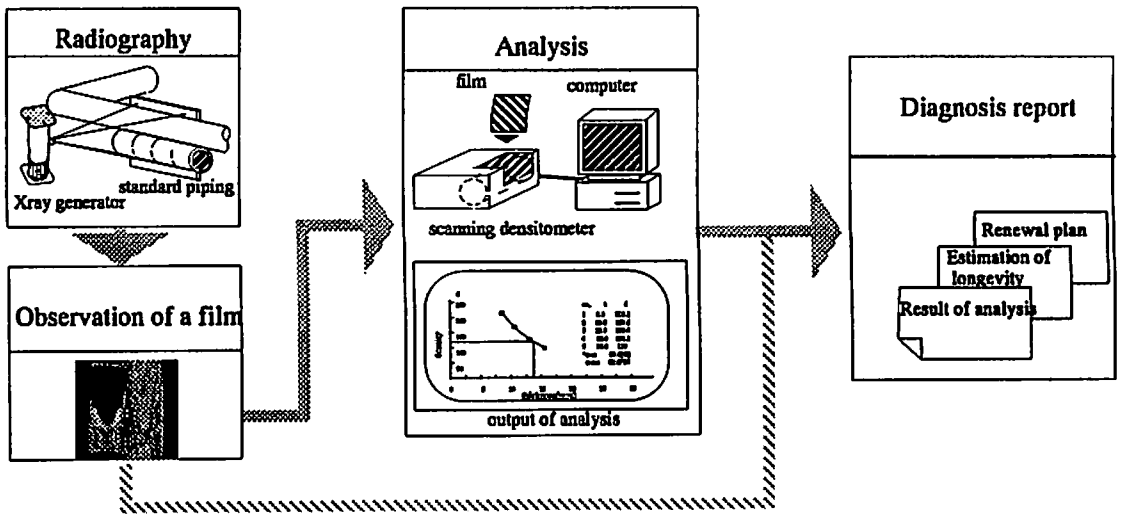

Fig.1 Block diagram of X-ray piping diagnostic system

3 Simulation Carried Out with EGS4

3.1 Simulation condition

The model used in the simulation was composed of several regions, as illustrated in Fig. 2. The areas of the regions were unbounded.

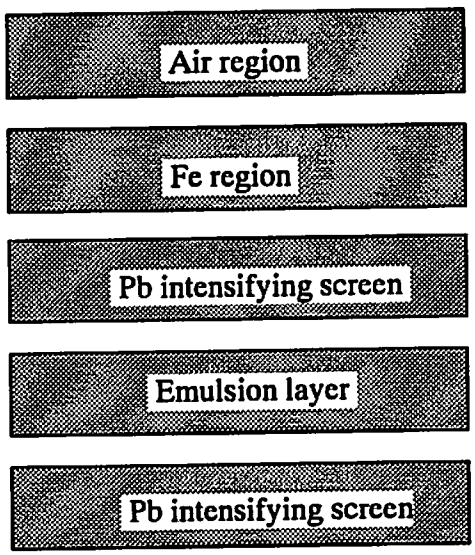

Fig. 2 Structure of a model for calculating the relation between steel plate thickness and absorbed energy.

Other conditions were as follows.

1. The detector is assumed to be a film. (K Co. type AA)
2. A steel plate is positioned in front of the film, the thickness of which was changed.
3. The incident angle of the X-ray is 90°.

4. The X-ray generator produced monochromatic 200-kV X-rays.

5. The energy absorption is assumed to correspond to the density increase of the exposure film.

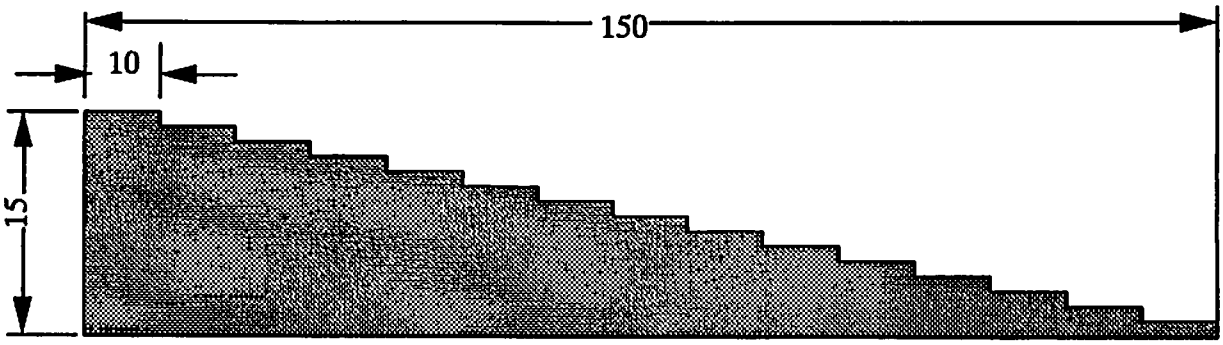

Fig. 3 Cross section of a contrastmeter (mm)

3.2 Simulating result

An iron contrast meter consisting of 15 steps was used to obtain the relationship between plate thickness and film density. (Fig. 3) The result of the simulation (Fig. 4) were then compared. The X-ray film was developed, and the density of a radiographed film was measured using a scanning densitometer. The results shows that the trends of both curves are similar, that is, the vertical value (density/energy deposition) goes down as horizontal value (thickness9 increases. However, the absorbed energy in the film as simulated by EGS4 had a deviation that was significantly larger than that of the film used with the contrast meter. To what extent the deviation could be reduced by increasing the number of histories was not confirmed yet. The structure of a real X-ray film for industrial use is illustrated in Fig. 6.

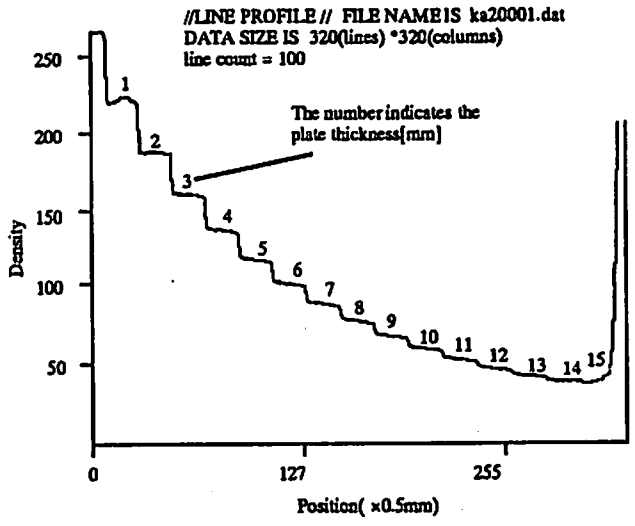

Fig. 4 Density profile of a constrastmeter using a scanning densitometer.

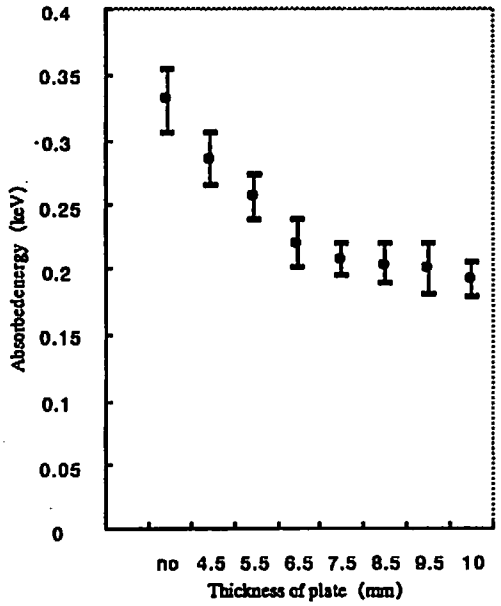

Fig. 5 Relationship between steel plate thickness and absorbed energy. A dot indicates the means value of flat bars around the dot indicates the deviation range.

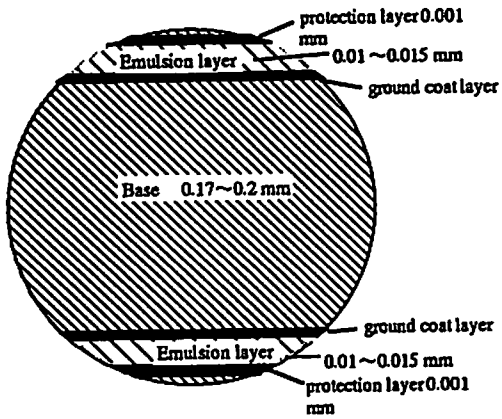

Fig. 6 Composition of X-ray film industrial use.

4 Qualitative Examination of the Film[2]

The effects of changing the number of emulsion layers on the film and using intensifying screen in front of the film was examined in the simulation. AgBr plate was also simulated. Figures 7 to 11 show the simulation results, and are arranged according to (1) number of particles (electrons/photons) crossing the detector plane, (2) absorbed energy, and (3) the structure of the model. What has become clear so far is the following.

1. The absorbed energy depends on the thickness of a plate.
2. The deviation in the absorbed energy corresponds to a change of more than 1 mm in plate thickness. This result seems not to match the exposed film results. The density deviation of the exposed film for a particular thickness is very small value, especially at the thin end of the contrastmeter (Fig. 4).
3. The measurement of thickness in the simulation should have an error under 10% on the absorbed energy.
4. The absorbed energy is larger in two layers of emulsion than it is in one layer of emulsion. It is also larger when the Pb intensifying screen is used.
5. The absorbed energy in the AgBr plate is larger than of the emulsion layer of the film. The absorption of electrons is thought to contribute most to the reaction of a film, and the level of absorption of electron in the AgBr plate is between one layer and two layers of emulsion.
6. The properties of the emulsion layer, for example, factors concerning the growth of crystals of halogenide silver, and the difference in time between the light exposed part and non-exposed

part in the process of developing were taken from a reference book [3]. Therefore these factors may been outside the EGS4 simulation.

5 Conclusion

The quantitative results of this examination cannot adequately explain the phenomenon. However, the qualitative results match the phenomenon. Therefore EGS4 simulation probably applicable to the study of rust corrosion in piping. However, this research is in preliminary stages and more works is needed.

Acknowledgement

The author is very grateful to Professor Hirayama in KEK who gave me help in all areas from way to using EGS4 to the components of a film.

References

[1] G. Kajiwara,"X-ray piping diagnostic system", *Journal of Testing and Evaluation* **Vol. 16**, 346-351(1998).

[2] N. Kobayashi,"Evaluation about effects of the intensifying screen with EGS4", Proceedings of the 2nd Symposium on Radiographic Testing. pp.13-16.

[3] foe example S. Kikuchi,"Chemistry of photography", Kyoritu Publishing Co., 201(1976).

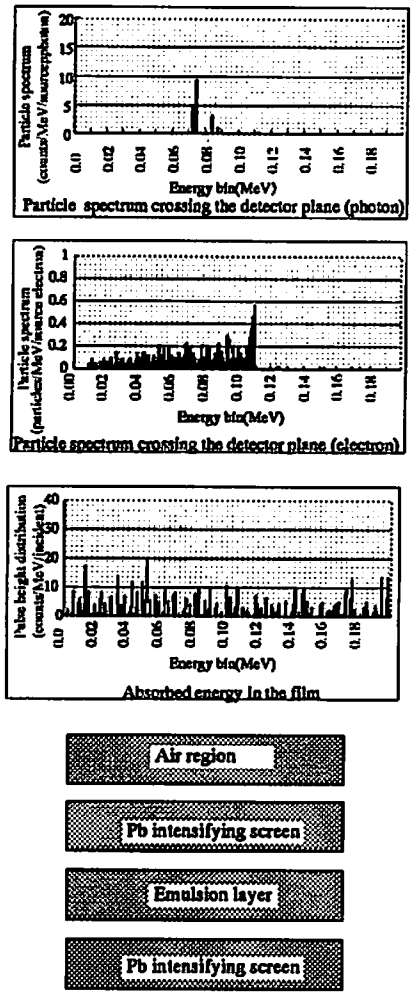

Fig. 7 One-sided emulsion layer on a film with Pb 0.03-mm intensifying screen (200 kV)

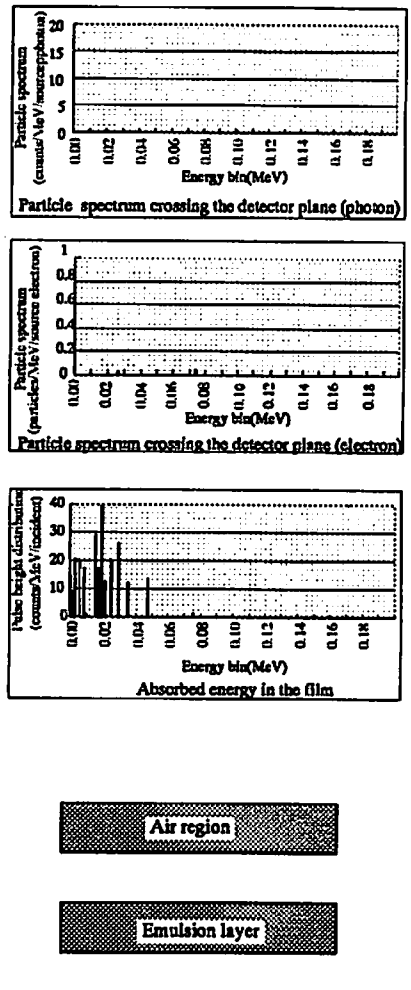

Fig. 8 One-sided emulsion layer on a film (200 kV)

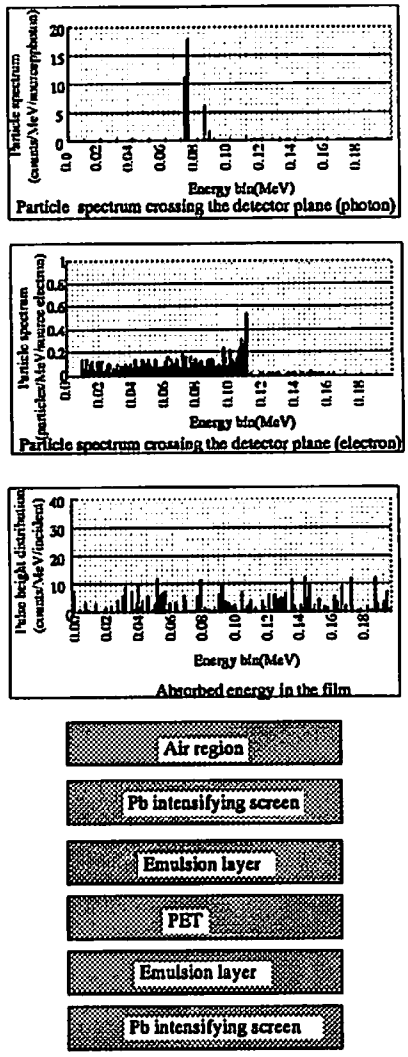

Fig. 9 Double-sided emulsion layer on the film with Pb 0.03-mm intensifying screen (200 kV)

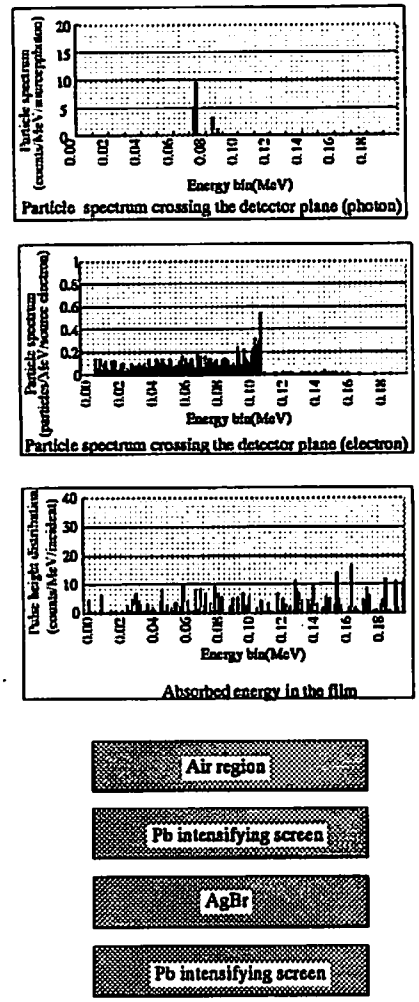

Fig.10 AgBr plate with 0.03-mm Pb intensifying screen (20 0 kV)

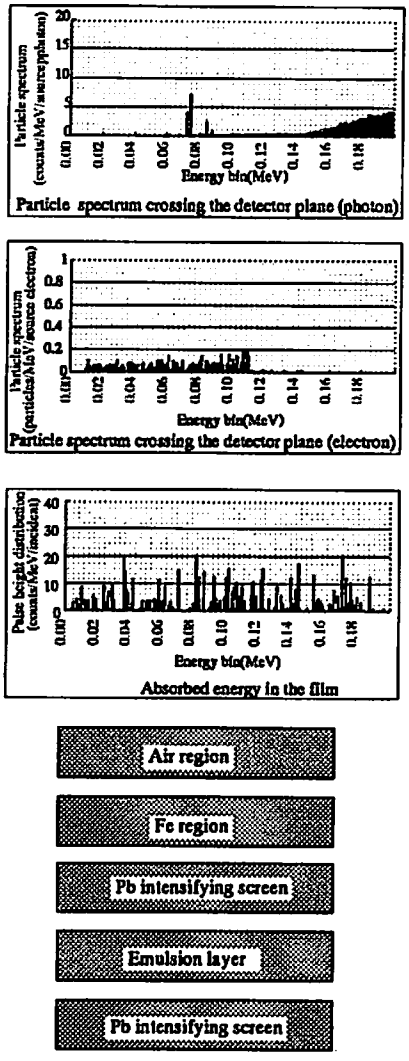

Fig.11 One-sided emulsion layer on a film with 0.03-mm Pb intensifying screen (200kV)

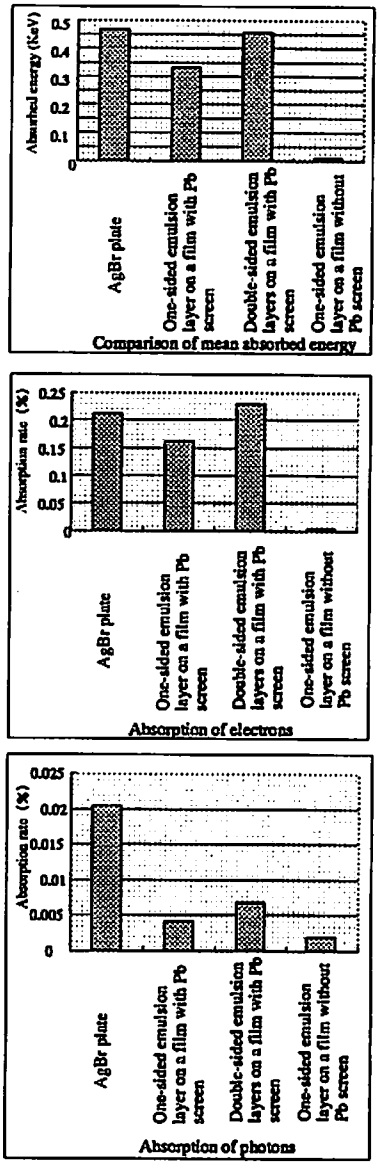

Fig.12 Comparison of absorbed energy according to detector

ANALYSIS OF BACKSCATTERED ELECTRON SPECTRA FROM HIGH-Z MATERIALS IRRADIATED WITH LOW ENERGY PHOTONS

Nobuteru NARIYAMA

Nuclear Technology Division, Ship Research Institute
6-38-1, Shinkawa, Mitaka, 181-0004 Tokyo, Japan
e-mail:nari@srimot.go.jp

Abstract

Total energies and spectra of electrons backscattered from silver and gold irradiated with 20-200 keV photons were calculated with a Monte Carlo transport code ITS. Influence of M- and N-shell electrons for energy reflection was found not to be negligible even above the K-edge energies: 15% for silver and 14% to 26% for gold. The influence was confirmed by comparing the calculated with measured backscattering dose factors using TLDs. Moreover, effect of Auger electrons was becoming larger with approaching the K-edge energies: 38% at 26.52 keV for silver. The cause of the large influence is attributed to the high electron energies relative to K-shell photoelectrons.

1 Introduction

When dosimeters and soft tissue of human body next to high atomic number materials are irradiated with photons, large doses are given in the vicinity of the interface by secondary electrons produced in the materials. Especially, when the interested region is very thin, the influence becomes severe. Moreover, for low energy photons, photoelectric effect becomes dominant so that photoelectrons and Auger electrons play an important role. In that case, which electron orbital is to be considered becomes more significant for electron simulation.

In this study, to investigate behavior of backscattered electrons influencing doses, total energies and spectra of the secondary electrons backscattered from silver and gold on which 20-200 keV photons were incident were calculated with a Monte Carlo transport code ITS [1].

2 Calculation Method

The code used is TIGERP of the ITS, which simulates photon and electron transport down to 1 keV. The geometry used is one-dimensional slab. The photon transport includes photoelectric effect, incoherent scattering with binding effect, coherent scattering with atomic form factor and pair production. In electron transport, condensed-history technique is used: electron trajectories are divided into path segments along which many interactions occur. To shorten the time consuming, angular deflection in the multiple scattering is sampled using Gaudsmitt-Saunderson theory [2]. The electron transport includes bremsstrahlung production and electron impact ionization.

Production of fluorescence photons and Auger electrons from K-, L-, average M- and N-shells are also considered. The cut-off energies used for photons and electrons in the calculation were set equal to 1 keV and 5% of maximum source energy, respectively.

In the calculations, 20-200 keV photons were incident normally on the silver and gold, and energy reflection and spectra of the backscattered electrons from the materials were obtained. The binding energies used in ITS for the two materials are tabulated in Table 1. The thicknesses of silver and gold were determined so as to satisfy the saturation of the number and energies of the electrons, that is, 35 and 30% of the CSDA range of the electrons of which the energy corresponding to the incident photon energy [3]. Energy reflection is defined as the total energies of the backscattered electrons per incident photon.

3 Results

Figure 1 shows the calculated doses in a 0.38 mm-thick LiF TLD directly given by incident photons and electrons reflected from each material. The LiF energies were obtained by multiplying the mass energy absorption coefficients of LiF by the photon energy. With increasing energy, the LiF doses given directly by the incident photons become smaller until about 80 keV, and over the energy the dose increases with energy. On the other hand, the electron reflection energies increase monotonously until 150 keV; that is, the influence of the electrons to the TLD dose becomes the largest around 80 keV when the scattered photons are neglected.

Figure 2 shows the electron spectra for silver. While for 200 keV photons only one peak corresponding to the K-shell electrons is observed, a small peak of L-shell electrons appears for 80 keV photons. For 40 keV photons, the L-shell electrons are seen more separately. Figure 3 indicates the spectra for gold. For 200 keV photons, the peaks of K- and L-shell electrons are observed, and for 100 keV photons the energies of the K-shell electrons become small and L-shell electrons dominant. For 40 keV photons, a small M-shell electron peak appears.

In both figures, M-shell and Auger electron distribution seems to be overlapped by K- and L-shell electron peaks. For the clear comparison, energy reflection calculated for silver were shown in Fig. 4 together with those for no M-shell electron and Auger electron transport, respectively. Even over the K-edge energy, differences of the values with and without M-shell electron transport become as much as about 10%. Moreover, below the energy, the difference rises to 30hand, the ratio of the value without Auger electrons to that with the electrons is remarkably great just above the K-edge energy: 38% at 26.52 keV. The electron spectra calculated are shown in Fig. 5. No Auger electron transport induces the decrease of the peak below 20 keV. On the other hand, without M-shell electrons the peak at 26 keV drastically diminish. The energy reflection calculated for gold is indicated in Fig. 6. As shown for silver, without M-shell electrons the values become smaller by 14 to 26% over the K-edge energy and 45% at 40 keV, and for Auger electrons the influence increases with approaching the edge energies.

4 Discussion

Even over the K-edge energy, the influence of M- and N-shell electrons to reflection energy has been confirmed clearly. Moreover, Auger electrons were found to make the dose larger with approaching the edge energy. To clarify the reason, the data related with photoelectric effect used in ITS were tabulated in Table 2. The values of PK means the fraction of photoelectric interaction occurring in the K-shell, and YK means the fluorescence yield. In the table, the values of PM are about 3% to 5% for both materials. Here it should be noticed that the photoelectrons from M-shells have larger energies than K-shell and the ratio of the two energies increases with approaching K-edge energy. Moreover, the energies of Auger electrons are much larger than that of K-shell

photoelectrons just above K-edge: KL1L1 Auger electrons have an energy of 18 keV approximately for silver. For the Auger electrons, while the fluorescence yield is large, the probability of K-shell photoelectric effect is also great. This is the reason that the influence of the Auger electrons to the reflection energies became larger near the edge as shown in Figs. 4 and 6.

To confirm the effect of M- and N-shell electrons experimentally, comparison with measurements [4] was made. Table 3 shows the backscattering dose factor for $Li_2B_4O_7$ TLD with gold. The TLD is 90 μm- thick powders on the 120 μm- thick polyimide film. The factor is defined as the ratio of dose in the TLD with the backing to that in free air. For 0.001 mm-thick gold, the ITS calculated values agreed with the measured. Without M- and N-shell electrons, however, the calculated values became smaller by 30% and 16% for 30 and 20 keV photons, respectively. For 0.00025 mm-thick gold, while even the values of normal ITS calculations are different from the measured, the calculated values without M- and N-shell electrons became about 15% smaller. The reason of the discrepancy between the calculations and the measurements can be considered that the gold thickness is too small for the condensed history technique used in the code and the average energy is used for M- and N-shell binding energy.

5 Conclusion

Total energies and spectra of electrons backscattered from silver and gold irradiated with 20-200 keV photons have been calculated using a Monte Carlo transport code ITS. The influence of M- and N-shell electrons was found not to be negligible for the total energies even above the K-edge energies. Moreover, Auger electrons influence the energies larger with approaching the edge energies since the energies of Auger electrons become much larger than that of K-shell electrons. For the calculations of doses in thin region, the detailed treatment for the electron transport is necessary.

References

[1] J. A. Halbleib, et al., "ITS Version 3.0: the integrated TIGER series of coupled electron/photon Monte Carlo transport codes," *SAND91-1634* (1992).

[2] S. Gaudsmit and J. L. Saunderson, "Multiple scattering of electrons," *Phys. Rev.* **57**, 24 (1949).

[3] N. Nariyama and S. Tanaka, "Responses of LiF TLD in different media and cavity ionization theory for low energy photons below 200 keV," *J. Nucl. Sci. Tech.* **34**, 137-147 (1997).

[4] N. Nariyama, Y. Namito, S. Ban and H. Hirayama, "TLD responses backed by copper, silver and gold for 20-40 keV monoenergetic photons," 12th International Conference on Solid State Dosimetry, Burgos, Spain (1998).

Table 1 Binding energy for each shell

	Ag	Au
$(E_b)_K$	25.514	80.725
$(E_b)_L$	3.81, 3.52, 3.35	14.35, 13.73, 11.92
$(E_b)_M$	0.532	2.77
$(E_b)_N$	-	0.404

unit: keV

Table 2 Ionization fraction and fluorescence yield

Ag				Au			
P_K	0.845	Y_K	0.84	P_K	0.8	Y_K	0.96
P_L	0.125	Y_L	0.01	P_L	0.15	Y_L	0.105
			0.055				0.357
			0.06				0.327
P_M	0.029	Y_M	0.0	$P_{M,N}$	0.05	Y_M	0.029

Table 3 Backscattering dose factors measured and calculated for $Li_2B_4O_7$:Cu backed with gold

E(keV)	Gold thickness (mm)	Exp.	ITS normal	ITS M,N-off
40	0.00025	2.73	2.10	1.83
30	0.001	2.37	2.43	1.71
	0.00025	1.58	1.90	1.56
20	0.001	1.57	1.44	1.21
	0.00025	1.46	1.32	1.14

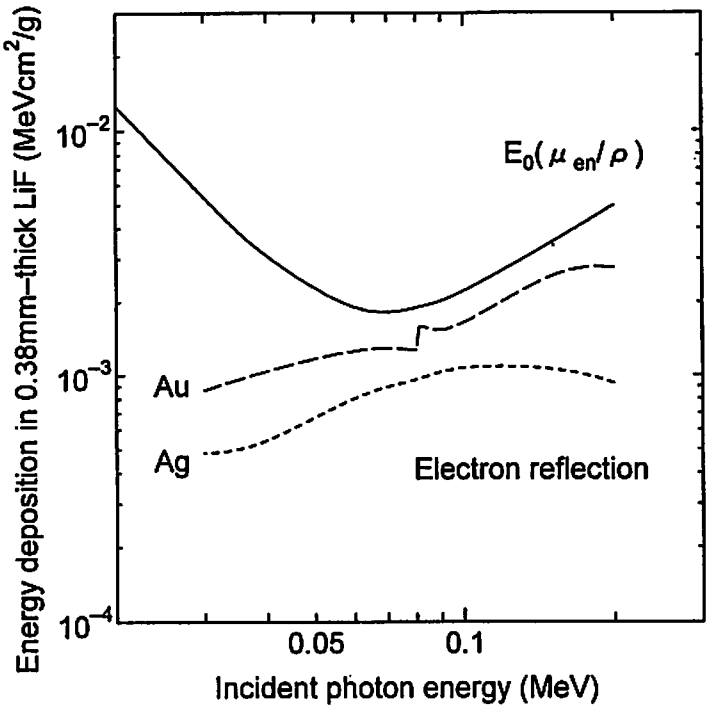

Fig.1 Electron energy reflection and energy deposition in a 0.38mm-thick LiF TLD without backings

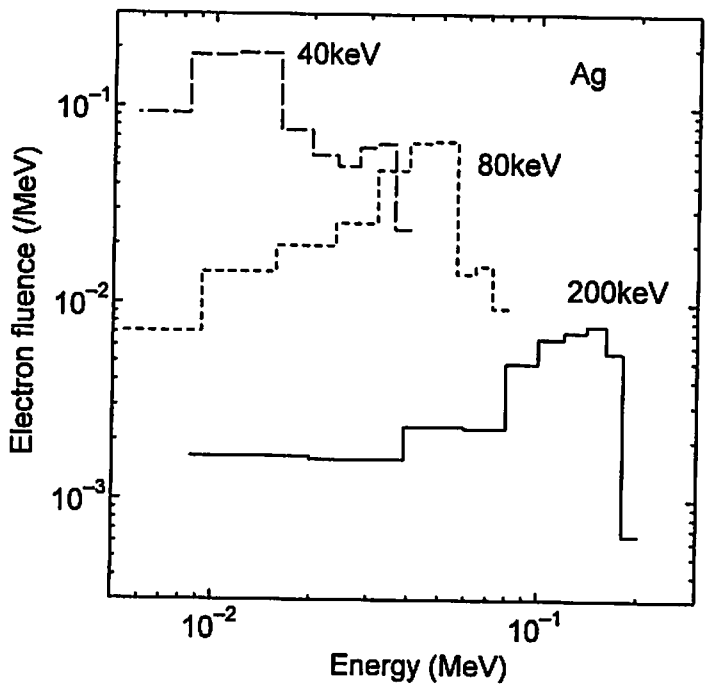

Fig.2 Electron spectra backscattered from silver

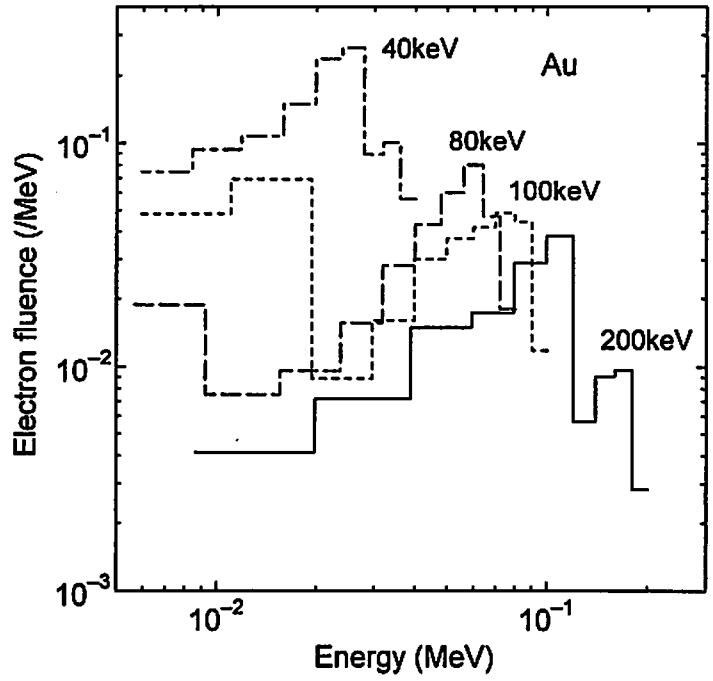

Fig.3 Electron spectra backscattered from gold

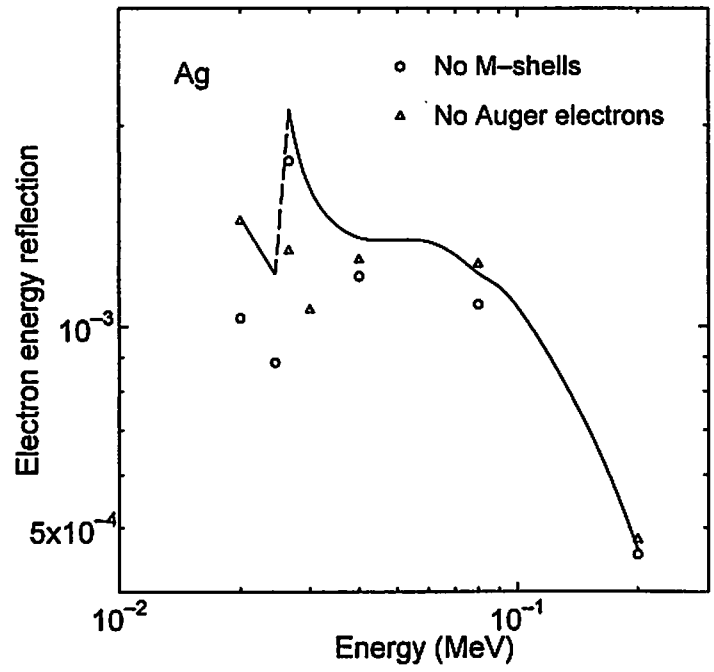

Fig.4 Electron energy reflection for silver

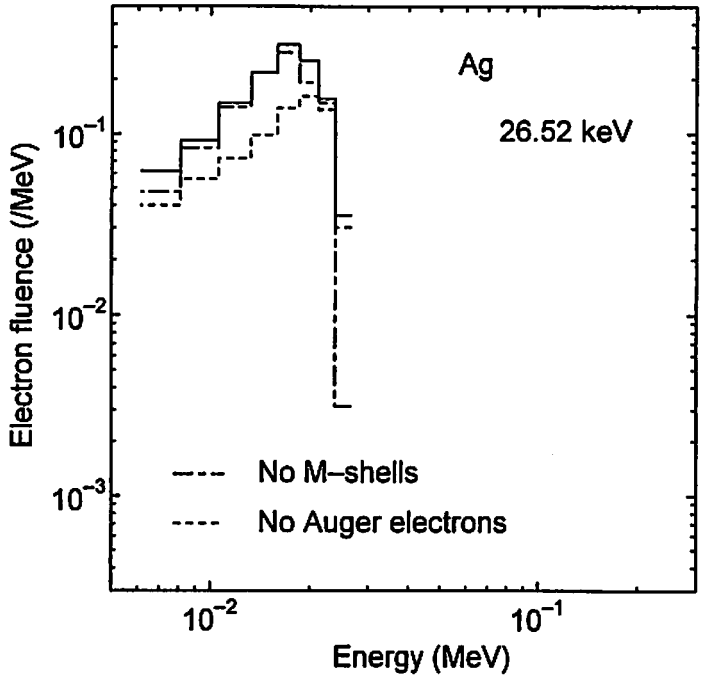

Fig.5 Electron spectra backscattered from silver irradiated with 26.52 keV photons

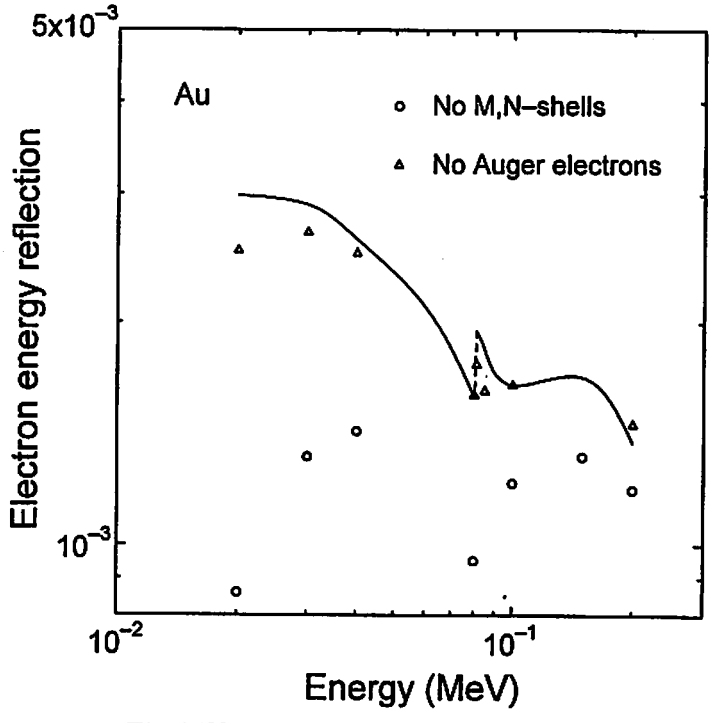

Fig.6 Electron energy reflection for gold